

NUO / SINCE 1579



Fragmentas iš Vilniaus universiteto auklėtinio Alberto Dablinskio (1601–1665) vieno geriausių XVII a. astronomijos veikalų *Centuria astronomica* (Vilnius, 1639), kuriame pateikta astronomijos pasiekimų apžvalga, remiantis stebėjimais teleskopu, atliktais kartu su kitu VU mokslininku, matematiku ir astronomu Osvaldu Krygeriu (apie 1598–1655).

VU biblioteka, BAV 47.10.21

Fragment from *Centuria astronomica* (Vilnius, 1639), one of the most well-known works on astronomy from the 17th c., written by Vilnius University graduate Albertus Dablinus (1601–1665). It presents an overview of achievements in the field of astronomy, based on observations using a telescope together with another VU scientist, mathematician, and astronomer Osvaldas Krygeris (c. 1598–1655).

VU Library, BAV 47.10.21



Vilnius
University

Integrated Diffractive Optical Elements for Terahertz Beam Shaping and Polarization Control

Surya Revanth Ayyagari

DOCTORAL DISSERTATION
2025



<https://doi.org/10.15388/vu.thesis.756>

<https://orcid.org/0000-0002-4129-8232>

VILNIUS UNIVERSITY
CENTER FOR PHYSICAL SCIENCES AND TECHNOLOGY

Surya Revanth Ayyagari

Integrated Diffractive Optical Elements
for Terahertz Beam Shaping and
Polarization Control

DOCTORAL DISSERTATION

Natural Sciences,
Physics (N 002)

VILNIUS 2025

The dissertation was prepared between 2021 and 2025 at the Center for Physical Sciences and Technology. The research was supported by EU program H2020-EU.1.3.1. topic MSCA-ITN-2020 (grant no. 956857).

Academic Supervisor – Prof. Dr. Irmantas Kašalynas (Center for Physical Sciences and Technology, Natural Sciences, Physics, N 002).

Dissertation Defence Panel:

Chairman – Prof. Habil. Dr. Jūras Banys (Vilnius University, Natural Sciences, Physics, N 002).

Members:

Assoc. Prof. Dr. Rimvydas Aleksiejūnas (Vilnius University, Natural Sciences, Physics, N 002).

Assoc. Prof. Dr. Ladislau Matekovits (Polytechnic University of Turin, Department of Electronics and Telecommunications, Italy, Natural Sciences, Physics, N 002),

Dr. Sergejus Orlovas (Center for Physical Sciences and Technology, Natural Sciences, Physics, N 002),

Prof. Dr. Tomas Tamulevičius (Kaunas University of Technology, Natural Sciences, Physics, N 002).

The dissertation shall be defended at a public meeting of the Dissertation Defense Panel at 11:00 on 23rd May 2025 in auditorium D401 of the Center for Physical Sciences and Technology.

Address: Saulėtekio ave. 3, D401, Vilnius, Lithuania

Tel. +370 5 264 8884; e-mail: office@ftmc.lt

The text of this dissertation can be accessed at the library of Vilnius University, as well as on the website of Vilnius University:

<https://www.vu.lt/naujienos/ivykiu-kalendorius>

<https://doi.org/10.15388/vu.thesis.756>

<https://orcid.org/0000-0002-4129-8232>

VILNIAUS UNIVERSITETAS
FIZINIŲ IR TECHNOLOGIJOS MOKSLŲ CENTRAS

Surya Revanth Ayyagari

Integriniai difrakciniai optiniai
elementai terahercinio pluošto
formavimui ir poliarizacijos valdymui

DAKTARO DISERTACIJA

Gamtos mokslai,
Fizika (N 002)

VILNIUS 2025

Disertacija rengta 2021–2025 metais Fizinių ir technologijos mokslų centre. Mokslinius tyrimus rėmė Europos Sąjunga, programa H2020-EU.1.3.1. tema MSCA-ITN-2020 (sutarties nr. 956857).

Mokslinis vadovas – prof. dr. Irmantas Kašalynas (Fizinių mokslų ir technologijų centras, gamtos mokslai, fizika, N 002).

Gynimo taryba:

Pirmininkas – prof. habil. dr. Jūras Banys (Vilniaus universitetas, gamtos mokslai, fizika, N 002).

Nariai:

Doc. dr. Rimvydas Aleksiejūnas (Vilniaus universitetas, fizika, gamtos mokslai, fizika, N 002),

Doc. dr. Ladislau Matekovits (Turino politechnikos universitetas, Italija, gamtos mokslai, fizika, N 002),

Dr. Sergejus Orlovas (Fizinių mokslų ir technologijų centras, fizika, gamtos mokslai, N 002),

Prof. dr. Tomas Tamulevičius (Kauno technologijos universitetas, gamtos mokslai, fizika, N 002).

Disertacija ginama viešame Gynimo tarybos posėdyje 2025 m. gegužės mėn. 23d. 11:00 val. Fizinių ir technologijos mokslų centro D401 auditorijoje.

Adresas: (Saulėtekio al., 3, Vilnius, Lietuva), tel. +370 5 2648884; el. paštas: office@ftmc.lt.

Disertaciją galima peržiūrėti Vilniaus universiteto bibliotekoje ir VU interneto svetainėje adresu:

<https://www.vu.lt/naujienos/ivykiu-kalendorius>

ACKNOWLEDGEMENTS

This thesis wouldn't have been possible without the support and guidance of many. I'm thankful to my academic supervisor, Irmantas Kašalynas, whose expertise and advice were crucial throughout this journey. With his support and encouragement, I have been able to widen my skillset during many conferences, work trips, and traineeships in Lithuania and abroad.

A big shoutout to my lab mates past and present from THz Atelier (Terahertz Photonics Laboratory), whom there are too many to individually address. The collaborative spirit of our lab not only propelled our research forward but also created a wonderful collaborative environment and made the lab a great place to learn and grow.

To everyone who contributed to this thesis directly or indirectly, in ways big or small, thank you. This work reflects not just my efforts but the support and encouragement I received from each one of you.

CONTENTS

ACKNOWLEDGEMENTS	5
ABBREVIATIONS.....	8
INTRODUCTION.....	10
MAJOR GOAL	13
OBJECTIVES OF THIS WORK	13
SCIENTIFIC NOVELTY	13
STATEMENTS FOR DEFENCE.....	15
AUTHOR CONTRIBUTION.....	15
PARTICIPATION IN RESEARCH PROJECTS.....	16
SECONDMENTS	16
LIST OF PUBLICATIONS.....	17
ON DISSERTATION TOPIC	17
Conference list.....	17
PRESENTED BY THE AUTHOR.....	17
PRESENTED BY CO-AUTHORS	19
1. LITERATURE OVERVIEW	20
1.1. DIFFRACTIVE LENSES	20
1.2. HCG-type WAVEPLATES.....	23
1.3. FREE-STANDING META-SURFACES.....	26
2. METHODS AND MODELS.....	30
2.1. Finite-difference time domain (FDTD) method	30
2.2. Multipole analysis method	31
2.3. Direct laser ablation (DLA) method.....	35
2.4. THz signal measurement and analysis methods.....	36
3. RESULTS.....	40
3.1. THz diffractive lenses	40
3.2. HCG-type Waveplates.....	56

3.3. Free-standing meta-surfaces	67
CONCLUSIONS	86
SANTRAUKA	87
REFERENCES	96
ANNEX	104
CURRICULUM VITAE	105
NOTES	107

ABBREVIATIONS

THz	Terahertz
DOE	Diffractive optical element
EM	Electromagnetic
MPZP	Multiphase zone plate
H-MPZP	Hybrid Multiphase zone plate
HCG	High contrast grating
QWP	Quarter waveplate
HWP	Half waveplate
FWHM	Fullwidth-half maxima
ZP	Zone plate
SZP	Soret Zone plate
FZ	Fresnel Zone
PQL	Phase quantization level
HRFZ-Si	High resistivity floating zone silicon
TE	Transverse electric
TM	Transverse magnetic
ARS	Anti-reflective structures
AMC	Amplification multiplication chain
DSP	Digital signal processing
ADC	Analog-to-digital converter
FFT	Fast Fourier transformation
FDTD	Finite difference time domain
TDS	Time domain spectroscopy
DLA	Direct laser ablation
VNA	Vector network analyzer

RF	Radio frequency
DUT	Device under test
TRM	Thru/Reflect/Match

INTRODUCTION

Optics based on diffractive optical elements (DOEs), which feature small thickness, low weight, and minimized absorption losses were established more than half a century [1]. Unlike traditional optics based on geometric principles, diffractive optics rely on wave optics to manipulate light by designing the subwavelength size optical elements that introduce specific phase shifts in passing radiation through the phenomenon of diffraction. This key advantage distinguishes DOEs from their refractive counterparts.

In recent years, the development of Terahertz (THz) technology has been greatly influenced by, THz beam-forming [2],[3], imaging [4], and communication [5]. Thus, a precise and dedicated design of optical elements that utilizes the diffraction has been of such a great importance. The possibility of replacing volume elements with thin structures has become more and more desirable in the GHz and THz ranges.

The DOEs in THz range offer a compact and lightweight alternative to traditional refractive optics, leveraging wave-based design principles. Among the most widely recognized DOEs are grating, waveplates, multi-phase zone plate (MPZP) lenses and metamaterials. The DOEs are particularly appealing for beam shaping applications in the THz domain due to their miniature size (comparable to the wavelength), light weight, and superior compatibility with on-chip technologies compared to traditional reflective and refractive elements [2],[6]. Depending on their specific function such as focusing, redirecting, or splitting of incoming radiation, DOEs can take on various structural forms, based on the design rules of wave optics [7]. These advantages make DOEs a focal point of interest for the THz research community. However, these optical elements that exhibit unusual electromagnetic (EM) behaviour require different design methods. With the rapid advancement of THz science and technology, there is a growing demand for high-performance optical components that are easier to fabricate and seamlessly integrate with semiconductor devices on-chip [8]–[10]. With their efficiency and versatility, DOEs have become a key focus in advancing THz science and technology for THz photonics integration on-chip with the semiconductor devices.

The PhD work focuses on the research and development of DOEs such as MPZP lenses, quarter and half waveplates, 2D resonator arrays (meta-surface) using silicon's high refractive index and stainless steel's electrical conductivity for operation at THz frequencies ranging from 0.1 to 1 THz. The work aims to achieve the additive functionalities such as beam focusing, control of polarization, antireflective and enhanced transparency behaviour via

manipulation of phase, amplitude, and polarization state of incoming THz radiation.

The thesis is discussed across four chapters. The first chapter gives a brief literature overview on the DOEs comprising three sub-chapters. Subchapter 1.1 is devoted to diffractive lenses, 1.2 is devoted to high contrast grating waveplates and 1.3 is devoted to the meta-surfaces.

The second chapter covers the Methodology and Models that are used for the development of DOEs.

The third chapter discuss the results development of DOEs for THz frequencies and includes three parts. Subchapter 3.1 is devoted to development and optimization of the MPZP. In this sub-chapter first part is devoted to the development binary diffractive lenses and the focusing performance dependence on number of Fresnel zones and F-number. Second part is devoted to the development of standard multi-phase zone plates and the study of focusing performance of such multiphase zone plates. Third part is devoted to the optimization of multiphase zone plates to hybrid multi-phase zone plates by reducing the structural complexity and the study of focusing performance of such hybrid multiphase zone plates without deterioration of focusing performance compared to the MPZP.

Subchapter 3.2 is devoted to the development of high contrast gratings (HCG) that functions as a waveplate and control the polarization of THz radiation. First part is the development of high contrast grating which can work as quarter waveplate (QWP) for THz frequencies. Second part is devoted to the design and optimization of HCG QWP waveplate to perform as a half waveplate (HWP) and improve its transmission performance along the grating axis. Third part is devoted to further optimization of HCG waveplate to improve overall transmission performance of the waveplate by significantly reducing the reflection losses for broader THz frequencies.

Subchapter 3.3 is divided into two parts, with first is devoted to the theoretical analysis and the experimental observations of mutual coupling behaviour of meta-atoms that led to the broadening of resonance bandwidth when are arranged in a square lattice array for metal-based meta-surfaces. In which we have discussed the study of electromagnetic response and a multipole decomposition analysis of single subwavelength resonator embedded in a frame. And the study of electromagnetic response and a mutual coupling behaviour of meta-atoms when they are placed at a subwavelength period of 2×2 resonator array arranged in a square lattice. Also, the study of electromagnetic response and a mutual coupling behaviour of meta-atoms with a 5×5 resonator array and 10×10 (Infinite) resonator array arranged in a

square lattice for THz frequencies. Second part is devoted to the study of electromagnetic response of meta-surfaces composed of silicon-based meta-atoms when are arranged in a square lattice array. In which we show the existence of the anapole resonances enabling enhanced transparency of the meta-surface at wide range of THz frequencies.

Last chapter four is devoted to the conclusions of whole PhD work.

MAJOR GOAL

The goal is to develop diffractive optics with semiconductor- and metal-based elements aiming to provide functionalities such as beam focusing, polarisation control with antireflective and enhanced transparency behaviours, with a wide operational bandwidth at THz frequencies.

OBJECTIVES OF THIS WORK

1. Development and research of the silicon-based MPZP lenses with aim to reduce design complexity at outer zones and fabrication time without deterioration of the focusing gain at THz frequencies.
2. Research and development of the silicon-based HCGs as a QWP and HWP, for efficient manipulation and control of polarization state with a suppression of reflection losses in a wide spectrum range from 0.1 THz to 1 THz frequencies.
3. Research and development of the metal-based and silicon-based meta-surfaces composed of single, 2x2, 5x5, 10x10, and an infinite number of meta-atoms, based on concentric disks and rings arranged in a square lattice with a aim to suppress the scattered radiation in the far-field and demonstrate enhanced transmission for broadband THz frequencies.

SCIENTIFIC NOVELTY

1. Development and demonstration of the hybrid multi-phase Fresnel lenses (H-MPZPs) with a hybrid combination of phase quantization levels, offering similar or even better focusing performance than basic MPZPs with the same number of phase quantization levels.
2. Development of a monolayer HCG-type waveplate with an anti-reflective design, functioning as a quarter waveplate (QWP) in the frequency range of 0.3 to 0.5 THz providing operational bandwidth of 200 GHz.
3. A novel design integrates periodic dielectric-air interface gratings on both sides of an HRFZ-Si silicon wafer, enhancing the performance of a quarter-wave plate (QWP) to a half-wave plate (HWP). The resulting structure combines the characteristics of both QWP and HWP, achieving improved TM polarization transmission, ranging from 90% to 100% across a broad THz frequency ranging from 0.4 to 0.9 THz.

4. We presented a new design that modifies the waveplate's surface from flat to sinusoidal, with an amplitude of $10\ \mu\text{m}$ and a period of $1500\ \mu\text{m}$ along the TE polarization, resulting in a significant reduction of the Fabry-Perot effect up to 10% amplitude modulation for both TE and TM polarizations and a successful decrease in the transmission gap between the polarizations to less than 10% across a frequency range of 0.3 to 0.9 THz.
5. The meta-surface composed of different number of resonators was developed on a thin free-standing metal (stainless-steel) film to reveal the mutual coupling behaviour between the meta-atoms demonstrating the increase of fullwidth-half maxima (FWHM) and the decrease of quality factor of resonance peak from 40 GHz to 150 GHz and from 8.5 to 2.1, respectively.
6. Far-field THz transmission spectra for a subwavelength-sized metamaterial, composed of a single resonator and 2×2 resonators on a thin free-standing metal film, were reported.
7. Silicon-based meta-surface of free-standing meta-atoms comprising concentric discs and rings was developed featuring an anapole state with enhanced transmission as high as 70% across a frequency range of 0.5 to 0.7 THz.

STATEMENTS FOR DEFENCE

1. Hybrid multiphase zone plates, integrating $Q = 8$ quantisation levels and $Q = 4$ with a $\pi/4$ phase increment in the outer zones, enhance focusing gain by up to 10% while reducing fabrication time by up to 50% compared to conventional $Q = 8$ multiphase zone plates.
2. Silicon high contrast gratings with ridge height of 200 μm , periodicity of 100 μm , and sidewall inclination on each side of 11 degrees create the $\pi/2$ phase difference between the orthogonal polarizations of EM wave in the frequency range of 0.3 to 0.5 THz, resulting in a bandwidth of 200 GHz, used for the development of quarter waveplates for efficient polarisation control of THz beam.
3. A meta-surface composed of metal conductivity based meta-atoms comprising concentric discs and rings exhibits a significant increase in resonance bandwidth (40 GHz to 154 GHz) and a reduction in q -factor (from 8.5 to 2.1), with a resonance peak at around 350 GHz, compared to a single meta-atom and a 10×10 array, due to the enhanced interaction of electromagnetic fields between neighbouring meta-atoms.
4. A meta-surface composed of low conductivity silicon-based meta-atoms comprising concentric discs and rings achieves enhanced transparency (up to 70%) by suppressing radiation in the far-field through the coexistence of compound anapole and anapole resonances within the frequency range of 0.5 to 0.7 THz.

AUTHOR CONTRIBUTION

The author simulated and measured the focusing performance, focusing gain of MPZP lenses fully in [P1]. The author simulated the phase characteristics and transmission performance of HCG waveplates and polarization experiments of QWP waveplate fully, partially in cooperation with co-authors contributed to the THz- TDS, VNA measurements in [P2]. The author simulated the S-parameters for all the meta-surfaces fully and partially contributed to the multipole decomposition analysis and to THz-TDS, VNA measurements in cooperation with co-authors in [P3]. The author partially involved in S-parameter calculations of silicon-based meta-surface in [P4].

Most of the sample simulations, fabrication, characterization, and experimental investigations were done in the Center for Physical Sciences and Technology (FTMC), Lithuania. A part of measurements of the HCG

waveplates and the meta-surface samples in [P2-P3] were performed at the University of Duisburg-Essen, Duisburg, Germany, and the University of Lille, Lille, France.

Fabrication of the samples were done by Dr. Simonas Indrišiūnas from the Laser Microfabrication Laboratory, FTMC. The author was involved in experimental investigations together with Dr, Daniil Pashnev, FTMC, Lithuania, for THz-TDS measurements, with Prof. Guillaume Ducournau, at the Institute of Electronics, Microelectronics and Nanotechnologies (IEMN), France, for VNA measurements, and with Dr. Andreas K. Klien and Prof. Andreas Stohr at the Department of Optoelectronics, University Duisburg-Essen, Germany, for some THz FDS measurements.

PARTICIPATION IN RESEARCH PROJECTS

The author was involved in:

1. EU TERAOPTICS project (grant no. 956857) under the program H2020-EU.1.3.1. topic MSCA-ITN-2020; since Jan 22nd 2021 to Jan 19th2024.
2. Hybrid plasmonic components for THz range (T-HP) of the Research Council of Lithuania (Lietuvos Mokslo Taryba) funded by the European Regional Development Fund according to the Measure No. 01.2.2-LMT-K-718-03-0096; since Jan 20th 2024.

SECONDMENTS

The author had secondments:

1. Training on THz frequency domain spectroscopy (FDS) system in November 13-26th 2022; characterization and analysis of the silicon waveplates samples in April 23rd- May 05th 2023 at the University of Duisburg-Essen, Duisburg, Germany.
2. Training on Vector Network Analyzer (VNA) in June 11-24th 2023; characterization and analysis of the Silicon Waveplates and 2D Metal resonators in November 19th- December 03rd 2023 at the University of Lille, Lille, France.

LIST OF PUBLICATIONS

In this chapter, the author listed all articles published since the start of PhD studies in January 2021.

ON DISSERTATION TOPIC

- [P1] **Surya Revanth Ayyagari**, Simonas Indrišiūnas, and Irmantas Kašalynas, "Hybrid Multiphase Fresnel Lenses on Silicon Wafers for Terahertz Frequencies," in *IEEE Transactions on Terahertz Science and Technology*, vol. 13, no. 3, pp. 231-236, May 2023, doi:10.1109/TTHZ.2023.3263638.
- [P2] **Surya Revanth Ayyagari**, Andreas K. Klein, Simonas Indrišiūnas, Vytautas Janonis, Daniil Pashnev, Abdu Subahan Mohammed, Guillaume Ducournau, Andreas Stöhr, and Irmantas Kašalynas, "Broadband high-contrast-grating-type waveplates for the terahertz range," *Opt. Express* 32, 15870-15881 (2024), doi: 10.1364/OE.521532
- [P3] **Surya Revanth Ayyagari**, Simonas Indrišiūnas, Alexey Basharin, Vytautas Janonis, Daniil Pashnev, Guillaume Ducournau, Polina Kuzhir, and Irmantas Kašalynas, "Experimental observation of mutual coupling in resonator array on thin-metal-film," *J. Appl. Phys.*, vol. 137, no. 1, Jan. 2025, doi: 10.1063/5.0245081
- [P4] Isaac Appiah Otoo, Alexey Basharin, Anar Ospanova, Grigorii Matveev, Georgy Fedorov, Petri Karvinen, **Surya Revanth Ayyagari**, Daniil Pashnev, Andrzej Urbanowicz, Justinas Jorudas, Irmantas Kašalynas, Yuri Svirko, Polina Kuzhir "Broadband Transparency in Terahertz Free-Standing Anapole Metasurface," *Appl. Phys. Lett.*, vol. 125, no. 26, Dec. 2024, doi: 10.1063/5.0246993.

CONFERENCE LIST

PRESENTED BY THE AUTHOR

- [K1] **Surya Revanth Ayyagari**, Simonas Indrišiūnas, and Irmantas Kašalynas. Development of Hybrid Multi-Phase Zone Plate Fresnel Lenses for Frequency of 585 GHz. In abstract book of the EEE festival and Research 2022 conference; London, United Kingdom; **Poster presentation.**

[K2] **Surya Revanth Ayyagari**, Simonas Indrišiūnas, and Irmantas Kašalynas. Development of silicon based Hybrid multi-phase fresnel lenses for THz frequencies. In abstract book of 11^{oji} doktorantų ir jaunujų mokslininkų konferencija „FizTech 2022“; Vilnius, Lithuania, 2022; **Oral presentation.**

[K3] **Surya Revanth Ayyagari**, Simonas Indrišiūnas, and Irmantas Kašalynas. Phase profile optimization of silicon multi-phase zone plate lenses for operation at 585 GHz frequency. In the Proceedings of the 2022 47th International Conference on Infrared, Millimeter and Terahertz Waves (IRMMW-THz); IEEE, Delft, Netherlands, 2022, pp. 1-2, doi: 10.1109/IRMMW-THz50927.2022.9895492; **Poster presentation.**

[K4] **Surya Revanth Ayyagari**, Simonas Indrišiūnas, Gediminas Račiukaitis, and Irmantas Kašalynas. Development of Hybrid phase profile silicon multi-phase zone plate lenses for THz frequencies. In abstract book of the Advanced Properties and Processes in Optoelectronic Materials and Systems (APROPOS 18); Vilnius, Lithuania, 2022; **Oral presentation.**

[K5] **Surya Revanth Ayyagari**, Alexey Basharin, Simonas Indrišiūnas, Daniil Pashnev, Vytautas Janonis, Polina Kuzhir, and Irmantas Kašalynas. Mutual coupling effects between meta-atoms for enhanced bandwidth. In the Proceedings of the 2023 48th International Conference on Infrared, Millimeter and Terahertz Waves (IRMMW-THz); IEEE, Montreal, QC, Canada, 2023, pp. 1-2, doi: 10.1109/IRMMW-THz57677.2023.10298979; **Poster presentation.**

[K6] **Surya Revanth Ayyagari**, Simonas Indrišiūnas, Daniil Pashnev, Vytautas Janonis, Andreas Kurt Klein-Schuster, Guillaume Ducournau and Irmantas Kašalynas. Simple Dielectric-Based Quater Waveplate (QWP) for Broadband THz Frequencies In abstract book of the 45th Lietuvos nacionalinė fizikos konferencija; Vilnius (LNFK-45), Lithuania, 2023; **Oral presentation.**

[K7] **Surya Revanth Ayyagari**, Simonas Indrišiūnas, Daniil Pashnev, Vytautas Janonis, and Irmantas Kašalynas. THz Waveplate based on Laser Processed Silicon Grating. In abstract book of 12th doktorantų ir jaunujų mokslininkų konferencija „FizTech 2023“; Vilnius, Lithuania, 2023; **Oral presentation.**

[K8] **Surya Revanth Ayyagari**, Vytautas Janonis, Andreas Kurt Klein-Schuster, Simonas Indrišiūnas, Daniil Pashnev, Dalius Seliuta, Andreas Stohr, Guillaume Ducournau and Irmantas Kašalynas. Planar diffractive optical elements for THz beam polarization control. In abstract book of German Microwave conference 15th (GEMIC 2024); Duisburg, Germany; **Oral presentation.**

[K9] **Surya Revanth Ayyagari**, Vytautas Janonis, Andreas Kurt Klein-Schuster, Simonas Indrišiūnas, Daniil Pashnev, Dalius Seliuta, Andreas Stohr, Irmantas Kašalynas and Guillaume Ducournau. Investigation of Dielectric Deep-Groove-Gratings as a Quarter Waveplate in the Terahertz Range. In the Proceedings of the 2024 International Conference on Electromagnetics in Advanced Applications IEEE and Antennas and Propagation in Wireless Communications (ICEAA_APWC_2024) conference; Lisbon, Portugal, Sep. 2024, pp. 801–803. doi: 10.1109/ICEAA61917.2024.10701792; **Oral presentation.**

PRESENTED BY CO-AUTHORS

[K10] **Surya R. Ayyagari**, Alexey Basharin, Simonas Indrišiūnas, Daniil Pashnev, Vytautas Janonis, Polina Kuzhir, Guillaume Ducournau, and Irmantas Kašalynas*. Research of anapole modes in ring-shaped subwavelength periodic structures fabricated on thin free-standing metal film. In the Proceedings of the 2024 International Conference on Electromagnetics in Advanced Applications IEEE and Antennas and Propagation in Wireless Communications (ICEAA_APWC_2024) conference, Lisbon, Portugal, Sep. 2024, pp. 804–805. doi: 10.1109/ICEAA61917.2024.10701944; **Oral presentation.**

1. LITERATURE OVERVIEW

1.1. DIFFRACTIVE LENSES

Refractive lenses have a curved, homogeneous surface that causes a uniform phase shift in light passing through. They are typically thicker than the wavelength of light they handle, making them effective in focusing light over a wide range of wavelengths. In contrast, Fresnel lenses or diffractive lenses evolved as an optimization over traditional refractive lenses. They are designed to reduce the dimensions of the lens approximately to the size of wavelength by focusing light at the required focal length for a desired frequency. Typically, these lenses function effectively for a narrow frequency range. Fresnel lenses are classified into amplitude and phase based lenses. Amplitude based lenses block part of the radiation and have lowest diffraction efficiency. However, phase based lenses can have different profiles—binary, multi-level, or kinoform which has higher efficiency than the amplitude based lenses. Amplitude based lenses are also known as Soret zone plate (SZP) or Soret lenses uses alternating transparent and opaque circular zones to focus light. The lens with odd transparent circular zones is positive SZP and the lens with even transparent circular zones is negative SZP as shown in Fig. 1. This simple structure, while efficient in focusing, achieves limited focusing efficiency (around 10%). These lenses often made of metals which is a case of the width reduction as it may be fabricated from an extremely thin metal foil (tens of microns in thickness). As the radiation approaches to the binary zone plate it diffracts around the opaque zones into multiple spherical waves that converge at a focal point [11]. The design of such zone plate (ZP) is based on the formula:

$$r_n = \sqrt{n\lambda F + \frac{n^2\lambda^2}{4}} \quad (1)$$

where r_n is the radius of the n -th zone, n is the number of zone, λ is the desired wavelength, and F is the focal length.

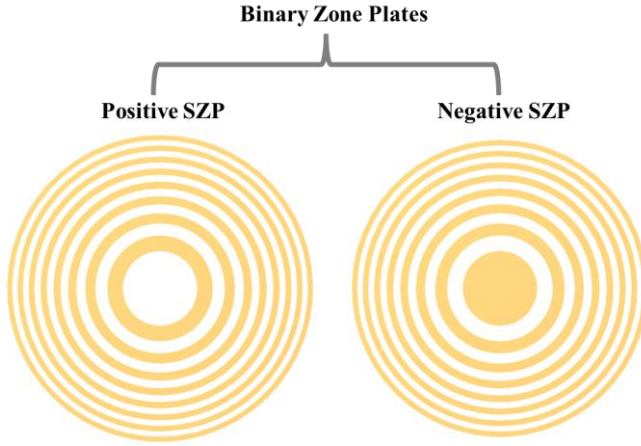


Figure 1: The illustration of positive and negative soret zone plate (SZP).

The efficiency of a zone plate is increased 4 times (up to 40%) when instead of opaque zones are replaced by transparent zones, where phase change is introduced. This is achieved by etching a groove which is a subzones or phase quantization levels (PQLs), in the surface of dielectric or transparent material, where the depth groove (subzone) is selected as to retard the radiation phase (φ) by π , resulting in two phase quantisation levels of $\varphi = 0$ and $\varphi = \pi$. The design of a MPZP is based on the formula:

$$r_n = \sqrt{\frac{2\lambda n(F + \frac{d}{2})}{Q} + \frac{n^2 \lambda^2}{Q^2}} \quad (2)$$

$$d = \frac{\lambda}{Q(\varepsilon - 1)} \quad (3)$$

here r_n is the outer radius of n -th subzone (concentric ring), d is the depth of single subzone, Q is the number of subzones or PQL, and ε is the refractive index of media, for example Si substrate possesses $\varepsilon = 3.45$. Other notations are the same as in previous equations.

The efficiency of such MPZP lenses climbs asymptotically upto 100% with the increase of PQLs introduced into the lens profile. For example the scheme of MPZP lens with eight subzones is shown in Fig. 2 along xy -plane and xz -planes which was proven that the efficiency of such MPZP lens is 95% [6].

MPZP lens

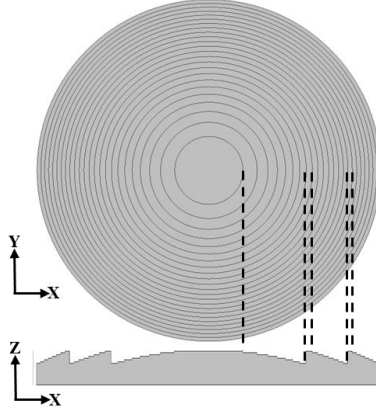


Figure 2: The illustration of multi-phase zone plate (MPZP) lens with eight subzones along xy - and xz -planes.

MPZP is a successful example of DOE which defines the beam shape by describing the phase and amplitude distribution of incident wave at the focal plane. In general, MPZP makes a phase shift of incoming radiation resulting in a constructive wave interference at predefined distance along an optical axis. In a particular case the thickness of material is adjusted to introduce the phase offsets strictly related to value of the effective refractive index. Further, the efficiency of MPZP lens can reach upto 100% in the case of kinoform structures having continuous phase profile [6]. The phase profile of such kinoform structure can be represented by φ with the non-paraxial approach shown in the Eq. 4. Especially, in the THz frequencies when the diameter of the element is almost equal to its focal length the non-paraxial approach works better providing highly reduced off-axis aberrations with the increased efficiency [12],[13].

$$\varphi = e^{-ik\sqrt{r^2+F^2}} \quad (4)$$

Where $k = \frac{2\pi}{\lambda}$, is the wave number.

Different tools such as mechanical polishing, hot pressing, 3D printing have been used for the development of the MPZPs of different low refractive index materials such as polymers, Teflon, polyamides, paraffins which possess small optical losses in the sub-THz frequency range [14],[15],[16],[17]. All those materials and fabrication processes make bottle-neck for the developments at higher THz frequencies and for the integration of MPZPs on-chip with other THz devices [9],[10]. Researchers moved to higher

frequencies by making use of the silicon (Si) with low absorption losses typical for many semiconductor crystals [18],[19]. Reactive ion etching [20] and photo-lithography [21] are the two most common methods used to manufacture Si-based MPZPs; however, they are tedious if several processing steps need to be modified [22]. A mask-less direct laser ablation (DLA) technology was proposed recently [23],[24] as a flexible tool for the development of MPZPs with different number of the PQLs, which demonstrated good focusing performance in a wide frequency range from 0.6 THz up to 5 THz [25],[26]. Large Fresnel losses due to high refractive index of Si was proposed to compensate by fabrication of anti-reflection coatings within the same DLA process [27],[28],[29]. Notably that the diffraction efficiency of Si based MPZPs with large Q value can reach almost 100% [19]. However, manufacturing of the MPZP with large number of PQLs is challenging task because the complexity of step profile increases going towards the outer zones [26]. On the other hand, the design of lens with high numerical aperture, defined as the ratio between the diameter and the focal distance, needs to be considered in a case of THz device manufacturing on-chip. Indeed, DLA processing of Si for THz technologies make a specific requirements for the surface smoothness and dimensions of the phase-delay-material used especially in the area of most outer zones [19],[30]. It is worth noting that only with appearance of the DLA technology, many designs of DOEs became possible to realize of crystal materials in the THz range [31],[32],[33],[34]. However, the aim of this research work focuses on the integrated diffractive optics, the achieved overall focusing gain or diffraction efficiency is not a concern of this work. For this reason, we have performed the development and research on Hybrid multi-phase zone plates (H-MPZP) by integrating MPZP ($Q = 8$) together with MPZP ($Q = 4$), aiming to reduce complexity and simplify fabrication processes compared to conventional MPZP maintaining $Q = 8$, which is discussed in detail in the Results Section.

1.2. HCG-type WAVEPLATES

An efficient manipulation and control of EM wave phase and polarization are essential for controlling the propagation of light and it is a great necessity for the mentioned application in the introduction part. Waveplates and phase retarders are vital components which manipulate and control the polarization state and phase of the EM wave. Usually, the waveplates are designed to introduce a specific phase delay between two orthogonal polarization components of EM wave. Most commonly conventional methods for the

control of phase and polarization depend on the intrinsic properties of natural birefringence materials, which support different phase delays along the two orthogonal optical axes. The number of easily applicable naturally birefringent materials is very limited in the THz range due to the small difference of the refractive indexes, large losses, bulk size, and high cost of material and production [35]. For example, natural birefringence in liquid crystals and crystalline quartz is low in the range of 0.3-0.5 THz possessing values of 0.127 [36] and 0.046 [37], respectively. Therefore, due to their low birefringence the thickness of a waveplate can reach up to several millimetres and that makes them difficult to integrate with other THz devices. Moreover, low loss, THz transparent materials like silicon and polymers such as HDPE and Teflon are isotropic and possess no birefringence at all. Another of commonly used materials is lithium niobate (LiNbO₃), with birefringence effect caused by its nonlinearity, but its use in THz range is hampered by high absorption losses [38]. Some of the ways to improve the operational bandwidth and to achieve a π phase retardation in the waveplate are the use of a multi-layer design taking advantage of natural material birefringence [39], or introduction of artificial birefringence via creation of some complex subwavelength structures [40],[41] use of aperiodic gradient grating [42] or Fresnel rhomb waveplate design [43]. Artificial birefringence has to be created either by producing periodic sub-wavelength structures or by surface modification introducing a spatial asymmetry which provides high order anisotropy [35],[44]. One way to create an artificial birefringence is by creating a subwavelength grating on the surface [35] or in the volume of the material [45] as shown in Fig. 3.

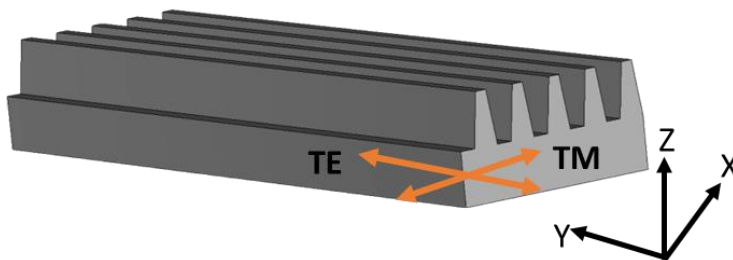


Figure 3: The Schematic representation of single-sided monolayer high contrast gratings (HCG) waveplate.[46]

The surface structures are made by etching or ablating subwavelength periodic grooves with the periodicity of around $\lambda/8$ and depth of $\lambda/4$. However,

dielectric-grating-based waveplates seem to be more attractive than metal-based ones because of their low loss and phase retardation proportional to product of refractive index and physical thickness, called optical thickness at specific wavelength [38]. Though the dielectric-based grating waveplates are suitable for the manipulation of THz polarization in transmission mode because of high transparency, they still lack the operational bandwidth for broadband regime as the phase retardation is proportional to the frequency [42]. Moreover achieving a phase difference of π between the orthogonal polarization components is itself complicated for low refractive index materials [35]. Use of low-loss silicon as the waveplate material is advantageous because of its high thermal stability as compared to polymers as well as established processing techniques, especially when the device under test needs to undergo high-intensity laser fabrication and characterization methods [30]. Moreover, it stands out as one of the most transparent materials with minimal absorption losses across the THz frequencies. Additionally, silicon exhibits low dispersion indicating that its refractive index remains constant regardless of the frequency in THz range. Important advantage for constructing a waveplate lies in its high refractive index with 3.45 as compared to polymer materials which values are around 1.45 at THz frequencies. This characteristic enables silicon substrates to have a reduced physical thickness compared to polymers while still achieving the necessary phase retardation. The HCG was proposed of a single layer of high-index-contrast subwavelength grating in which tailoring of the dispersion relations of two orthogonal waveguide modes is supported by the structure [47],[48]. As the periodic gratings merely resemble a periodic waveguide along the propagation direction a few waveguide modes are excited depending on the angle of incidence of the plane wave. Because of large index contrast and functional properties of HCG, only two waveguide modes with real propagation constants carries electromagnetic energy along the propagation direction for a wide frequency range. When the HCG subjected to normal incidence light only even modes are excited such as zeroth order and second order modes of transverse electric (TE) and transverse magnetic (TM) denoted with TE_0/TM_0 and TE_2/TM_2 whereas, under oblique incidence odd modes are excited. However, only zeroth order diffraction carries energy both in reflection and transmission because of HCG's subwavelength period in air [49]. In addition, there is some insertion loss for grating based waveplates due to a strong reflection at the material-air interfaces which can be reduced by adding anti-reflection layers [50] or structures [51],[28]. In the THz range, the broadband anti-reflective structures (ARS) of subwavelength dimensions were developed on crystalline material using mechanical dicing blade or direct

laser ablation [52] techniques. However, for large scale micro structuring applications these techniques may encounter certain limitations in terms of fabrication time and efficacy. Notably, issues such as surface roughness may arise, potentially causing scattering or diffraction losses, particularly at higher THz frequencies [30]. Nevertheless, efficient control of polarization of light requires a waveplate with wide operational bandwidth, achieving a phase difference of $\pi/2$ or π , and less reflection losses at high frequencies. To achieve all the above qualifications in a single component, the waveplate design becomes more complex and difficult to implement. Thus, in the Results Section we have shown the HCG waveplates working as quarter waveplate and half waveplate with anti-reflective behavior for a desired THz frequencies from 0.1 THz to 1 THz.

1.3. FREE-STANDING META-SURFACES

Metamaterials have rapidly emerged as a dynamic and expanding field of research in recent years, largely due to their exceptional EM properties opening a lot of applications in optics and photonics. These materials, engineered with subwavelength structures, exhibit extraordinary EM behaviour not found in naturally occurring materials. The individual subwavelength components, known as meta-atoms, interact with the EM fields in such a way that they allow for precise manipulation of the properties of EM waves [53],[54]. All metamaterial characteristics are highly dependent on the geometry, size, and composition of the meta-atoms as well as their arrangement in space. Meta-surfaces are a class of metamaterials that are ultra-thin and planar structures composed of subwavelength-sized elements (meta-atoms) that are arranged in a specific pattern in two-dimensional (2D) plane on the substrate to achieve a desired response to incident EM waves [55]. Meta-surfaces composed of meta-atoms with varying geometries, arranged in a periodic array and embedded within a frame, as shown in Fig. 4, where P being distance between the neighbouring meta-atoms or periodicity and t being the overall thickness of meta-surface.

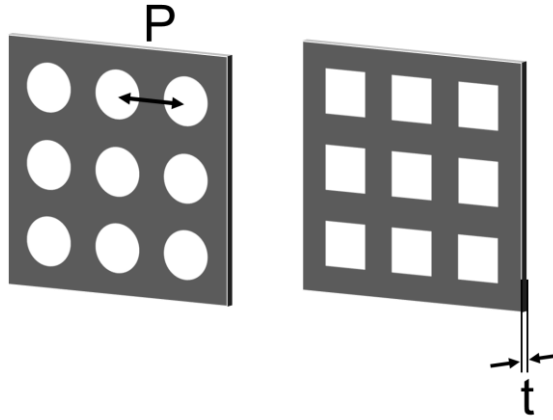


Figure 4: Meta-surfaces with different geometries of meta-atoms arranged in a periodic array and embedded in a frame.

Thanks to their 2D design and ultra-thin structure along the wave propagation direction, meta-surfaces offer a simpler and faster manufacturing process compared to bulky 3D metamaterials. This ease of fabrication has shifted research focus toward developing meta-surfaces that are compatible with modern semiconductor technologies, leveraging existing manufacturing techniques [56]. By carefully choosing appropriate materials and a proper arrangement of meta-atoms with subwavelength thicknesses in propagation direction, undesirable losses can be significantly reduced achieving an absolute transparency [54],[57]. They are capable of manipulating the phase, amplitude, and polarization of electromagnetic waves, which makes them promising candidates for a wide range of applications, such as optical devices, antennas, sensors, and cloaking devices [55]. Moreover, these planar subwavelength structures or meta-surfaces are mentioned to introduce optical properties resembling the DOE rather than bulky refractive optics. Some of the meta-surfaces such as C-shaped meta-atoms that are periodically arranged manipulate the phase of incoming beam which acts as a lens array to create a multiple focal points [58]. And another set of meta-surfaces with V-shaped meta-atoms with periodic array are designed form vortex beams [59] and planar lens with long focal depth along propagation axis [60]. In addition, the meta-surfaces can possess multiple functionalities such as bandpass and bandstop frequency filters, perfect absorbers, polarization converters and as a optical holograms [61]. Figure 5 demonstrates a couple of examples of meta-

surfaces that can act as bandpass frequency selective meta-surface and a meta-surface composed of dielectric nanoparticles achieving full transparency for a selected frequency range.

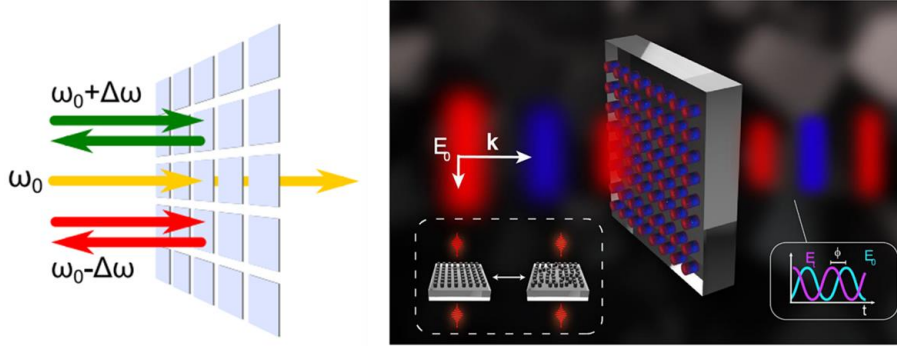


Figure 5: Selected functionalities of meta-surfaces working as a bandpass frequency selective filter (left) and meta-surface composed of dielectric nanoparticles (right) illustrating full transmission (left inset) and phase control (right inset).[61][62]

However, designing a metamaterial/meta-surface based on conductive and semi-conductive materials with full transparency in a wide frequency range is a challenging task due to conductive losses. In addition, achieving full transparency also implies vanishing radiation scattered by individual meta-atoms in the far-field zone even though it may be nonzero in the near-field zone. Moreover, when meta-atoms are arranged in a specific pattern of periodic array, the cross-talk and interaction of electromagnetic fields between neighbouring meta-atoms, known also as a mutual coupling, can occur. When two or more meta-atoms are coupled, the overall collective response of the device increases or decreases depending on nature of the coupling, which in turn changes the resonant characteristics. A proper understanding of such details can be revealed through a multipole expansion of the scattered fields. In the multipole expansion framework, the EM field scattered by a meta-atom in the far zone can be represented by dipole moments such as electric dipole (p), toroidal dipole (T), magnetic dipole (M), electric quadrupole (Q_e) and magnetic quadrupole (Q_m) moments of the meta-atom, respectively. These dipole moments provide a physically significant contribution to the basic characteristics of light-matter interaction. One can observe that the p contribution to the scattered field can be nullified by the T . At such a condition, which is referred to as the “anapole” resonance, where electric dipole radiation in the far zone is suppressed, *i.e.*, in the dipole approximation, the meta-surface does not reflect the incident electromagnetic wave leading to absolute transparency. More detailed explanation on the origin of anapole

resonance is explained in the chapter 2.2. On the other hand, The mutual coupling between meta-atoms can be also explained using a concept of near-field interaction [63]. The near-field interaction between meta-atoms leads to the modification of the resonance bandwidth which in turn changes the quality factor (q -factor). The interaction between two meta-atoms depends on the separation distance, orientation, and polarization of the dipoles which determines the overall behaviour of the meta-surface [63],[64],[65]. The resonance bandwidth of a meta-atom is defined as the ratio between resonance frequency and bandwidth over which the amplitude response is half of its peak value. The analytical approach based on field quantities has been proposed to determine separately the electric and magnetic coupling coefficients which, depending on orientation, may reinforce or may cancel each other and lead to an enhancement of the resonance bandwidth [66]. This enhancement occurs due to the overlapping of the near-field interactions between the meta-atoms, which effectively increases their effective size and modifies their resonance characteristics. Moreover, under presence of mutual coupling behaviour, the near-field interaction between two or more meta-atoms can create additional pathways for energy dissipation and produce radiating losses, leading to the decrease of q -factor. Conversely, meta-atoms can be separated in such way that their field interaction is weak and the q -factor remains high [65]. However, thorough investigation in the THz range is required on such conductive and semi-conductive based meta-surfaces depending on the shape, separation distance, orientation of meta-atoms to achieve a desired EM response with a full transparency.

The design of a single meta-atom with a disk in ring composition has been developed for RF spectrum [67]. The resonator acts as a subwavelength scatterer that supports dynamically induced and spatially confined electromagnetic fields excited individually in a disk and ring integrated in the meta-atom, supporting a anapole state at the frequency of 1.8 GHz [67].The characteristics of such subwavelength structure achieve significant scattering suppression for any polarization and direction of the incident wave. In this work, the performance shift towards the THz range via scaling down of such meta-atom composed of concentric disks and rings connected via inter-bridges is investigated. And the development of meta-surface composed of different number of such meta-atoms possessing two types; one is with metal-based meta-surfaces and other with silicon-based meta-surface which can achieve enhanced transparency for wide THz frequency range was shown in the results section.

2. METHODS AND MODELS

2.1. Finite-difference time domain (FDTD) method

FDTD method involves breaking down an object into a grid of points and iteratively solving Maxwell equations across these points in time domain. This means that the calculation of the EM field values progresses at discrete steps in time. One benefit of the time domain approach is that it gives broadband output from a single execution of the program code; however, the main reason for using the FDTD approach is availability of commercial tools (CST Studio) offering an excellent scaling performance of the method and its ability to model arbitrary structures with high precision widely adapted for solving of different EM problems. The foundational principles of the FDTD method are outlined in the original publication [68].

It discretizes both space and time into small segments to simulate field interactions. Space is divided into box-shaped cells, with electric fields (E-field) located on edges and magnetic fields (H-field) on faces, forming the Yee cell shown in left side of Fig. 6. Time is quantized into small steps, representing the time it takes for fields to travel between cells. Using a leapfrog scheme, E- and H-fields are alternately updated at each time step. When many FDTD cells are combined together to form a three-dimensional volume, the result is an FDTD grid or mesh. By connecting many cell edges with materials, a geometrical structure can be formed within the FDTD grid such as the sphere with volume shown in right side of Fig. 6. Each small box in the sphere shown in the figure represents one FDTD cell. The spacing between cells in the x , y , and z directions can vary across the problem space, enabling a higher density of cell edges in areas with strong fields, such as around small features of highly conductive materials. FDTD simulations can model a wide range of electric and magnetic materials, with the simplest material being free space. By default, all FDTD cells are initialized as free space, and the fields at cell edges are updated using free space equations unless a different material is introduced to replace it. Within, the 3D mesh materials like conductors or dielectrics are added by modifying field computation equations. As an example, if a perfectly conducting material segment is added to the edge of a cell, the equation for computing the electric field is simply set to zero, as the electric field inside a perfect conductor is zero. The cell size, is the most important constraint in any FDTD simulation since it determines not only the step size in time, but also the upper frequency limit for the calculation. In general, a minimum resolution of ten cells per wavelength is required to establish the upper frequency limit. However, in some structures, the cell size

is often made even smaller to capture fine details of the simulated structure, such as the thickness of a substrate or the length of a wire. The fields are updated at each cell location depending on the neighbouring fields in an FDTD grid. However, the grid must end at some point and the fields on the outer edges of the grid must be absorbed by using an absorbing boundary. The performance of the outer boundaries is an important factor in the accuracy of an FDTD calculation and care should be taken to correctly use them. An Excitation, such as sampled waveforms, are introduced at specific locations to the field, while the fields will propagate the introduced waveform throughout the FDTD grid properly, depending on the characteristics of each cell. Simulations run until a state of convergence has been reached, where all the field values have decayed to zero or reach steady-state conditions. All the FDTD simulations in this thesis were done using CST software and the step-by-step procedure of how the simulations were done is shown in the ANNEX. The details of modelling parameters for the elements of MPZP, Waveplates, and 2D resonators are mentioned in the results chapter at their respective sections.

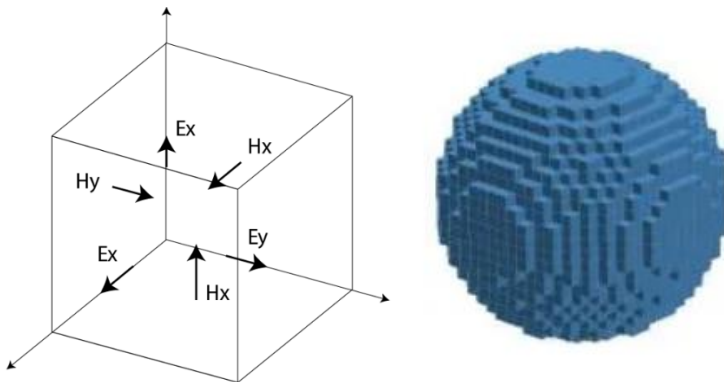


Figure 6: The Yee cell with labelled field components, and finite-difference time domain (FDTD) grid as the sphere with volume by connecting FDTD cell edges.[69]

2.2. Multipole analysis method

The multipole analysis of the system is used to understand nature of the resonance and its broadening behaviour. The multipole analysis consists of fundamental and higher-order modes that describe how EM waves interact with structured materials like meta-atoms and meta-surface. These multipoles arise from multipole expansion or decomposition of scattering fields by long-wavelength approximation (LWA), which mathematically breaks down the

scattered electromagnetic field into different contributions [67],[70]. Indeed, multipoles such as electric quadrupole and magnetic quadrupole in addition to electric dipole and magnetic dipole provides physically significant contribution to the basic characteristics of light-matter interaction. Electric dipole represents the simplest form of charge oscillation, where positive and negative charges oscillate out of phase. Dominates radiation at short wavelengths and is responsible for basic scattering and absorption in plasmonic and dielectric meta-atoms. Magnetic dipole is a circular loop of current, generating a magnetic field. Magnetic dipoles are dominant in the ring-shaped structures or meta-atoms that can strongly couple between neighbouring meta-atoms separated at a subwavelength distance where the quality factor of the whole system resonance decreases. Electric quadrupole is a more complex charge distribution with four charge regions. Quadrupoles contribute to asymmetric scattering effects and directional radiation patterns. Magnetic quadrupole is a higher-order version of the magnetic dipole, featuring more intricate circulating current loops. These modes become prominent when the structure dimensions approach the wavelength of the incident light.

Classical Mie scattering is a theory that describes how spherical particles scatter electromagnetic waves. It is a solution to Maxwell's equations for a plane wave interacting with a spherical structures of arbitrary size and refractive index [71],[72]. Mie scattering applies to all particle sizes and accounts for complex interactions such as resonance effects and higher-order multipole contributions. The scattered field in Mie theory consists of an infinite series of multipole modes (electric and magnetic dipoles, quadrupoles, octupoles... etc.), whose relative contributions depend on the size parameter $x=2\pi r/\lambda$, where r is the sphere's radius.

On the other hand, the LWA considers the wavelength of incident light is much larger than the characteristic size of the scatterer. In this regime, higher-order multipole contributions become negligible, and the scattering behaviour is dominated by the dipole and quadrupole responses. This approximation allows for analytical simplifications, considers only the leading-order dipole terms unlike classical Mie theory for subwavelength structures [70],[73],[74]. LWA approximation can be used in the calculation of the multipole expansion for Optical Anapole structures [67],[75]. An anapole is a non-radiating electromagnetic state that arises from the destructive interference of electric and toroidal dipole moments [76]. This results in a state where the structure interacts strongly with light but does not scatter energy into free space. The anapole mode is unique because, despite significant internal field enhancement, it produces minimal or no far-field radiation. Meta-surfaces,

can be designed to support anapole states by engineering their geometric and material properties. The anapole condition is achieved by adjusting the shape, size, and material of meta-atoms. Common structures include high-index dielectric nanoparticles, nanodisks, and ring-like geometries that support both p and T modes. Tuning the aspect ratio and resonant wavelength can optimize the anapole response. Optical anapoles are typically excited at specific resonant wavelengths, where the destructive interference condition of p and T is met.

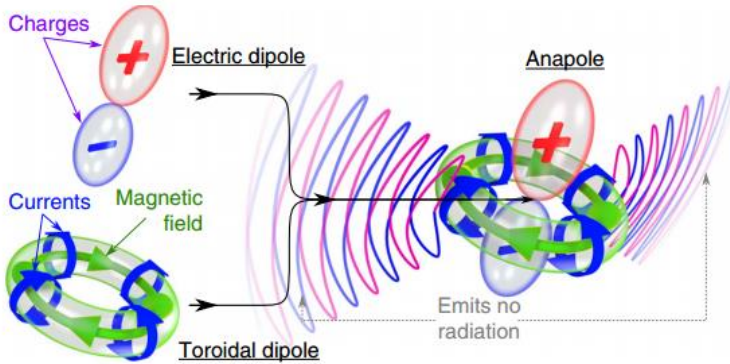


Figure 7: Structural representation of Anapole state that emits no radiation in far-field. Anapole arises when the electric dipole (p) and the toroidal dipole (T) cancels each other due to out of phase superposition.[76]

When the p and T oscillate out of phase, their scattered fields destructively interfere, leading to an anapole state as shown in Fig. 7. The long-wavelength approximation facilitates this analysis by ensuring that only a few leading multipole terms contribute significantly, making it easier to identify and manipulate the toroidal dipole moment [74],[77]. Toroidal Dipole is a nontrivial type of dipole formed by poloidal currents (looping currents circulating around a toroidal core). Unlike an M , a T does not produce a conventional magnetic field outside the structure, leading to unique non-radiating states. Within the long-wavelength limit, the toroidal dipole moment can be understood as a non-radiating current configuration that results from charge and current distributions forming poloidal loops. The T moment arises naturally when considering higher-order corrections to the p term in the multipole expansion. As the design of optical anapole structures requires a multipole expansion, which mathematically breaks down the scattered field into contributions from different multipole moments including toroidal moment. This can be done in either a spherical or Cartesian basis. In a spherical basis, the T moment arises naturally in the multipole expansion.

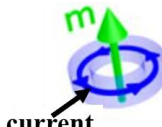
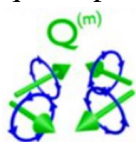
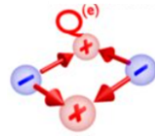
Unlike the Cartesian Taylor expansion, which assumes small sources and can overlook toroidal moments, the spherical basis captures all three families of multipoles (electric, magnetic, and toroidal) more naturally [75]. In the long-wavelength approximation, the Cartesian multipole moments are obtained by expanding the exact spherical expressions in terms of Bessel functions. This allows toroidal multipoles to appear as higher-order corrections beyond the leading-order dipole terms.

To further analyse the role of multipoles in the observed resonance, scattering power for each multipole moment was calculated using Eq. 5. In the multipole expansion framework, the E-field of the EM wave scattered by a meta-atom in the far zone can be presented by the following equation [67],[75],[78]:

$$\mathbf{E}_{\mathbf{n}} = \frac{\omega^2 \mu_0 e^{ikr}}{4\pi r} \left[\mathbf{n} \times \left[\left(\mathbf{p} + \frac{ik}{c} \mathbf{T} - \frac{ik}{6} \mathbf{Q}_e \mathbf{n} \right) \times \mathbf{n} \right] - \frac{1}{c} \left(\mathbf{M} - \frac{ik}{2} \mathbf{Q}_m \mathbf{n} \right) \right] \quad (5)$$

where r is the distance between the observation point and meta-atom, \mathbf{n} is the unit vector in the scattering direction, $k = \omega/c$ is the wavenumber, ω is the angular frequency, μ_0 is the vacuum permeability, and c is the speed of light in the medium surrounding the meta-surface. The multipole moments of the unit-cell introduced in Eq. 5 are defined in the Table 1. All multipole moments are expressed by integrals over particle volume with different moments of the current density \mathbf{j} .

Table 1: Illustration and long wavelength approximation of the multipole moments determining the radiated wave from meta-surface expressed by Eq.5. [67],[78]

<p>Electric dipole moment (p)</p> 	$\frac{i}{\omega} \int_V \mathbf{j} d^3r$
<p>Toroidal dipole moment (T)</p> 	$\frac{1}{10} \int_V [(\mathbf{r} \cdot \mathbf{j})\mathbf{r} - 2r^2\mathbf{j}]d^3r$
<p>Magnetic dipole moment (M)</p> 	$\frac{1}{2} \int_V [\mathbf{r} \times \mathbf{j}]d^3r$
<p>Magnetic quadrupole (Q_m)</p> 	$\frac{1}{3} \int_V ([\mathbf{r} \times \mathbf{j}] \otimes \mathbf{r} + \mathbf{r} \otimes [\mathbf{r} \times \mathbf{j}])d^3r$
<p>Electric quadrupole (Q_e)</p> 	$\frac{3i}{\omega} \int_V \left(\mathbf{j} \otimes \mathbf{r} + \mathbf{r} \otimes \mathbf{j} - \frac{2}{3} (\mathbf{r} \cdot \mathbf{j}) \hat{U} \right) d^3r$

Note for symbols: “.” represents the dot product (scalar product); “ \times ” represents vector product (cross product); “ \otimes ” represents tensor product (outer product) of two vectors r and j .

2.3. Direct laser ablation (DLA) method

DLA method involves the removal of substrate material using high-intensity short duration laser pulses. Under proper fabrication conditions, the light absorption is confined to a small area on the material’s surface. During DLA process, the material absorbs a significant amount of energy, causing it to transition directly from a solid to vapor with minimal thermal transfer and damage to the remaining substrate. The vaporized material is then removed

from the processing area using a technical gas flow. Due to its versatility, the ablation process can be applied to a wide range of materials, including ultrahard substances [79], metals [10],[80], semiconductors [81], polymers [82], and on flexible materials like paper [83] and polymers [84],[85]. In DLA, a laser beam—commonly in the infrared range, with operational wavelength of 1064 nm produced by a diode-pumped solid-state laser—is raster scanned across the sample surface. Overlapping laser spots ensure a smooth processed surface, and the scanning pattern allows for highly flexible processing geometries [30]. While the unit cost of components may be higher than in mass-production techniques like photolithography, the DLA processing significantly reduces the cost of creating unique designs. Raster scanning's main limitations stem from the digital mapping of the processing profile. The scanning speed directly influences processing costs and the design duration for each element.

The DLA technique has shown excellent results in THz science, including the fabrication of binary phase lenses on silicon, metal phase plates, and diffractive optics with integrated bandpass filters [10],[80] as well as the development of antireflective coatings that minimize reflective losses caused by the high refractive indices of semiconductors [28],[52]. The in depth details of DLA method used to fabricate the THz diffractive lenses, HCG-type waveplates, and metal-based meta-surfaces are mentioned at the beginning of each subchapter of the results section. For the silicon-based meta-surfaces which is the last chapter of thesis were fabricated by using electron beam lithography (EBL). The in-depth details of EBL method are mentioned at the beginning of subchapter 3.3 of the results section.

2.4. THz signal measurement and analysis methods

THz imaging setup was used to characterize the performance of MPZP samples. Setup schematically is shown in Fig. 8. Schottky diode based amplification multiplication chain (AMC) from Vignia Diodes Inc. (VDI AMC 346 (VDI MC156) was used as the THz source. An initial 12.083 GHz frequency signal was supplied by the Agilent E8257D generator and the frequency then multiplied 48 times ($6 \times 2 \times 2 \times 2$) to 580 GHz by the AMC. The 580 GHz frequency radiation was then out-coupled from AMC output waveguide via horn antenna (VDI WR 1.5). The resulting output power was around 800 μ W. The radiation from the source formed a diverging Gaussian beam, which was collimated using a refractive HDPE lens and directed to the sample via a flat gold mirror. The focusing performance of the MPZP was evaluated using a THz antenna-coupled microbolometer detector and lock-in

amplifier used for THz signal measurements [86]. A single-pixel detector, mounted on an automated system of three precision traveling stages, was scanned in the xy -plane at the sample's focal plane and in the xz -plane to assess focal depth of lens.

This setup provided information about the signal amplitude at the focal spot, the diameter and position of the focal spot, and the symmetry of the focused beam.

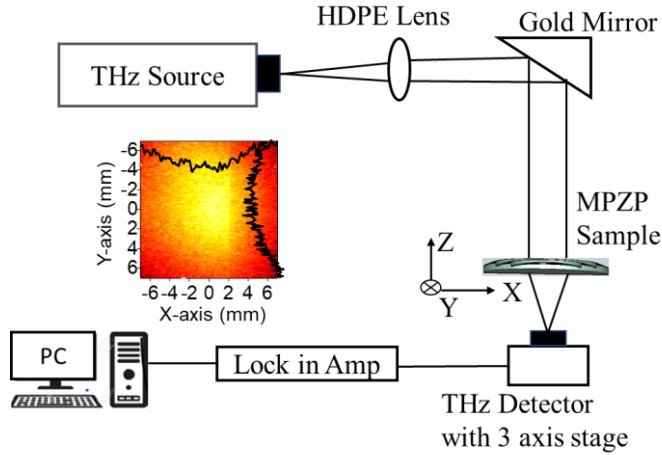


Figure 8: Schematic representation of the experimental setup. Inset shows Gaussian shape of the THz beam emitted from the THz source and measured at the position of MPZP sample. Noise of the THz signal recordings was approximately 0.1 mV, resulting in the noise level of focusing gain to be at about -10 dB.[87]

THz time-domain spectroscopy (THz-TDS) system was used to study material properties in the THz range. The Teravil 'T-SPEC' spectrometer with both transmission and reflection configurations was employed. Measurement schemes are shown in Fig. 9. A femtosecond fiber laser (Toptica, Femtofiber Pro) generating 90 fs pulses at 780 nm and operating at a repetition rate of 80 MHz was used to excite and sample THz pulse radiation via photoconductive antennas made from LT-GaAs.

The THz emitter and detector antennas were designed as coplanar lines made from titanium and gold (Ti/Au), with a linewidth of 20 μm and a spacing of 50 μm between them. The THz detector featured an Hertzian dipole-type antenna with a 6 μm narrow gap located at the center of the coplanar line structure. For more efficient collimation and focusing of THz radiation,

substrate lenses made from high-resistance silicon were attached to the backside of each antenna.

The delay line utilized a hollow retro-reflector moving at 10 times per second, providing a 120 ps time window, corresponding to a spectral resolution of approximately 8 GHz. The THz signal was detected using a digital signal processing (DSP) card integrated into an electronic module featuring an analog-to-digital converter (ADC).

In this method, THz pulses, lasting a few picoseconds, are generated, passed through or reflected by a sample, and then detected in the time domain. The measurement and Fast Fourier transformation (FFT) analysis of THz pulse provide both amplitude and phase information, allowing for a comprehensive study of the material's properties.

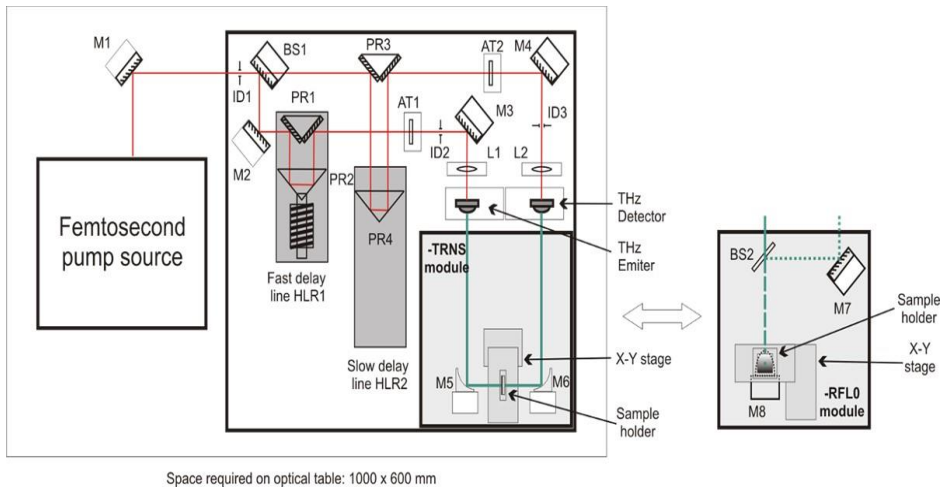


Figure 9: Schematic of THz time domain spectrometer in both transmission and reflection geometry from Teravil 'T-SPEC' terahertz spectrometer (M: mirrors; BS: beam splitter; AT: power attenuator; M5,6,8: parabolic mirrors; PR: prism; L: optical lens).

S-parameter analysis method is used to describe the response of electrical devices to input signal, detailing the relationship between incident and reflected waves at each port. They are essential in characterizing high-frequency components, providing insights into gain, loss, reflection coefficients, and impedance matching. A vector network analyzer (VNA) instrument measures S-parameters of the device under test (DUT) by generating a known signal, directing it through the DUT, and measuring the resulting transmitted and reflected signals. The VNA instrument calculates the

S-parameters, offering a comprehensive frequency-domain analysis of the DUT's performance.

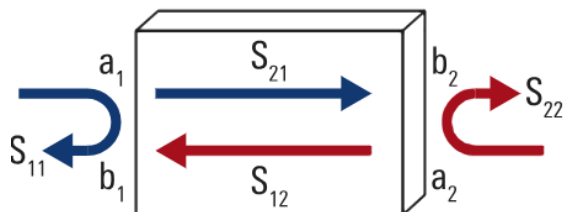


Figure 10: Schematic illustration of device under test (DUT) with two-port network for measuring S-parameters from Rodhe & Schwarz vector network analyzer (VNA).

In the case of the VNA system, several frequency extenders are controlled by a ZVA-24 VNA, over a frequency range of 220 to 1100 GHz. With the first in the range 220 GHz to 325 GHz (WR 3), the second from 325 GHz to 500 GHz (WR 2), the third from 500 GHz to 750 GHz (WR 1.5) and the fourth from 750 GHz to 1100 GHz (WR 1), all from Rodhe & Schwarz. In each case, the output beam is coupled from hollow-core waveguides (VNA ports) to the free space using horn antenna producing a Gaussian beam, fully vertically polarized. Before measuring the samples, the VNA measurements were meticulously calibrated using a set of waveguide Thru/Reflect/Match (TRM) standards. The system was thoroughly calibrated for both spectral bands maintaining a maximum transmission (equal to 0 dB) between transmitter (*Tx*) and receiver (*Rx*). The focus of measurements was to assess the transmission of the sample devices. For a two-port network, the S-parameters are defined as S_{11} (Input port reflection coefficient), S_{21} (Forward transmission coefficient), S_{12} (Reverse transmission coefficient), S_{22} (Output port reflection coefficient). Whereas, a_1 travelling wave incident on port 1, a_2 travelling wave incident on port 2, b_1 travelling wave reflected from port 1, and b_2 travelling wave reflected from port 2 as shown in Fig. 10. These parameters are complex, encompassing both magnitude and phase information, and vary with frequency. S-parameters capture essential details about signal behaviour, including reflection, attenuation, magnitude, and phase, enabling a thorough understanding of a network's performance. S-parameters analysis provides valuable insights into the performance of linear electrical networks such as amplifiers, filters and various RF components.

3. RESULTS

3.1. THz diffractive lenses

The development and research of diffractive optical lenses capable of THz operation using FDTD simulations is the aim of this section. The simulations for all lenses were conducted using a commercial software with the time-domain solver (CST Studio) selected for its relevance to the application. The simulations were performed by choosing a boundary conditions of perfectly matched layer (PML) in order to absorb the transmitted and reflected waves from the structure. Symmetric conditions were enforced in x (perfect electric) and y (perfect magnetic) directions to reduce simulation time and working memory requirements. The calculations were performed assuming the steady-state energy criterion using a multi-frequency plane wave with field amplitude of 1 V/m irradiation onto the sample. The intensity distribution was calculated and analyzed along the optical axis and at the focal plane over a frequency range from 0.1 to 620 GHz. A default hexahedral mesh type is used for the time domain solver, setting up to an average of 6 mesh cells per wavelength. However, there is need for a trade-off between the accuracy of the simulation results and the simulation time, depending on the number of mesh cells defined. The number of mesh cells was chosen to maintain equilibrium. For modelling the Si, a loss-free dielectric was chosen from the material library with properties including a permittivity of 11.9, thermal conductivity: 148 (W/K/m), density: 2330 (kg/m³); and the gold (Au) as a lossy metal with electrical conductivity of 4.56110^7 S/m, thermal conductivity: 314 (W/K/m), density: 19320 (kg/m³).

Binary diffractive lenses in a shape of SZP lens were designed for a specific 300 GHz frequency on a thin 0.1 mm thick gold (Au) metal film. A concentric zone rings (n) that are alternatively transparent and opaque were used to form the SZP lens having a thickness below the wavelength. The focusing gain and focusing performance results were calculated at the focal planes along the optical axis (z -axis) for a designed wavelength of 1 mm by varying the zone number and the F-number or numerical aperture (NA). The F-number is a dimensionless number that represents the ratio of the lens focal length (F) to the lens diameter (D). The NA is inversely proportional to two times of F-number. The following working examples were used to validate model as there is analytical solution for focusing gain of a binary diffractive lens or SZP with different amount of zones, results of which can be compared with FDTD simulations. Selection of design parameters for SZP samples was according

to the Eq. 1. Each zone differs by a phase difference of π , path difference of $\lambda/2$ and period duration of $\tau/2$. Model of the zones used the inner radius with the analytically calculated radius of r_{n-1} and the outer radius with the calculated r_n for the n th zone, continuing with the same step until the desired lens diameter is formed. The completed zone plate was illuminated by a plane wave source at 1V/m along the z -axis.

Effect of Fresnel Zones on Focusing Gain was investigated by FDTD simulations at the frequency of 300 GHz. The focusing gain was defined as the squared ratio between the field amplitude with (E_{MPZP}) and without (E_0) lens under research. The results are summarized in Table 2. The SZP's with the F-number of about 0.5 and a $NA=1$ (*i.e.* the focal length two times smaller than the diameter) demonstrate that the focusing gain of SZP's improves as the zone number increases. For example, for SZP lens with F-number 0.5 and an Fresnel zones or open zones (FZ) number changing from 2 to 32 (*i.e.* $FZ=n/2$), the focusing gain increases from 5.7 to 1032.3 value.

Table 2: Effect of zone number on focusing gain of the SZP lens found from FDTD simulations

Open Zones (FZ)	Analytical focal length / Diameter at 300 GHz in mm	E-field (at 300 GHz) @ focal length in mm	Focusing Gain (dB)
2	4.8/9.6	2.4V/m@4.8	5.7
4	9.6/19.2	4.0V/m@9.6	16.0
8	19.3/38.6	9.1V/m@19.3	82.7
16	38.6/77.2	18.3V/m@38.6	334.9
32	77.2/154.5	32.2V/m@76.2	1032.3

Effect of F-number on focusing performance of a lens is a measure of the lens's aperture, which controls the amount of light that enters the lens and reaches to the receiver side. The focusing performance of the lens was estimated in terms of the cross sections of the focused E-field along the xy -plane. Simulated results for a lens with $FZ = 4$ and F-number = 0.5, 1, and 2 or $NA= 1,0.5$, and 0.25 at 300 GHz frequency are shown in the Table 3. It is seen that the E-field at the focal point is almost the same for all F-number. On the other hand, the full width at half maximum (FWHM) of the focused E-field decreases when the F-number gets close to zero.

Table 3: Effect of F-numbers on Focusing Performance

F-number	E-field @300GHz	Focusing Gain (dB)	FWHM (mm)
0.5	4.0 V/m	16.1	0.9
1	4.1 V/m	16.5	1.8
2	4.1 V/m	16.6	2.5

It can be concluded that, as the number of Fresnel zones increases, the focusing gain improves and a diffractive lens focuses the radiation better than a lens with high F-number. Such lenses are used for point-to-point imaging applications and the fabrication of compact optical devices due to their small focal length.

Working frequencies of diffractive lenses is important characteristic. As the performance of diffractive lenses is wavelength depended, the operational bandwidth is much narrower compared to the conventional refractive lenses as explained in section 1.1. Nevertheless, diffractive lenses can be used for a quite range of frequencies. Table 4 shows the functioning dependence of diffractive lenses at different frequencies for different F-number for designed frequency of 300 GHz. For this, in simulations more E-field monitors are set up in multiples of designed frequency at 300GHz, *i.e.* for the frequencies of 450 GHz and 600 GHz. It is seen that the E-field at the focal point is almost the same for all the three mentioned frequencies. Thus, the diffractive lens can work for higher range of frequencies upto 1.5 to 2 times of designed frequency making them suitable for broadband THz imaging applications.

Table 4: Working frequencies of Diffractive lenses

F-number	E-field @300GHz	E-field @450GHz	E-field @600GHz
0.5	4.0 V/m	4.9 V/m	4.9 V/m
1	4.1 V/m	5.0 V/m	5.0 V/m

As said in the literature review section 1.1 the SZPs has only 10% of focusing efficiency and to improve the efficiency of a zone plate or lens we have moved to MPZP. In the coming sections we talk about the improvement of focusing efficiency of a lens.

Multi-Phase Zone Plates (MPZP)

In this section we focus on design and development of MPZP capable of terahertz operation using FDTD simulations. It is obtained by making the SZP opaque zones into transmissive and phase-reversing for the waves going through them.

MPZP are designed for a specific frequency (300 GHz) on silicon with n being zone rings and Q being sub-zones that are almost entirely transparent to the incident THz radiation. Now, model the MPZP by defining the inner radius of zone with the calculated radius of r_{n-1} and the outer radius with the calculated r_n for the n^{th} zone using Eq. 2, along the z -axis. Now, to modify the phase of incoming radiation to constructively interfere the phase difference must be created by determining a depth (d) using the Eq. 3, to each Q . For example, the MPZP with $Q = 4$, in which each sub-zone differs by a phase difference of $\pi/2$, and path difference of $\lambda/4$ *i.e.* with 0-, 90-, 270-, and 360-degree phase steps in each full-wave Fresnel zone. The depth for successive sub-zones are produced by 0, d , $2*d$, and $3*d$ in depth, correspondingly. The simulations with the mentioned parameters in the beginning of section 3.1 were used to analyse the focusing performance of MPZP lens.

Change of refractive index on MPZP: This section gives a fair idea about the focusing performance of MPZPs with two different refractive indices, MPZP with an index of 1.5 and another MPZP with a index of 3.45 for a designed frequency of 300GHz. Figure 11 shows the field distribution along the optical axis of MPZPs for F-number = 1 or $NA= 0.5$ with $FZ=4$ and $Q=4$. The focal distance for both MPZPs was found to be at around 30 mm along optical axis and a similar field amplitude of approx. 17 V/m. However, the thickness along the optical axis has been significantly reduced for MPZP with refractive index 3.45 compared to MPZP with a refractive index of 1.5.

The depth of each sub-zone in the MPZP, which is critical for phase reversal, is primarily determined by the material's permittivity as per Eq. 3. Higher permittivity leads to shallower sub-zone depths, resulting in a reduced overall thickness of the MPZP. Despite this, pronounced standing waves were observed inside the MPZP due to internal reflections for which the edges of the MPZP acts as a Fabry-Perot cavity because of its high refractive index. To assess whether these standing waves affect the focusing performance, further investigations were conducted by varying the MPZP thickness relative to a fraction of the incident wavelength. These findings are discussed in the subsequent section.

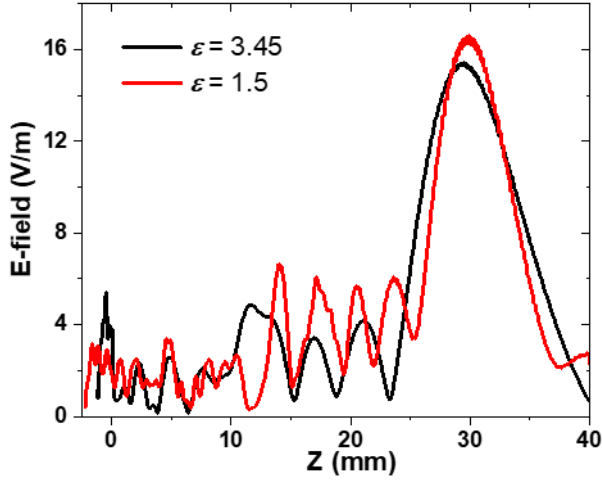


Figure 11: E-field distribution along optical axis of the multi-Phase Zone Plates (MPZP) with FZ= 4 and $Q = 4$ subzones; for a designed frequency (300 GHz) for refractive index = 3.45 & 1.5.

Optimization of standing waves inside the substrates: To study the effect of standing waves on focusing performance of MPZP, we consider the initial thickness of MPZP 0.5mm with a refractive index $\epsilon = 3.45$, FZ= 2, and $Q = 4$ at a designed frequency of 300 GHz. Now, the simulations were performed with double the initial thickness of MPZP, *i.e.* 1mm and thereby gradually increasing the thickness relative to the fraction of wavelength inside the MPZP ($\lambda_{in} = \frac{\lambda}{\epsilon}$) with a step size of 0.036 mm (*i.e.* $\frac{\lambda_{in}}{8}$). Figure 12 shows the field distribution along the optical axis with a change in physical thickness of MPZP. The focal distance for all the MPZPs was found to be at around 16 mm along optical axis and a similar field amplitude of approx.8 V/m. Figure 12 shows the occurrence of standing waves inside MPZP due to internal reflections until or around 1mm. The plate with a MPZP thickness of 1.0725 mm (blue line) shows a minimal amplitude of standing waves compared to MPZPs with other thickness. Nevertheless, we see no deterioration of E-field amplitude at focal length with optimizing the standing waves stating that the occurrence of standing waves doesn't affect the focusing performance of MPZP at the focal distance.

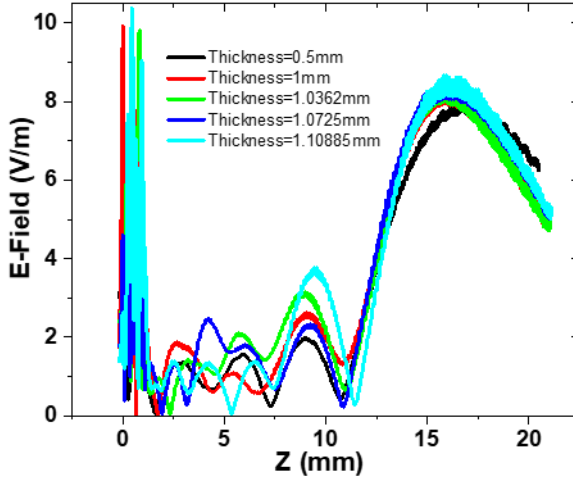


Figure 12: E-field distribution along optical axis of the MPZP for a designed frequency (300 GHz) for $FZ=2$, $Q=4$ and F-number = 1 by varying the thickness from 1mm to 1.10885 with a step size of 0.036 mm (*i.e.* $\frac{\lambda_{in}}{8}$).

Side of Incidence on MPZP: Further, we have investigated effect on focusing performance of MPZPs based on the direction of incidence of light. MPZP for F-number = 1 or $NA=0.5$ with a thickness of 0.5mm, with a refractive index of $\epsilon=3.45$, $FZ=4$, and $Q=4$ at a designed frequency of 300 GHz are consider. A multi-frequency plane wave with field amplitude of 1 V/m irradiated onto the MPZP from the side of circular rings (front side) and from the side of smooth surface (back side) of MPZP. Interestingly, we see no difference in the field distribution along the optical axis irrespective to the side of incidence shown in Fig. 13 The focal distance was found to be at around 30 mm along optical axis and a similar field amplitude of approx. 16 V/m. However, we see no difference in E-field amplitude at focal length and change of focal performance of MPZP based on the side of incidence giving a confidence that MPZP lens can focuses the radiation irrespective to the side of incidence.

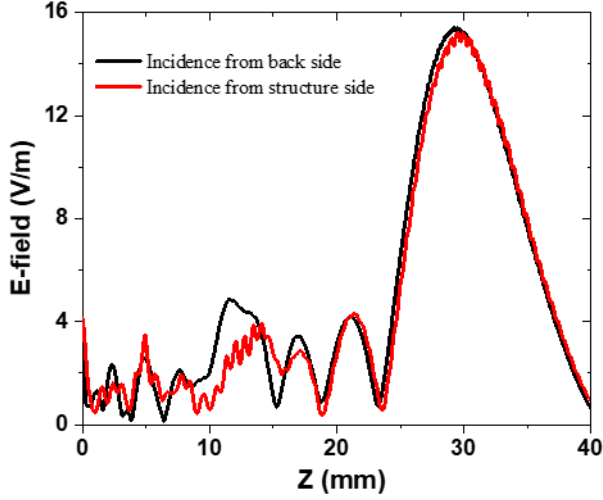


Figure 13: A example of finite-difference time domain (FDTD) calculation for an MPZP lenses with $FZ= 4$ and $Q = 4$ subzones for F-number =1; E-field distribution along optical axis of the MPZP for a designed frequency (300 GHz), (black) when the THz radiation is incident from the Substrate side and (red) when the THz radiation is incident from the Rings side.

Polarization dependence on MPZP:

In addition, we have investigated the polarization dependence on focusing performance of MPZPs. MPZP for F-number = 1 or $NA = 0.5$ with a thickness of 0.5mm, with a refractive index of $\epsilon= 3.45$, $FZ= 4$, and $Q = 4$ at a designed frequency of 300 GHz are consider. A multi-frequency plane wave with E-field amplitude of 1 V/m irradiated onto the MPZP along x -axis and y -axis respectively. Interestingly, we see no difference in the field distribution along the optical axis irrespective to the polarization of incidence shown in Fig. 14. The focal distances for both the orthogonal polarizations were found to be at around 30 mm along optical axis and a similar field amplitude of approx. 16 V/m. We observe no difference in E-field amplitude at the focal length and no change in the focal performance of the MPZP lens based on the polarization of light. This confirms that MPZP lenses are not polarization-sensitive and can focus radiation regardless of the polarization of incidence.

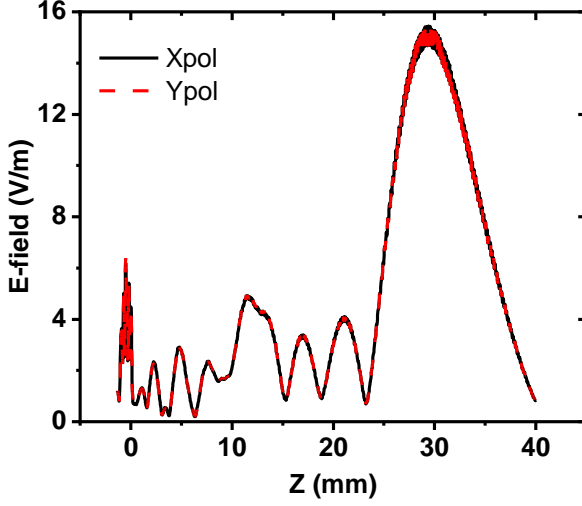


Figure 14: A example of FDTD calculation for an MPZP lenses with FZ= 4 and $Q = 4$ subzones for F-number =1; E-field distribution along optical axis of the MPZP for a designed frequency (300 GHz), (black) when the THz radiation is x -polarized and (red) when the THz radiation is y -polarized.

Hybrid Multi-Phase Zone plates (H-MPZP)

In this section, the hybrid multi-phase zone plates (H-MPZP) were developed on Si wafer for radiation focusing at the selected frequency of 585 GHz with F-number = 1 or $NA = 0.5$. Notably that the diffraction efficiency of Si-based MPZPs with large Q value can reach almost 100% [25]. However, manufacturing of the MPZP with large number of phase quantization levels is challenging task because the complexity of step profile increases going towards the outer zones [26]. To realize the H-MPZP, we modified the design of initial MPZP with the FZ=3 and $Q=8$, which has been previously demonstrated to be a good trade-off between fabrication time, design complexity, and focusing performance [25]. The H-MPZP was designed similar to MPZP using the Eq. 2 for defining the inner radius of zone with the calculated radius of r_{n-1} and the outer radius with the calculated r_n for the n^{th} zone. And the depth of single subzone, d , was described by Eq. 3.

In a case of initial MPZP, the parameter d was calculated from the Eq. 3 with $Q=8$ for selected frequency 585 GHz. However, for H-MPZP, the depth of sub-zones was varied with respect to the used value of Q . Figure. 15a demonstrates a step profile of initial design of MPZP with $Q = 8$ from which

the hybrid samples were developed with smaller amount of phase quantization levels in most outer zones (see Fig. 15b, c). Each set of the Fresnel zones is indicated by different colour bar at the bottom of Fig. 15a-c. Microscope pictures of the fabricated samples are shown in bottom row of Fig. 15a-c. Two hybrid lens designs were obtained after modification Q from 8 to 4 value in one set of Fresnel zones 3 (FZ 3) and in two sets of zones 2, 3 (FZ 2, FZ 3) labelling these samples as H-MPZP 1 (see Fig. 15b) and H-MPZP 2 (see Fig. 15c), respectively. The MPZPs were fabricated by DLA techniques (see section 2.3) patterned by an industrial-scale pulsed laser (Atlantic 60, EKSPILA UAB) with a pulse duration of 10 ps, operation wavelength of 1064 nm, scan speed of 856 mm/s (47 % spot overlap), 32 μm laser spot size diameter, 11.8 J/cm^2 laser irradiation fluence, hatch angle rotation of 45 deg after each scan and etch depth of 0.2 μm per layer which allowed to maintain precise control over the profile shape of the MPZPs.

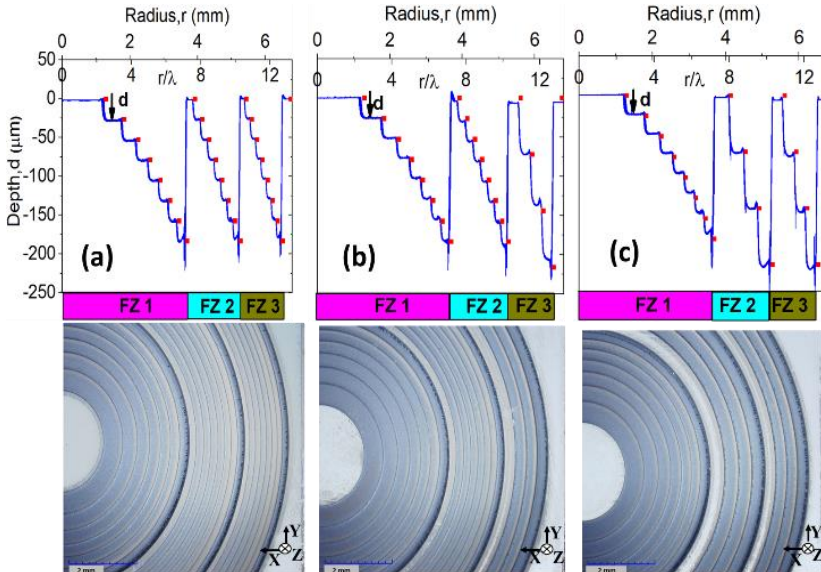


Figure 15: The step profile across centrum line (top row) and microscope picture (bottom row) of the fabricated samples of (a) initial design MPZP with $Q=8$ for all Fresnel sub-zones; (b) optimized H-MPZP1 with $Q = 4$ and $m = +3$ at the most outer sub-zones area FZ3; and (c) optimized H-MPZP2 with $Q = 4$ and $m = +3$ at both FZ2 and FZ3 areas. The step profile for each sample was taken from the numerical design (Red dots) and measured by a "Veeco Dektak 150" profilometer (Blue line).[87]

A FDTD method using CST software was used to analyse and optimize the focusing performance of the MPZP samples. To achieve similar or better focusing performance for H-MPZP samples as those of initial design of MPZP sample we have done some optimization on depth of sub-zones (d) using Eq. 6.

$$d = \frac{\lambda}{Q(\varepsilon - 1)} \left(1 + \frac{m}{8}\right) \quad (6)$$

here m is integer number value.

The optimization of phase profile in the selected outer Fresnel zone areas of the H-MPZP samples was performed by using a discrete step size of one eighth ($m/8$) of depth initial value at the subzone area in Eq. 6 until the lens reached maximum value of the focusing gain. For this reason, an integer m value was varied in the range from -4 to $+4$, which corresponds to a phase change of $\pi/12$ for the selected wavelength. The optimization results in terms of the focusing gain, beam size, focal distance, and F-number of the MPZP samples with hybrid phase profile in respect to the initial MPZP as a function of optimization factor (m) are shown in Fig. 16.

The change of the depth in sub-zones modifies the lens performance independently on the hybridization order of H-MPZP samples. Larger focusing gain was found by making the depth of subzones deeper for both hybrid design lenses than the actual subzone depth instead of making them shallower (see Fig. 16a). The maximum gain was found when the optimization factor of $+3$ was added to the actual subzone depth of H-MPZP1 and H-MPZP2 samples, which corresponds to the phase increment of $\pi/4$. Moreover, we clearly see the reduction in full-width half maximum (FWHM) of focused beam size at the same $m = +3$ (see Fig. 16b). In addition, Figs. 16c, d demonstrate the modification of focal length and F-number with very similar values as for the standard MPZP sample with $d = 26 \mu\text{m}$, when the optimization factor for H-MPZP samples is of about three eighths of the actual subzone depth. *i.e.* $m = +3$. It is worth to note that the maximum gain for initial MPZP samples is achieved when $m = 0$, *i.e.* the performance of initial design diffractive lenses is optimal in terms of focusing gain, therefore, analytical Eq. 3&6 accurately describe geometry parameters of the MPZP.

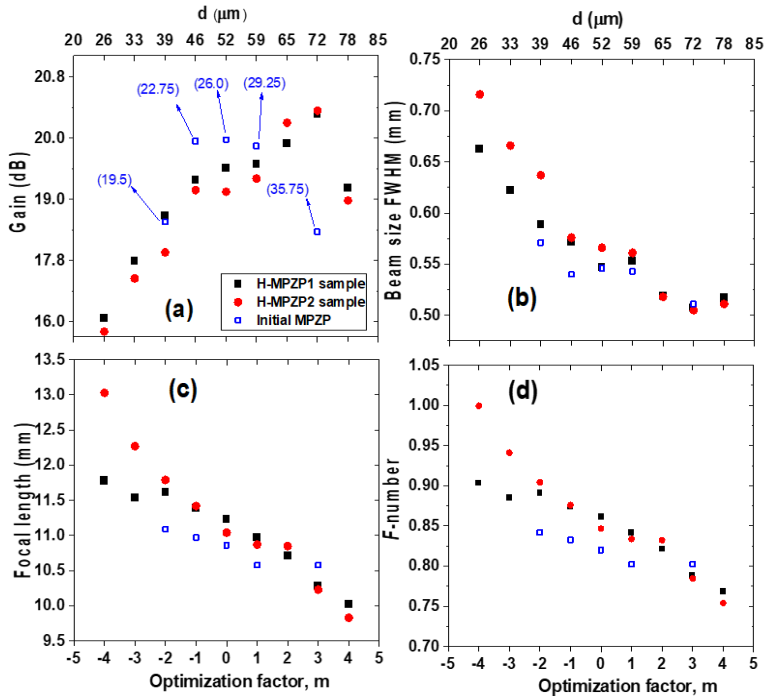


Figure 16: The simulated focusing gain (a), full-width half maximum (FWHM) (b), focal distance (c), and F-number (d) of the initial MPZP, H-MPZP1 and H-MPZP2 samples with different value of the optimization factor (m), bottom x -axis, and resulting depth of subzones, d , top x -axis. Inset: numbers in brackets, which are shown only in (a), indicate actual d value in micrometres of subzones with respect to the optimization factor for the standard MPZP samples.[87]

Figure 17 shows simulated focusing gain characteristics obtained for the initial MPZP, H-MPZP1 and H-MPZP 2. The gain value without considering a reflection loss was found to be of about 20 dB (about 100 times) which agrees with data obtained from analytical performance description of the MPZP used.

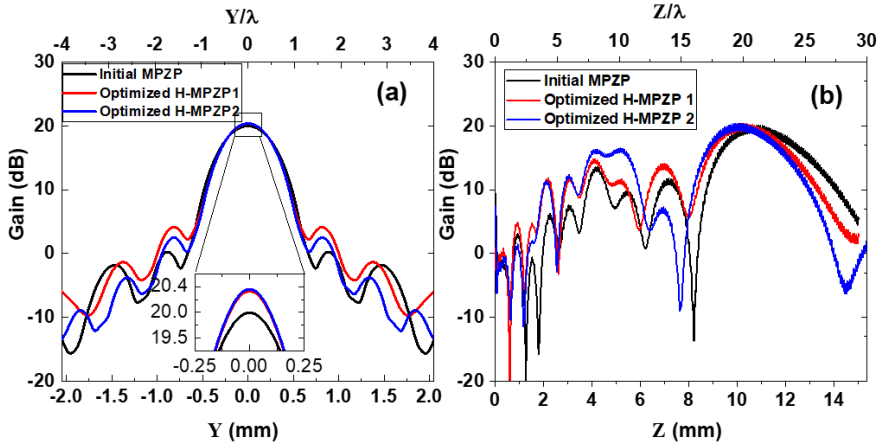


Figure 17: The simulated focusing gain characteristics at focal plane (a) and along optical axis (b) for the initial MPZP sample and two optimized H-MPZP1 and H-MPZP2 samples with the same parameters as in Fig. 15. The results are shown in semi-log scale, where $\text{dB} = 10 \log(\text{Gain})$. Inset shows the gain characteristics of the same samples in linear scale in zoomed area. Note, bottom axis is in millimetres, whereas top is normalized to the design wavelength λ . [87]

Numerical optimization results are summarized in Table 5. The H-MPZP1 and H-MPZP2 samples with factor $m = +3$ demonstrated maximum focusing gain and were treated as optimal design lenses, resulting in up to 10 % (+0.4 dB) higher gain in comparison to the initial MPZP (see also red and blue curves in Figs. 17a, b). The increase in focusing gain for the optimized H-MPZP samples was due to a constructive interference of the wavefront thanks to precise control over a phase shift of incoming radiation. Further increase in the sub zone depth, cases $m > +3$, resulted in the destructive interference and reduction of the focusing gain and FWHM values.

Moreover, from the results shown in Fig. 17a, we clearly see a change of sidelobe level from 0.23 dB for standard MPZP to 4.05 dB for H-MPZP1 sample with an increase of absolute focusing gain at the central beam by up to 10% (+0.4 dB). Further modification of the hybrid lens design from H-MPZP1 to H-MPZP2 resulted in two times smaller sidelobe magnitude (2.48 dB) maintaining approximately the same focusing gain values at the central beam (see Table 5).

Table 5: Summary of the modelling results[87].

Sample	Depth d @ outer sub- zones (μm)	FWHM (mm)	Focusing Gain (dB)	F- number
Initial MPZP with $Q=8$ at FZ=1,2,3				
Initial MPZP with $m=0$	26	0.55	20.0	0.82
Optimized H-MPZP with $Q=4$ at FZ=3; $Q=8$ at FZ=1,2				
H-MPZP1 with $m=+3$	72	0.51	20.3	0.78
Optimized H-MPZP with $Q=4$ at FZ=2,3; $Q=8$ at FZ=1				
H-MPZP2 with $m=+3$	72	0.51	20.4	0.78

Three samples in total, two of optimized design (H-MPZP1 and H-MPZP2) and one initial MPZP design were fabricated for operation at the frequency of 585 GHz. The step profiles of each sample scanned with "Veeco Dektak 150" profilometer demonstrate good fit to the design shape as shown from centre towards edge side in top row of Fig. 15.

The outer sub-zones become increasingly narrower with growing distance from the centre in a initial design MPZP. Therefore, a small spot size of the laser beam is needed to produce large diameter lens and ensure sufficient fabrication resolution in the outer zone areas. Whereas the outer sub-zones in the H-MPZPs are wider but a bit deeper. Although the removed material volume in the initial MPZP lens is smaller than that in the H-MPZP, the feasibility to use large diameter laser beam leads to faster and less demanding fabrication process of those lenses. For example, if we consider the narrowest ring of the initial and hybrid MPZP design to be respectively of 192 μm and 345 μm , then we increase proportionally the laser spot and 1.8 times faster fabricate hybrid MPZP of optimized design.

Focusing performance of the samples was explored experimentally by using a THz continuous wave system operating at 585 GHz frequency. Setup is shown in section 2.4 where the composition of setup was explained. The measurements were done scanning with the THz detector placed on an automated 3D axis stage. This allowed us to evaluate the intensity distribution along the optical axis (z -axis) and in the focal plane (x - and y - directions) in respect to the sample.

The measurements revealed a incidence beam with a Gaussian shape polarized along y -axis at the sample plane in experiments with FWHM=14 mm (see inset in Fig. 8). Notably, the plane wave excitation was used in the numerical simulation resulting in overestimated gain values in comparison to the experimental data. We would assume that the aperture efficiency with the reflection losses in our experiment was within the range of 38 %.

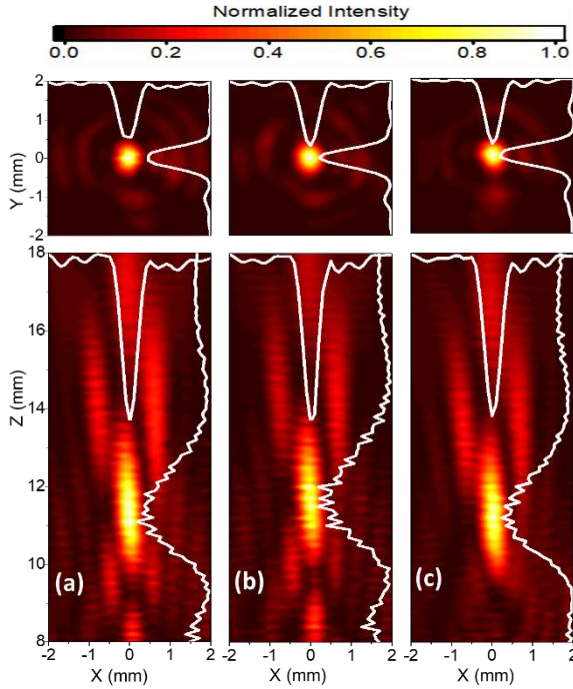


Figure 18: THz beam intensity distribution measured at the focal plane (xy plane) and along the optical axis (xz plane) with respective cross-section of focused beam for the fabricated (a) Initial MPZP, (b) Optimized H-MPZP 1, and (c) Optimized H-MPZP 2 samples.[87]

Experimental data of the THz beam focusing with different samples are shown in Fig. 18. The focal distance was found to be at around 12 mm (z -direction) similar for all samples. We see that the beam is perfectly focused as an Airy disc seen in the focal plane as the side lobes around the central focal spot. The increment in intensity was found in experiment up to $\sim 10\%$ (+0.4 dB) for the H-MPZP samples compared to the standard MPZP. It is worth to note that the

magnitude of the intensity change was found the same as predicted by numerical modelling.

Figure 19 demonstrates the focusing gain characteristics obtained experimentally and numerically for different lens samples at focal plane. Both hybrid design lenses demonstrated the same F-number and the focusing gain approx. 10% (0.4 dB) higher than values achieved with the initial MPZP samples.

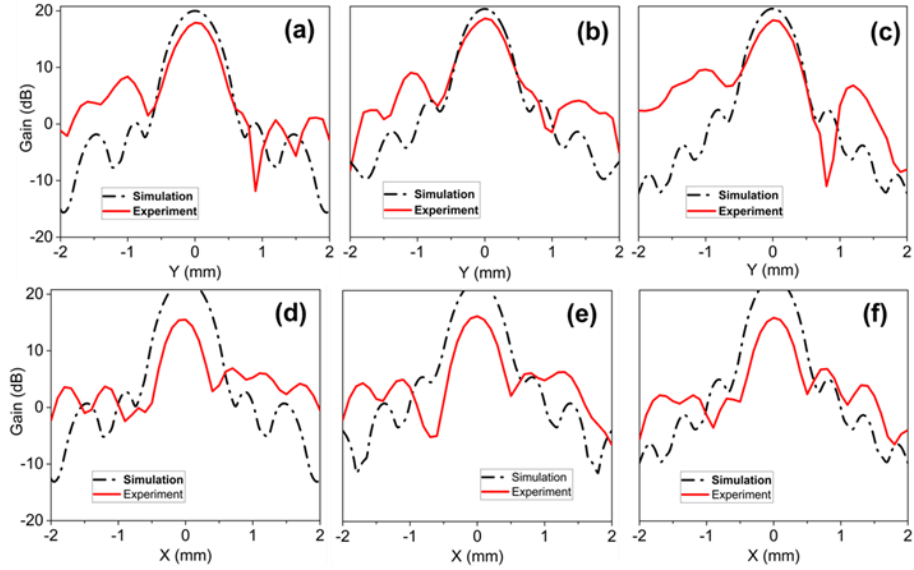


Figure 19: The focusing gain in semi-log scale obtained experimentally (solid red lines) and numerically (dot-dashed black lines) at the focal plane for the y -axis and x -axis (a,d) Initial MPZP; (b,e) Optimized H-MPZP 1 and (c,f) Optimized H-MPZP 2 samples.[87]

Detailed comparison of experimental and modelling results for fabricated samples are done in Table 6. The first columns of the simulation and experimental data show the focused beam FWHM measured along x - and y -axis direction. As the diameter of the MPZP lens is almost equal to its focal length with a angle being 26 degrees *i.e.* angle of the maximum cone of light focused by the MPZP lens. With such high angle of which the light is focused said to be a non-paraxial lens with high NA which possess elongation of FWHM of a focused beam along the direction of polarization. From the beam width percentage ratio, B , of beam size of hybrid, $FWHM_H$, to the beam size of initial, $FWHM_i$, design samples, *i.e.* $B = FWHM_H / FWHM_i$, we conclude that the focused beamwidth of optimized H-MPZP samples is narrowed by up

to 8 % compared to the initial MPZP in simulation, whereas from the experimental data, a similar change of FWHM values were found. The comparison of focusing gain was evaluated as the attenuated gain, A , indicating the ratio between the focusing gain of initial, G_i , and hybrid, G_H , design MPZP samples, *i.e.* $A = G_i / G_H$. Here $A < 1$ indicate the focusing gain of hybrid design lens to be higher in comparison to initial design MPZP. By comparing the A values, we clearly see that the optimized H-MPZP samples demonstrated slightly better focusing performance both in theory and in experiment. It is worth to mention, that by measuring the ratio between intensities at the focused beam centre and at the side of 1st order lobe, the diffraction efficiency was estimated to be of about 93 % (98 %) in experiment (in modelling), value of which was in agreement with analytical description of the MPZP [26]. Moreover, in the initial and hybrid lens designs, the narrowest ring width is 192 μm and 345 μm , respectively. By proportionally scaling the laser spot diameter to match the increased feature size in the hybrid design, the fabrication process is significantly accelerated. Specifically, the optimized hybrid MPZP lens enables a 1.8-fold reduction in fabrication time compared to the initial design, while maintaining the optical performance.

Table 6: Summary of experimental and simulation values of the FWHM and focusing gain for the fabricated MPZP samples [87].

Sample	Simulation			Experiment		
	FWHM _y (mm)	FWHM _x (mm)	Focusing Gain / dB	FWHM _y (mm)	FWHM _x (mm)	Focusing Gain / dB
Initial MPZP	0.55	0.55	99.0/20.0	0.50	0.41	61.7/17.9
Optimized H-MPZP 1	0.51 (B=0.92)	0.51 (B=0.92)	108/20.3 (A=0.91)	0.53 (B=1.06)	0.45 (B=1.09)	73.5/18.7 (A=0.84)
Optimized H-MPZP 2	0.51 (B=0.92)	0.51 (B=0.92)	109/20.4 (A=0.90)	0.50 (B=1.00)	0.44 (B=1.07)	68.2/18.3 (A=0.90)

We can also see from Table 6, a noticeable change in the focusing gain about 6 % and beam size about 6 % in the experiment values for optimized H-MPZP 2 compared to optimized H-MPZP 1 samples. Such differences were in the range of experimental errors. Moreover, the operation bandwidth at 3dB level was found to be of approx. 200GHz for all MPZP shown in Fig. 20.

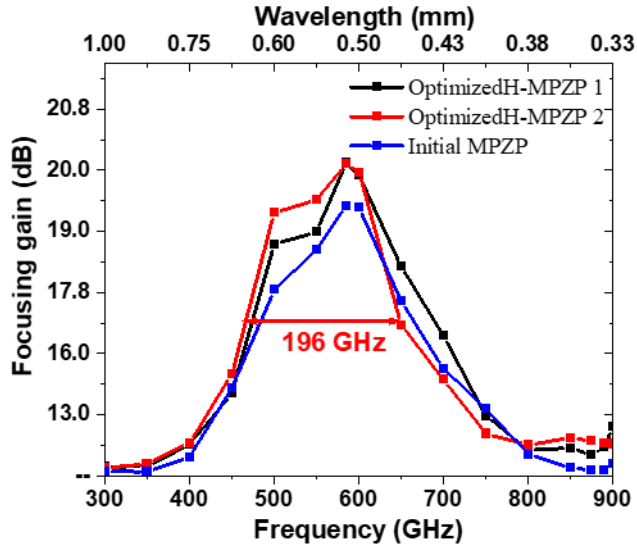


Figure 20: Operation bandwidth at 3dB level for initial MPZP (blue), optimized H-MPZP 1 (black), and optimized H-MPZP 2 (red).

Thus, obtained results validate a successful optimization process of the hybrid lenses with reduced complexity of phase profile. The H-MPZP samples demonstrated in experiment slightly better focusing performance as those of initial design of MPZP samples. The increment in the focusing gain of hybrid lenses was attributed to smaller shadowing effects and more efficient constructive interference of the spherical wavefront because of precise control over the phase shift of incoming radiation at the outer Fresnel zones by making them deeper [88][89]. Achieved overall focusing gain, which was not a concern of this research work, from the optimized H-MPZP samples was up to 18.7 dB (20.4 dB) in experiment (numerical modelling), can be further increased with larger amount of the Fresnel zones [26].

3.2. HCG-type Waveplates

We developed the HCG-type waveplate with an anti-reflective design of HRFZ-Si wafer targeting operation as QWP and HWP in a wide spectrum range from 0.1 THz to 1 THz. The transmission amplitude and phase characteristics of waveplate samples were modelled numerically and measured experimentally, the results of which are discussed in this section.

FDTD simulations were performed to optimize the HCG-type waveplates transmission and phase spectra, using a commercial solver (CST Studio) discussed in previous section. Simulations were carried out using a normal illumination of plane wave by choosing a perfectly matched layer boundary condition to absorb the transmitted and reflected waves from the structure. A default tetrahedral mesh type is used for the frequency domain solver, setting up to an average of 15 to 20 mesh cells per wavelength with a unique feature in the software using adaptive mesh refinement. The S-parameter calculations were performed for both orthogonal TE and TM polarizations assuming the steady-state energy criterion using a multi-frequency plane wave incoming onto the sample.

The selected waveplates were fabricated using DLA method implemented by an industrial-scale pulsed laser (Atlantic 60, EKSPILA UAB) under operation of wavelength of 1064 nm, 32 μm laser spot size diameter, pulse duration of 10 ps, 11.8 J/cm² laser irradiation fluence, scan speed of 856 mm/s (47% spot overlap), hatch angle rotation of 45 degrees after each scan and etch depth of 0.2 μm per layer which allowed to maintain precise control over the structure. The transmission spectra of the fabricated waveplate samples were measured by THz-TDS system and compared to the simulation data. The samples were characterized in the frequency range of 0.1–2.0 THz at a room temperature. The phase retardation or phase retardation ($\Delta\phi$) of a waveplate was found calculating the difference of phase from the orthogonal polarizations. Moreover, VNA measurements were also carried out over a frequency range of 220 to 1100 GHz to study the transmission characteristics of a waveplate and to prove the repeatability of waveplate performance. Various wide range waveguides and frequency extenders were employed to achieve this frequency coverage. The incident beam from the WR waveguides were out-coupled to free-space using waveguide horn antennas, further manipulated through two parabolic mirrors before and after passing through the sample similar to the THz-TDs experiment.

Design of flat profile single-sided HCG-type waveplate: At first, single-sided monolayer HCG-type waveplate was developed with a subwavelength periodic material-air interfaces with a period of $P = 100 \mu\text{m}$ on top of a HRFZ-Si wafer with an overall thickness of $t = 250 \mu\text{m}$ with design parameters shown in Fig. 21a. The grating height of a waveplate was kept at $h = 50, 100, 200 \mu\text{m}$ i.e the height from the top of the ridge to the bottom of the groove. The width of the top of the ridges was kept at $w = 50 \mu\text{m}$, resulting in sidewall inclination on each side of 11 degrees. We call the E-field along grating axis as TM and perpendicular to the grating axis as TE modes (see Fig.

3). The required $\Delta\varphi$ between TE and TM orthogonal polarizations can be achieved by carefully choosing the proper height and width of a grating ridges. The grating profile and microscopic image of a fabricated waveplate is shown in Fig. 21b, c.

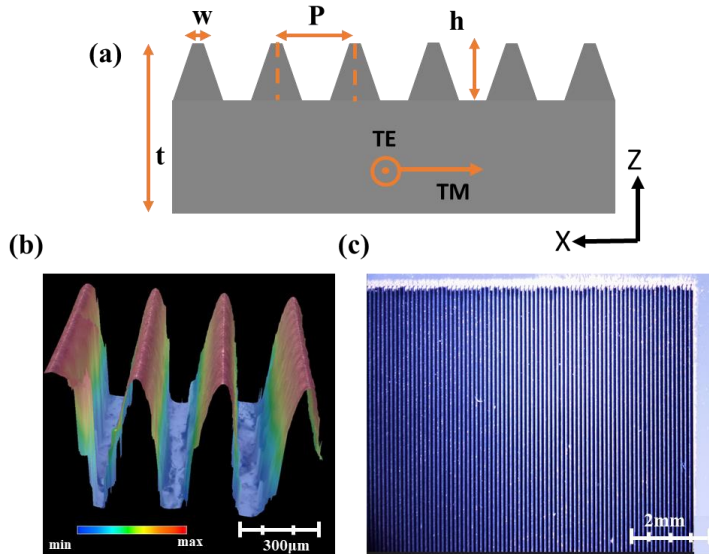


Figure 21: The images of single-sided high contrast gratings (HCG)-type waveplate; (a) shows the 2-D representation of a waveplate along xz -plane with design parameters, (b) grating profile was shown in colour scale along xz -plane taken from the optical profilometer, showing grating ridges (red) and grating grooves (blue), (c) microscopic images of a waveplate along xy -plane.[46]

The results of transmission and phase retardation of a single-sided HCG-type waveplate for the samples with $h = 50, 100, 200 \mu\text{m}$ for two orthogonal polarizations (TE and TM) are shown in Fig. 22. For both the polarizations the incoming light interacts with the flat surfaces of the structure. Due to strong internal reflection because of high refractive index, standing waves form within the waveplate with corresponding well known Fabry-Perot periodic spectral characteristics.

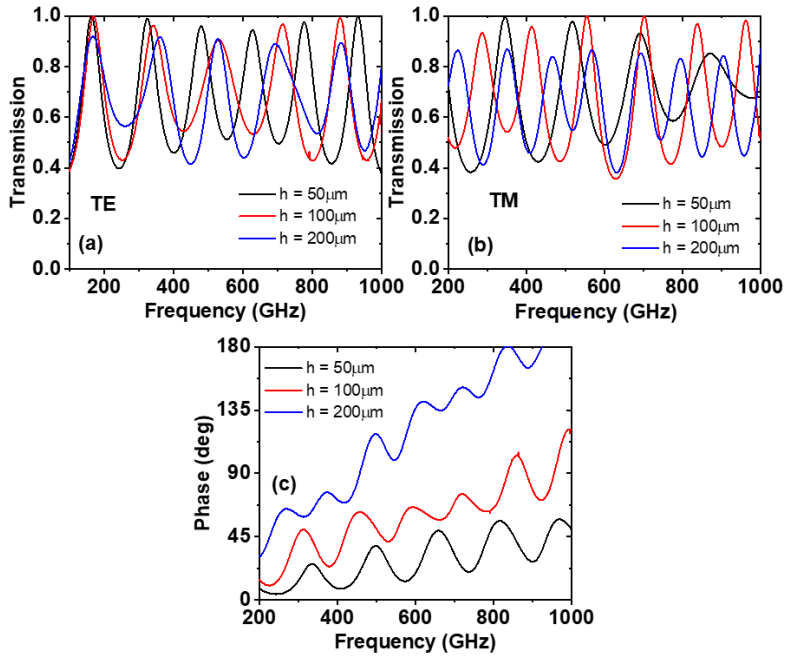


Figure 22: Transmission and phase retardation characteristics of a single-sided HCG-type waveplate modelled using FDTD simulations for three samples (a) along transverse electric (TE) polarization (b) along transverse magnetic (TM) polarization, and (c) phase difference between TE and TM.

From Fig. 22 now the sample with geometrical parameters $P = 100 \mu\text{m}$, $h = 200 \mu\text{m}$ $t = 250 \mu\text{m}$ was selected, as the phase difference between the two orthogonal polarizations were reaching 90 deg and 180 deg at 400 GHz and 900 GHz regions which was shown in blue curve. The results of transmission and phase retardation of a selected single-sided HCG-type waveplate for two orthogonal polarizations (TE and TM) are shown in Fig. 23. The transmission results for both the TE and TM polarizations were compared between the FDTD simulations, TDS and VNA measurements which shows a nice agreement in Fig. 23a, b.

The amplitude of such oscillations in transmission spectra for an un-patterned double-side polished Si wafer of 250 μm thickness is around 70 %, and for investigated structure in TE polarization it is around 50 %. The Fabry-Perot effect for TM polarization is suppressed quite significantly (amplitude modulation of 10% in TM versus 50 % in TE polarization) with the average transmission of silicon waveplate of about 70%. Fig. 23c shows the phase retardation between TE and TM polarizations across the investigated frequency range. Region where the phase retardation of 90 ± 10 degrees is achieved is marked by dashed lines. QWP operation is observed in the frequency range of 0.3 to 0.5 THz (bandwidth of 200 GHz). Inset shows the

comparison of phase retardation results of a HCG-type waveplate with and without inclination of grating side walls considered by FDTD simulations. It is seen that Fabry-Perot effect is suppressed more with the inclination of side walls by 11 degrees, moreover, the phase keeps close to constant value of $\pi/2$ in broad frequency range at around frequencies of 300 GHz to 500 GHz, respectively with bandwidth of 200 GHz.

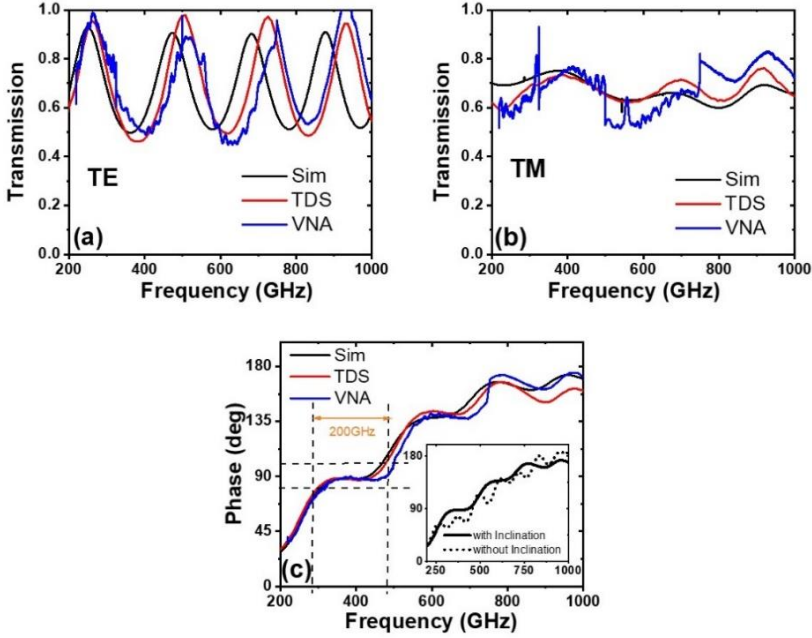


Figure 23: Transmission and phase retardation characteristics of a single-sided HCG-type waveplate compared between FDTD simulations (black), THz-TDs setup (red) and VNA setup (blue), (a) along TE polarization (b) along TM polarization, and (c) phase difference between TE and TM polarizations. Inset: comparison of phase retardation of a waveplate with and without inclination of side walls. Note that the breaks in transmission for VNA are caused by the changing of WR ranges.[46]

Design of flat profile double-sided HCG waveplate: To improve the transmission performance of a waveplate along the grating axis or TM polarization we have made a modification to the above mentioned single-sided HCG-type waveplate. We changed it to double-sided HCG-type waveplate possessing anti-reflection properties, simultaneously reducing reflections within the structure as well as coupling losses between the component and free-space. It consisted of a similar subwavelength periodic material-air interfaces with a period of $P_{MT} = P_{MB} = 100 \mu\text{m}$ on both top and bottom sides

of a HRFZ-Si wafer with an overall thickness of $t = 500 \mu\text{m}$ as shown in Fig. 24.

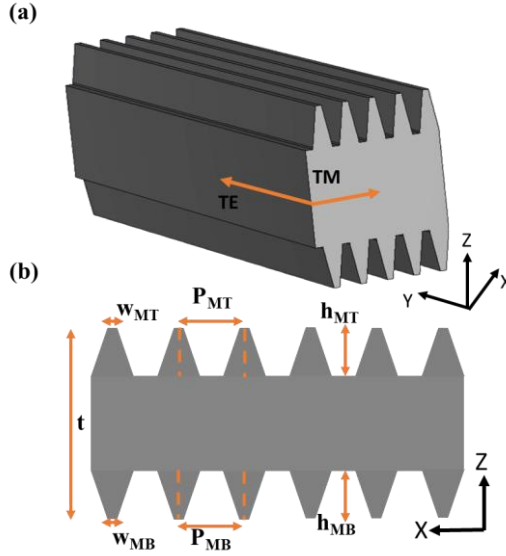


Figure 24: The Schematic representation of double-sided HCG-type waveplate; (a) 3D representation of a waveplate; (b) shows the 2-D representation of a waveplate along xz -plane with design parameters.

The height of meander gratings on each side of a waveplate is exactly half of an initial grating height of a single-sided sample with $h_{MT} = h_{MB} = 100 \mu\text{m}$ leaving a solid layer of silicon in middle with a thickness of approximately $300 \mu\text{m}$. The results of transmission and phase retardation of a selected double-sided monolayer HCG-type waveplate for two orthogonal polarizations (TE and TM) are shown in Fig. 25. In Fig. 25b we observe a transmission spectrum along grating axis of a modified waveplate featuring a double-side grating which shows a remarkable enhancement of transmission approaching nearly to 100 % for TM polarization. Additionally, in Fig. 25c it showcases a π phase shift between the two orthogonal polarizations which was not achieved in the previously mentioned single-sided waveplate. This enhanced transmission performance is observed within the frequency range of $0.434(0.369)$ THz to $0.979(0.860)$ THz with a broadband operational bandwidth of $545(491)$ GHz for the simulation(experimental) findings respectively. Conversely, we can achieve the required π phase shift between TE and TM polarizations, enabling the waveplate to function as a HWP in the frequency range of 0.778 THz to 0.978 THz, with an operational bandwidth spanning 200 GHz in simulations. However, it is important to note that in our experimental findings, achieving such π phase shift has proven challenging due to fabrication errors. We see in the experimental results that to achieve π phase shift as obtained in simulations additional refining of the DLA

technology for processing of double-sided samples is required. Simultaneously, at lower frequencies ranging from 0.327/0.300 THz to 0.403/0.382 THz, a $\pi/2$ phase shift is achieved with bandwidth of 76/82 GHz for simulations/experimental findings, offering a dual-band waveplate performance for a broadband spectrum of THz frequencies.

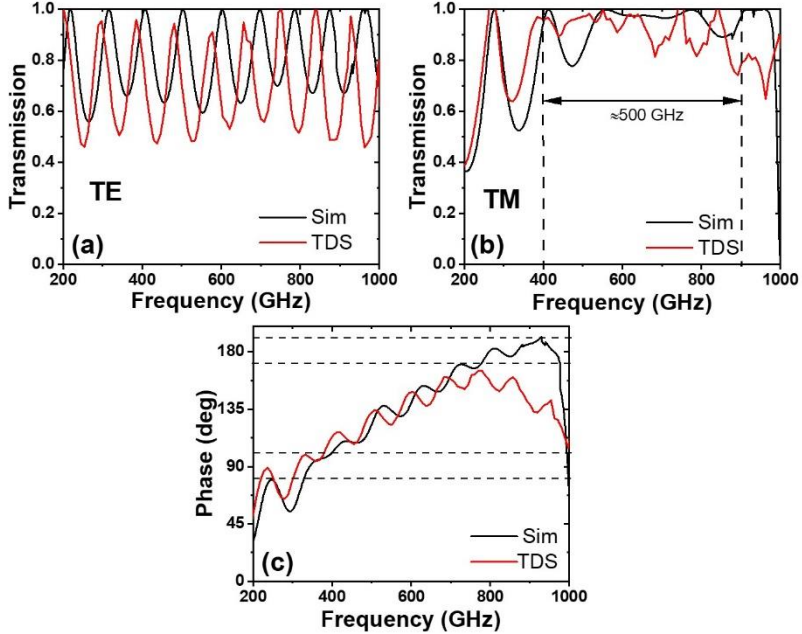


Figure 25: Characterization results of double-sided HCG-type waveplate compared with FDTD simulation (black) and THz-TDS setup (red): transmission spectra for (a) TE polarization and (b) TM polarization and (c) phase difference.[46]

Design of sinusoidal profile single-sided HCG-type waveplate: To mitigate the Fabry-Perot effect also along the TE polarization and with an aim to maintain smooth overall transmission of a waveplate across the frequency range we have introduced a surface modification along the TE-axis of the waveplate. In other words, to reduce the instability of transmission caused by the multiple Fabry-Perot peaks and dips, the flat shape of the grating was changed to a sinusoidal grating along the TE polarization as shown in Fig. 26a. In Fig. 26b the sinusoidal profile of a fabricated sample is shown in a color scale with ridges represented in red and grooves in blue colors.

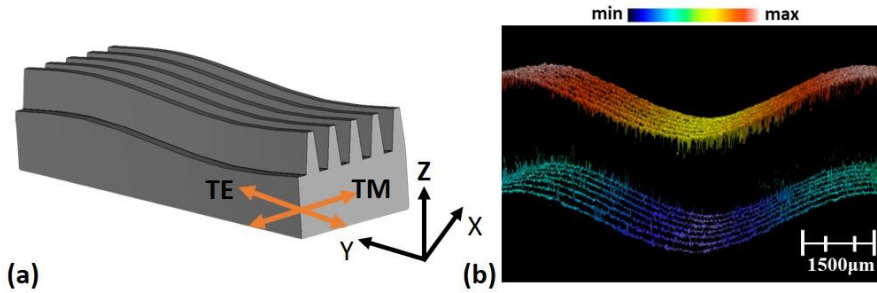


Figure 26: (a) 3D representation of a sinusoidal shape single-sided monolayer HCG-type waveplate (b) representing a sinusoidal grating profile shown in colour scale along YZ-axis with a sinusoidal modification along TE axis taken from the optical profilometer, showing grating ridges (red) and grating grooves (blue).[46]

The sinusoidal shape single-sided HCG-type waveplate consists of a similar subwavelength periodic material-air interfaces with a period of $P = 100 \mu\text{m}$ on top of a HRFZ-Si wafer with an overall thickness of $t = 250 \mu\text{m}$. The grating height of a waveplate was kept at $h = 100, 200 \mu\text{m}$ and the amplitude $a = 25 \mu\text{m}$ transitioning flat shape to sinusoidal shape with a sinusoidal period of $P_s = 1500 \mu\text{m}$ along TE polarization. The results of transmission spectra of a sinusoidal shape single-sided HCG-type waveplate compared with flat shape single-sided HCG-type waveplate for two orthogonal polarizations (TE and TM) are shown in Fig. 27. For both the spectra we clearly observe a reduction of Fabry-Perot effect along TE as well as TM polarization when compared to the flat design without any inclination of side walls.

The results of transmission of a selected sinusoidal shape single-sided HCG-type waveplate of $h=200 \mu\text{m}$ and $a=25 \mu\text{m}$ for two orthogonal polarizations (TE and TM) are shown in Fig. 28.

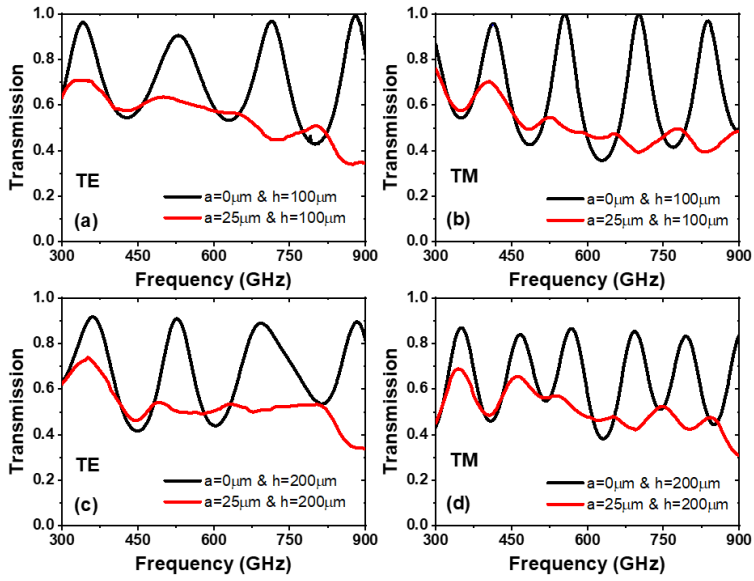


Figure 27: Shows the transmission spectra for TE and TM polarizations for samples (a&b) with $a = 0 \mu\text{m}$ & $25 \mu\text{m}$ with $h = 100 \mu\text{m}$; (c&d) with $a = 0 \mu\text{m}$ & $25 \mu\text{m}$ with $h = 200 \mu\text{m}$.

The transmission results for both the TE and TM polarizations were compared between the FDTD simulations, TDS measurements which shows a nice agreement in Fig. 28a, b. However, there is a significant decrease in transmission for both polarizations at higher frequencies. Given that the waveplate's intended function is in transmission mode, the observed low transmission is undesirable.

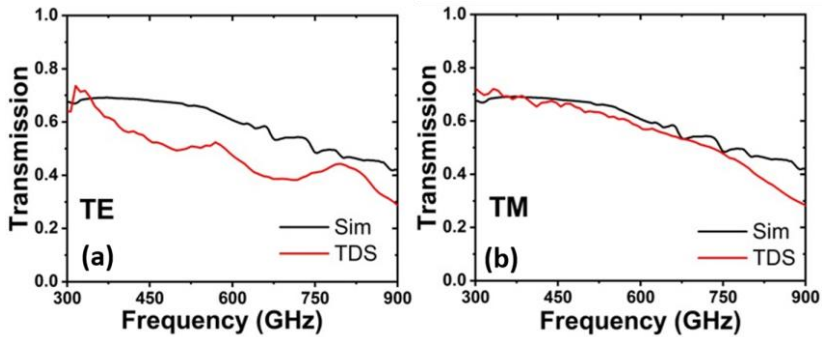


Figure 28: a) and b) transmission spectra of sinusoidal shape single-sided HCG-type waveplate for $a = 25 \mu\text{m}$ with $h = 200 \mu\text{m}$ with the FDTD simulation (black) and THz-TDS setup (red): for TE and TM polarizations respectively.[46]

Design of sinusoidal profile double-sided HCG-type waveplate: To improve the transmission performance of a waveplate at higher frequencies and narrow the transmission gap between TE and TM polarizations, we have implemented further adjustments to the sinusoidal shape single-sided HCG-type waveplate. This modification transforms the sinusoidal single-sided HCG-type waveplate to sinusoidal double-sided HCG-type waveplate, featuring a sinusoidal modulation on both top and bottom side of a HRFZ-Si with an amplitude of $a_{ST} = a_{SB} = 10 \mu\text{m}$ and a modulation period of $P_{ST} = P_{SB} = 1500 \mu\text{m}$, with an overall thickness of $t = 500 \mu\text{m}$, as depicted in Fig. 29.

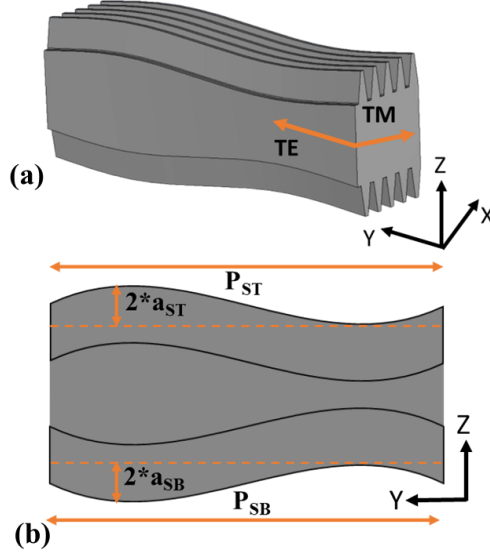


Figure 29: The Schematic representation of sinusoidal shape double-sided HCG-type waveplate; (a) 3D representation of a waveplate; (b) shows the 2-D representation of a waveplate along yz-plane with design parameters.[46]

As a result of these modification, the transmission of a waveplate improves significantly at higher frequencies. Simultaneously, the successful reduction of the transmission gap between TE and TM polarizations to less than 10% is achieved, all while ensuring that the overall Fabry-Perot effect remains diminished. Moreover, now the overall transmission of the waveplate exceeds 60% within the frequency range around 0.3 to 0.9 THz as it is shown in Fig. 30a, b. Furthermore, this modified waveplate still works as a QWP for a frequency of 0.300 to 0.391 THz offering an operational bandwidth of 91 GHz and operates as HWP for a frequency range of 0.713 to 0.924 THz providing an operational bandwidth of 211 GHz still showing dual-band waveplate performance for a broadband THz frequency range (see Fig. 30c).

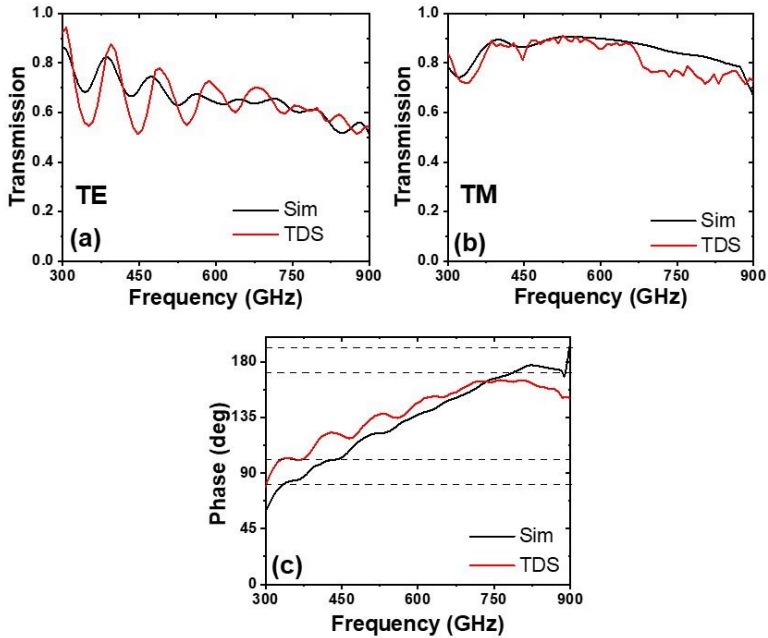


Figure 30: Transmission results of the sinusoidal double-sided HCG-type compared with FDTD simulation (black) and THz-TDS setup (red): transmission spectra for (a) TE polarization, (b) TM polarization and (c) phase difference.[46]

Polarization control with the QWP sample

Moreover, we conducted experimental research to demonstrate real application of the single-sided HCG-type waveplate with a commercial THz frequency domain system by utilizing Toptica Terascan 780 spectrometer setup. The results are shown in Fig. 31. To determine the sample's suitability as a QWP within a specified frequency bandwidth (0.3 to 0.5 THz), experiments were carried out at an intermediate frequency of 0.4 THz. Initially, we established a straightforward configuration in which linearly polarized light along the TE and TM axes was entirely blocked, but allowing circularly polarized light to be detected if QWP is inserted in between the elements at the angle of 45° . This setup comprised of a THz emitter emitting circular polarized THz radiation, a 0° polarizer converting circular to linear polarization (either vertical or horizontal), an analyzer oriented perpendicularly (90°) to the polarizer to block linearly polarized light, and a THz detector. Subsequently, the sample was introduced into the optical path at a 45-degree angle relative to both the polarizer and analyzer (blue color line in the inset of Fig. 31b). Remarkably, we observe increase of the signal transmission as detected by the THz detector in the spectrum range of 300-500 GHz, confirming that the designed sample performs as a QWP.

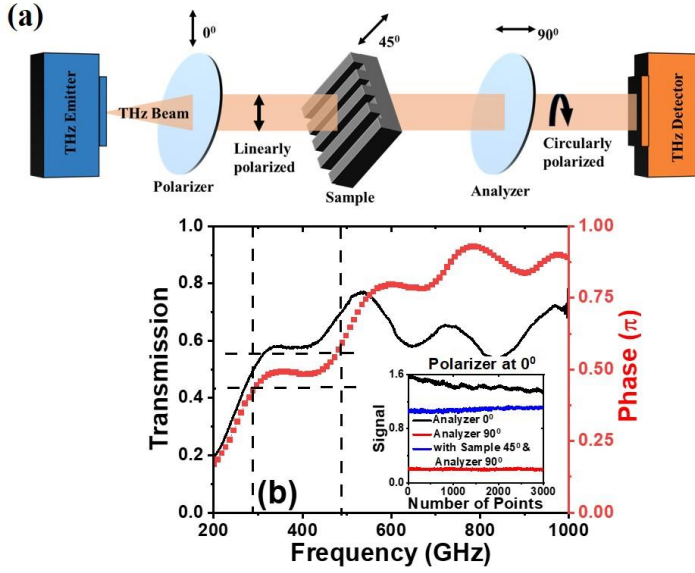


Figure 31: (a) Schematic representation of polarization measurement setup, (b) absolute transmission (left) of a waveplate measured exactly with the above shown setup configuration and the phase characteristics (right) of a waveplate normalized to π across the frequencies up to 1 THz. Inset: signal measurements in transmission mode at fixed 400 GHz frequency with both polarizer and analyser placed parallel (black curve); with both crossed (red curve) and with the sample placed in between and oriented at 45 degrees (blue curve).[46]

3.3. Free-standing meta-surfaces

In this section, we developed the free-standing meta-surface composed of different number of meta-atoms on a thin film.

First part, of this section is with free-standing metal-based meta-surface composed of different number of meta-atoms arranged as resonators array on a thin conductive film aiming to investigate the effect of mutual coupling between meta-atoms that leads to the broadening of overall resonance bandwidth. In this part, four meta-surface designs were considered by using single, 2×2 , 5×5 and 10×10 meta-atoms arranged in a square lattice array and framed in the metal film. The transmission performance of meta-surface samples was numerically investigated using FDTD simulations implemented in CST Studio software. The FDTD simulations were performed using a normal illumination of plane wave by choosing boundary conditions of a perfectly matched layer, used to absorb the transmitted and reflected waves from the structure. A default tetrahedral mesh type is used for the frequency

domain solver, setting up to an average of 10 mesh cells per wavelength with a unique feature in the software using adaptive mesh refinement. The S-parameter calculations were performed assuming the steady state energy criterion using a multi-frequency plane wave incoming onto the sample.

The DLA technique was used to fabricate designed samples, enabling precise control over the dimensions and spacing of metaatoms on a thin metal film. The samples were fabricated patterning the subwavelength structures with a focused laser beam, which removes an unwanted metal from the film, enabling the creation of precisely defined and well-shaped resonators. For this the femtosecond pulsed laser (Pharos, Light Conversion) was employed with an operation wavelength of 515 nm, 20 μm laser spot size diameter, pulse duration of 300 fs, 12 J/cm^2 laser irradiation fluence, scan speed of 1 mm/s (5000 pulses per mm), 7 scans. The meta-surface samples were characterized using a THz-TDS system and VNA system to measure resonant characteristics in transmission geometry. The multipole expansion analysis of the system is also performed to better understand nature of the resonance and its broadening behaviour.

Second part, of this section is with free-standing silicon-based meta-surface composed of similar shape of meta-atoms comprising concentric discs and rings but developed on a thin Si membrane with an electrical conductivity of 10 S/m targeting to achieve total transparency in a wide range of THz frequencies due to the suppression of electric dipole radiation in the far zone referred in literature as the “anapole” resonance. In this part, a meta-surface design was considered by using 10×10 meta-atoms arranged in a square lattice array. We show that coexistence of few anapole resonances enables broadband transparency of the free-standing meta-surface.

The meta-surface was fabricated from a 100 μm thick silicon wafer with ~ 10 Ohm-cm resistivity by sputtering a Cr layer, applying AR-P 6200 resist, and patterning it via electron beam lithography. By final cleaning and Cr removal, yielded a free-standing metaatoms with a total thickness of 60 μm . The transmittance and reflectance spectra of the fabricated meta-surface was by the THz-TDS system and compared with the FDTD simulations in the frequency range of 0.2-1.0 THz. The multipole expansion analysis of the system is also performed to better understand the suppression of the scattering in the far zone that led to broadband transparency.

Metal-based meta-surfaces

The samples of meta-atom arrays were developed on a thin metal film, to investigate the mutual coupling effects. A stainless-steel film with a subwavelength thickness of $50\ \mu\text{m}$ was selected for the development of the meta-surface samples varying number of meta-atoms in the array. The schematic representation of single meta-atom and an empty square aperture in a frame along with the experimental setup is shown in Fig. 32.

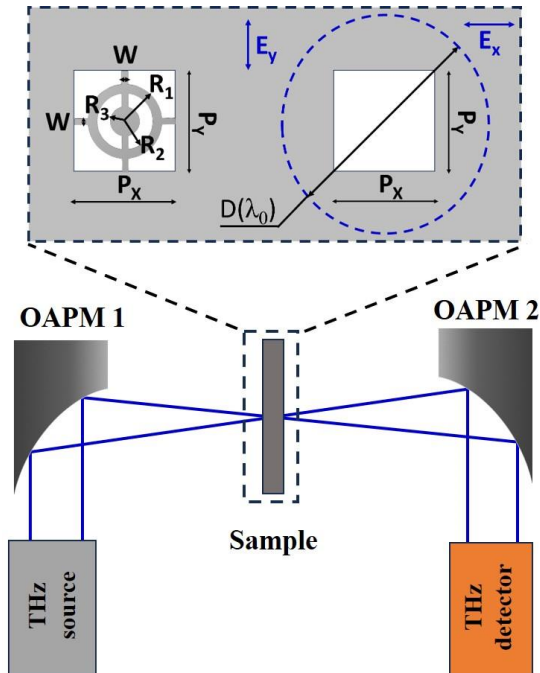


Figure 32: Schematic representation of experimental setup used to characterize the sample in THz-TDS and VNA systems. Inset shows the drawings of single meta-atom and empty square aperture in a metal frame with the THz radiation focused into diffraction limited beam size (blue-dashed line). It shows also orientation of the electric field vector in the incident beam with respect to the intra- and inter-meta-atom bridges.[90]

There were designed and arranged periodically subwavelength resonators embedded in a metal frame in a format of single, 2×2 , 5×5 , and 10×10 meta-atoms, to investigate the collective response of the system. Microscope images of fabricated samples with different number of meta-atoms arranged periodically are shown in Fig. 33.

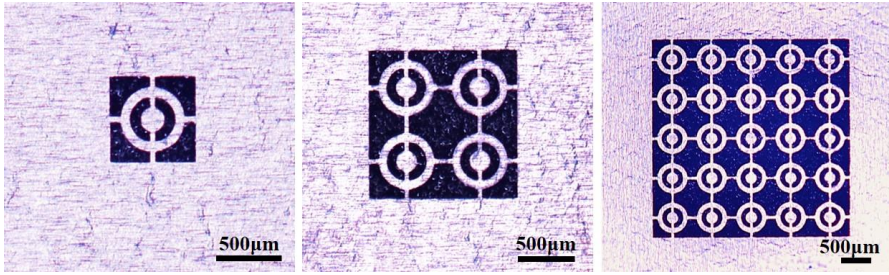


Figure 33: Microscope image of fabricated samples with 1x1, 2x2 and 5x5 array of meta-atoms in a frame of stainless-steel film.[90]

Subwavelength Size Aperture: the transmission characteristics of a empty square aperture on stainless-steel film with a subwavelength thickness of $50\ \mu\text{m}$ while the length of each side along x and y directions with P_x and P_y , being the value of $650\ \mu\text{m}$ was investigated initially. The transmission results are shown in Fig. 34. The transmission results compared between the FDTD simulations, TDS measurements and VNA which shows a nice agreement. The overall transmission of this subwavelength aperture was $< 10\%$ for the frequency of interest $0.35\ \text{THz}$.

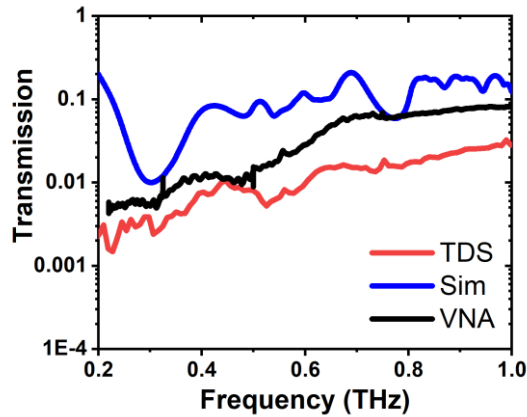


Figure 34: The Transmission characteristics of a square aperture with the length of each side along x and y directions of $650\ \mu\text{m}$; FDTD simulations (Blue), THz-TDS (Red) and VNA (black).

The transmission of the device was defined as the squared ratio between the field amplitude of sample and the field amplitude without sample. The diameter (D) of the THz beam incident on the sample via off-axis parabolic mirror (OAPM) was measured in the experimental setup based on VNA, demonstrating value of about $4.73\ \text{mm}$ at $0.35\ \text{THz}$. Beam size was almost

order of magnitude larger than size of the empty square aperture as it is shown schematically in Fig. 32.

Single Meta-atom Embedded in a Metal Frame

The design of a single meta atom with a disk in ring composition has been inspired from [67]. The dimensions of a single meta-atom were adjusted to THz spectrum range setting values for a radius of circular rings $R1$, $R2$ and $R3$ with 250, 170 and 96 μm , respectively. The bar width, W , used to bound disk and ring in the meta-atom, was of about 42 μm , while the lattice period along x and y directions were fixed with P_x and P_y , being of the same value of 650 μm .

The meta-atom structure on metal film was designed to demonstrate a sharp resonance at the frequency of 0.35 THz or wavelength (λ_0) of 0.856 mm, value of which is almost at a wavelength 1.32 times of its lattice period dimension. The results of transmission and scattering power for multipoles of a single meta-atom for case of E_x and E_y polarization are shown in Fig. 35. The resonance peak in the transmission spectrum was experimentally observed (Fig. 35a) demonstrating the q -factor of about 8.5.

Figure 35b shows the multipoles analysis of electric and magnetic moments where we see a clear dominance of electric dipole compared to other multipole moments over a frequency range of interest. The transmission peak observed at 0.35 THz for E_x polarization was attributed to the pronounced presence of a strong p and a comparatively weak M . In contrast, the E_y polarization spectrum exhibits a transmission dip characterized with a slight dip in the P at the resonance frequency (see Fig. 35c).

The field distributions for single meta-atom give us a better understanding on the resonance behaviour. The results are shown in the inset of Fig. 35b&d. The localized E -field is concentrated on the ring structure and on the intra-bridges of the meta-atom, generating a p moment, which indicates the presence of a resonance peak (see case $|E|$). While, $|H|$ field plot illustrates a confined H -field at the edges of the inter-bridges of the meta-atom, coupling to the metal frame, which indicates the presence of both M and Q_m moments which are not negligible require proper assessments. In summary, the optical characteristics and the resonance of single meta-atom in the selected THz range mainly depends on the p moment.

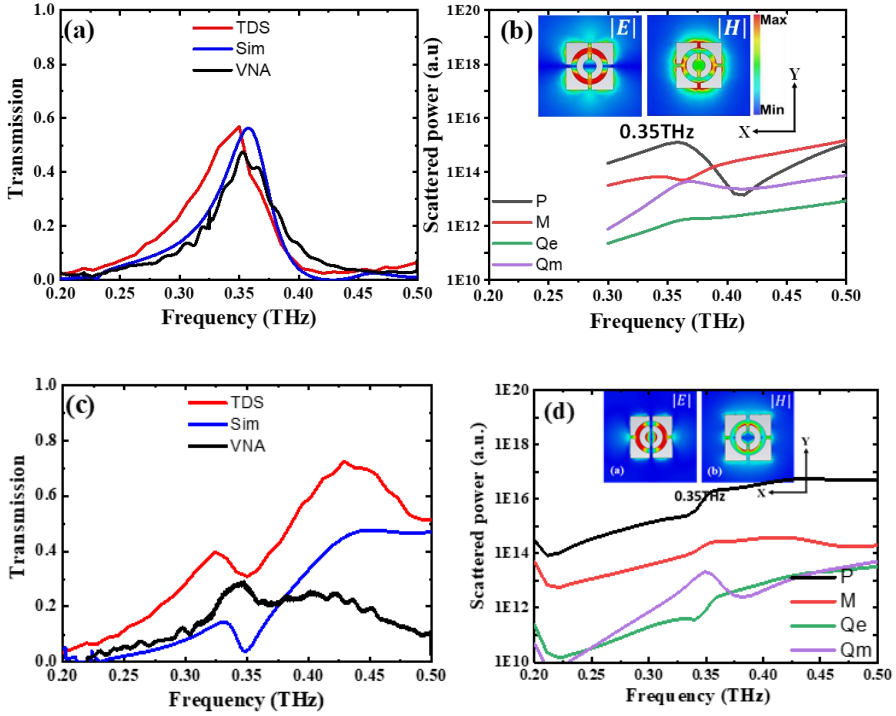


Figure 35: Transmission characteristics of a single meta-atom compared between FDTD simulations (blue), THz-TDs setup (red) and VNA setup (black), respectively shown for (a) E_x polarization and (c) E_y polarization, Four leading scattered powers of multipole decomposition for the single meta-atom, where p , M , Q_e , and Q_m are electric dipole, magnetic dipole, electric quadrupole, and magnetic quadrupole respectively shown for (b) E_x polarization and (d) E_y polarization. Insets demonstrate an E and H fields in XY plane of a single meta-atom in a metal frame at the resonance frequency of 0.35 THz.[90]

We also investigated the surface currents (j). The results are shown in Fig. 36. One can see a currents presence along the inter-bridges of meta-atoms. The surface current on inter-bridges that are induced by the x -polarized incidence generates a magnetic field with a strong M as well as a high oscillating Q_m surrounding the inter-bridges along z -axis.

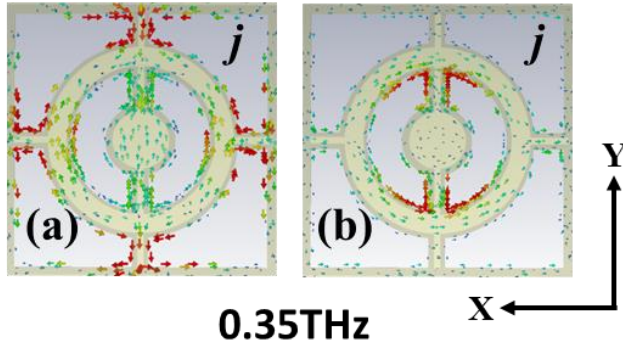


Figure 36: Distribution of surface currents (j) in xy -plane of a single meta-atom in a metal frame at the resonance frequency of 0.35 THz for (a) E_x polarization and (b) E_y polarization.

2x2 array Meta-atoms Embedded in a Metal Frame

The results of transmission and scattering power for multipoles of a 2×2 array meta-atoms are shown in Fig. 37. Interestingly, we clearly see the resonance broadening in transmission spectrum at around 0.35 THz compared to the performance of metamaterial based on a single meta-atom. The increase in bandwidth was attributed to the mutual coupling between the meta-atoms arranged into 2×2 array. This is a result of small p moment which shape is also different from that of single meta-atom. Moreover, the M and Q_m moments dominate over p moment as it is seen from the results shown in Fig. 37b. For better understanding of broadening of resonance bandwidth and the reason of magnetic multipoles dominance over electric dipole can be understood from the field plots. These were found at the resonance frequency and the results are shown in inset of Fig. 37b. We see that E -field is localized, similar to the single meta-atom case, on the ring structure of all the four meta-atoms providing a p moment that contributes to the resonance and a negligible E -field on the intra-bridges of the resonator that leads to split in resonance. Whereas, a strong coupling of H -fields on the inter-bridges between the meta-atoms leading to a broadening of resonance along E_x polarization. The transmission and scattering power for multipoles results of excitation with E_y polarization for 2×2 array are shown in Fig. 37c, d. We observe much more pronounced resonance dip at 0.35 THz compared to single meta-atom in the transmission spectrum for Simulation, THz-TDS measurements and VNA measurements. From the Fig. 37d the multipoles analysis of electric and magnetic moments where we can understand the resonance dip in the transmission is clearly due to the dip present in p at 0.35THz.

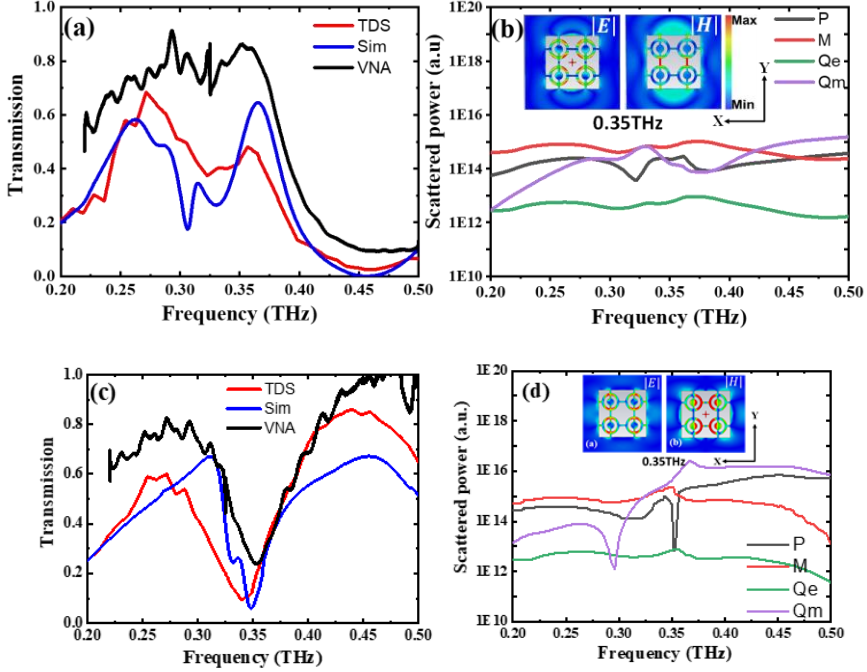


Figure 37: Transmission characteristics of a 2×2 array compared between FDTD simulations (blue), THz-TDs setup (red) and VNA setup (black), respectively shown for (a) E_x polarization and (c) E_y polarization, Four leading scattered powers of multipole decomposition for 2×2 array, where p , M , Q_e , and Q_m are electric dipole, magnetic dipole, electric quadrupole, and magnetic quadrupole respectively shown for (b) E_x polarization and (d) E_y polarization. Insets demonstrate an E and H fields in XY plane of a 2×2 array meta-atoms in a metal frame at the resonance frequency of 0.35 THz.[90]

Furthermore, we found a presence of surface currents along the inter-bridges of meta-atoms for 2×2 array similar to single meta-atom. The surface current on inter-bridges that are induced by the x -polarized incidence generates a magnetic field, induced magnetic field patterns produce a strong M as well as a oscillating Q_m surrounding the inter-bridges along z -axis led to increase in resonance bandwidth, shown in Fig. 38.

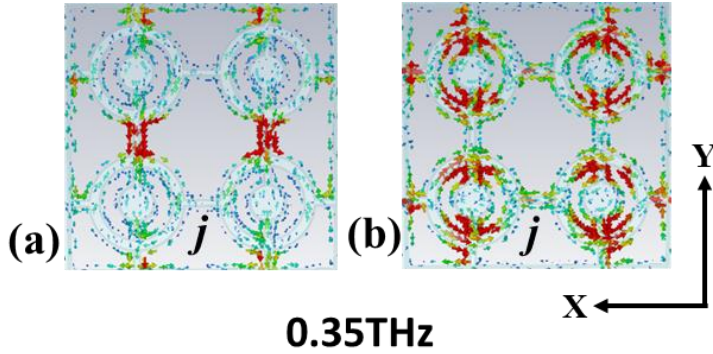


Figure 38: Demonstrate an surface currents (j) in XY plane of a 2x2 array in a metal frame at the resonance frequency of 0.35 THz (a) E_x polarization and (b) E_y polarization.

Modelling of different width size of metal film surrounding the meta-atoms:

To study the effect of metal frame on to the broadening of resonance bandwidth of a meta-surface, we consider the width of a metal frame surrounding the 2x2 array kept at two different sizes of 200 μm and 1000 μm . The transmission results for both the E_x and E_y polarizations were performed by FDTD simulations. Figure. 39 shows the results. There is no difference in the resonance bandwidth or the resonance frequency of meta-surface irrespective to the width of surrounding metal frame by maintaining resonance peak at 0.35 THz. Those the size of metal frame surrounding the meta-atoms doesn't affect the resonance bandwidth of overall meta-surface.

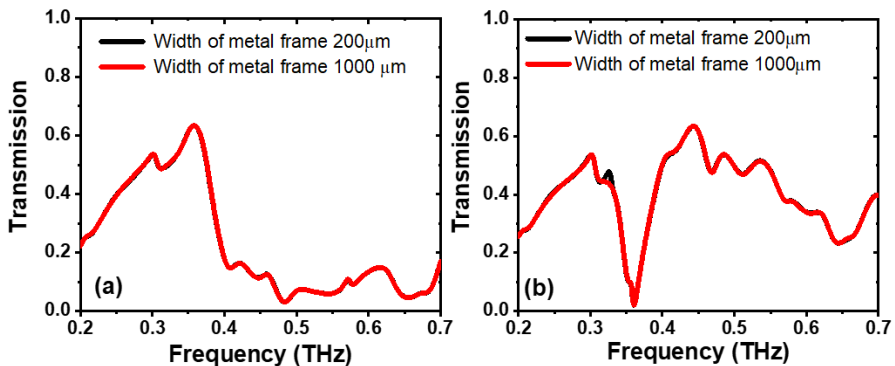


Figure 39: Transmission characteristics of a 2x2 array meta surface FDTD simulations with a change in surrounded metal frame size with 200 and 1000 μm (a) E_x polarization, (b) E_y polarization.

Influence of Inclination of Walls: Further, we have investigated effect of inclination of walls of meta-atoms on the resonance bandwidth of 2×2 array. The reason to do such investigation is because the meta-surfaces which were fabricated by a DLA techniques using femtosecond pulsed laser was focused on to the substrate for patterning the material. While patterning, the laser is focused on to the substrate with certain angle causing an unsymmetric/inclination on the walls of meta-atoms along propagation direction. The measured inclination on walls of meta-atoms is approx. 11 degrees. The transmission results for 2×2 array with inclination and without inclination of walls of meta-atoms for both the E_x and E_y polarizations were performed by FDTD simulations. Figure. 40 shows the results. There is no difference in the resonance bandwidth or a shift in the resonance frequency of meta-surface irrespective to the inclination of walls caused by the fabrication.

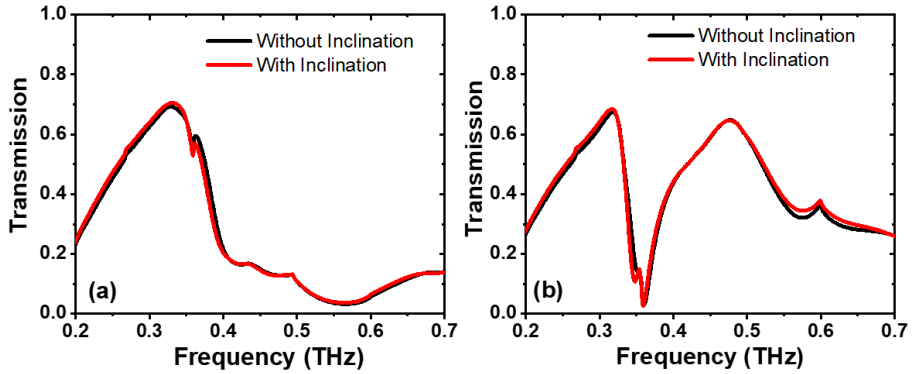


Figure 40: Transmission characteristics of a 2×2 array meta surface FDTD simulations with a influence wall inclination at angle of 11 deg (a) E_x polarization, (b) E_y polarization.

5×5 meta-atoms in a frame and infinite size array: Figure. 41 shows the results of transmission and scattering power for multipoles obtained for E_x and E_y polarization excitation of the meta-atoms arranged in 5×5 array as well as for infinite array. Here we still see the broadening of resonance bandwidth. The results of multipole analysis demonstrate a clear dominance of p moment among all the multipoles which resemble similar pattern to the transmission spectrum of the metamaterial. This shows us another strong support reason that shape of the resonance completely depends on p moment for a resonator and a coupling of H -fields on the inter-bridges between the meta-atoms led to a broadening of resonance. The transmission spectrum modelled for infinitely large number of meta-atoms with unit cell approximation in the simulation model was found to be similar to that of the metamaterial sample composed

of significantly larger 10x10 array of the meta-atoms arranged periodically in a thin metal frame, data of which are also shown in Fig. 41a&c by dashed blue line and dashed red line, respectively. It is worth to note that the 10x10 array sample demonstrated the resonance characteristic in terms of spectrum shape, resonance peak magnitude and bandwidth to be like that of the 5x5 array sample. Thus, we can assume that 5x5 array has the critical number of meta-atoms to perform as infinite size 2D metamaterial.

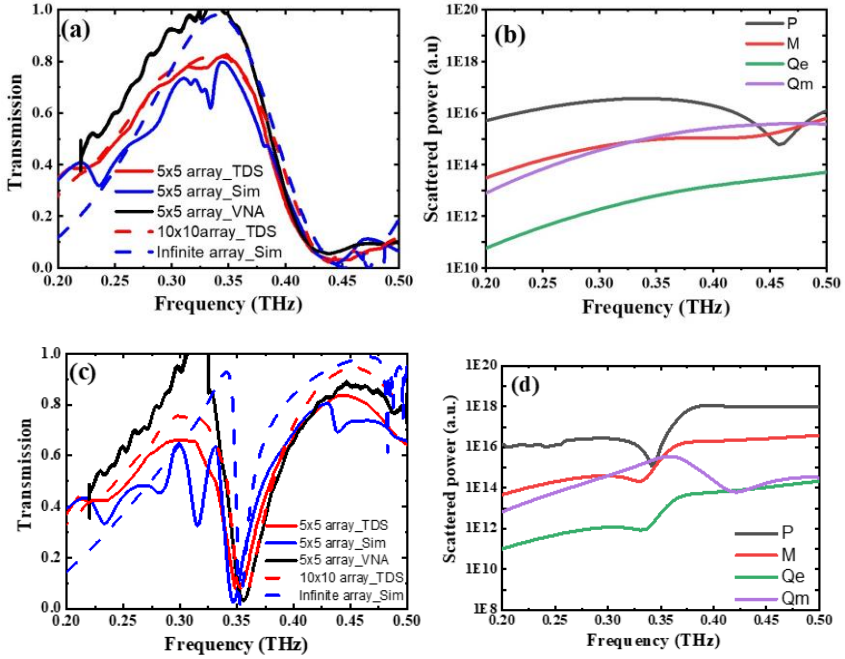


Figure 41: Transmission characteristics of a 5x5 array compared between FDTD simulations (blue), THz-TDs setup (red) and VNA setup (black), Infinitely large with unicc cell approximation FDTD simulations (dashed blue) and a dashed red for 10x10array array measured with THz-TDS setup (a) E_x polarization and (c) E_y polarization; Four leading scattered powers of multipole decomposition for the 5x5 array, where p , M , Q_e , and Q_m are electric dipole, magnetic dipole, electric quadrupole, and magnetic quadrupole, respectively shown for (b) E_x polarization and (d) E_y polarization.[90]

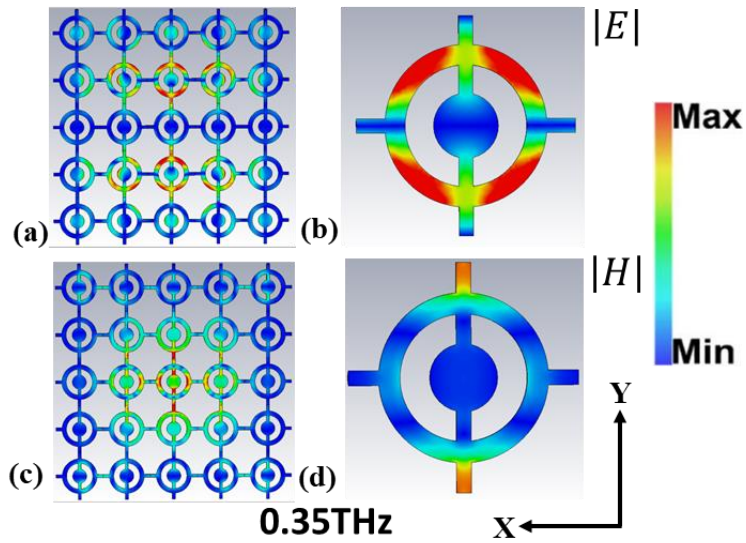


Figure 42: (a&b) E-field in the xy plane; (c&d) H-field in the xy plane, at the resonance frequency of 0.35 THz for the 5x5 array and infinite size array (unit cell) meta surfaces shown for E_x polarization.[90]

Figure. 42 shows a field plots for 5x5 array and for unit cell of infinite size array of the meta-atoms. We see a similar trend with the confined E -field on the ring structure for case of E_x polarization and a negligible field on the intra-bridges for case of E_x polarization leading to the resonance peak and dip. On the other hand, confined strong H -fields at the edges of the inter-bridges of the meta-atoms result in broadening of resonance bandwidth for E_x polarization.

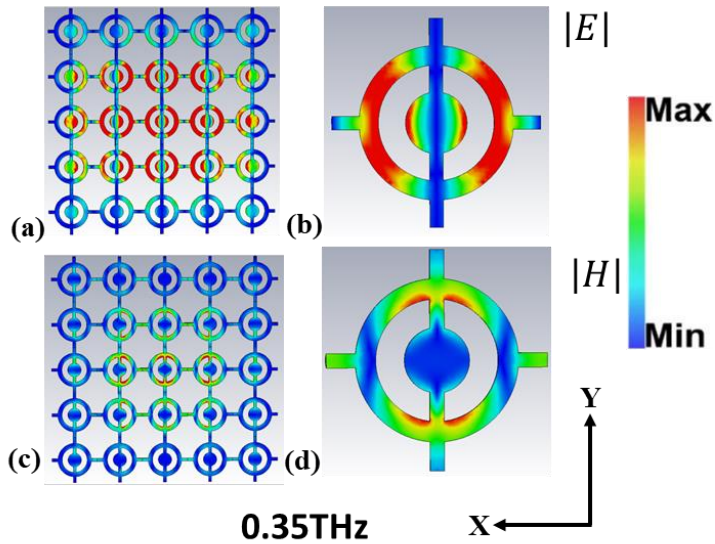


Figure 43: Similar as in Fig. 39 but for case of E_y polarization.[90]

In Fig. 43. we show a field plots for 5x5 array and infinite array (unitcell) which show a similar trend to that of 2x2 array with the confined E -field on the ring structure and negligible field on the intra-bridges for E_y polarization leading to resonance dip. On the other hand, Fig. 43d shows the existence of H -fields confining to the inner side of a meta-atoms.

More detailed analysis of the resonance observed in the experimental spectra was performed. The results are shown in Fig. 44. The resonance bandwidth (Δf), obtained at fullwidth of half maxima (FWHM), the resonance peak frequency (f_0), and the quality factor ($Q=f_0/\Delta f$) for all four discussed metamaterial samples are summarized in Table. 7 We clearly see the reduction in q -factor values from 8.5 to 2.1 comparing to single meta-atom and 10x10 meta-atoms in the metamaterial.

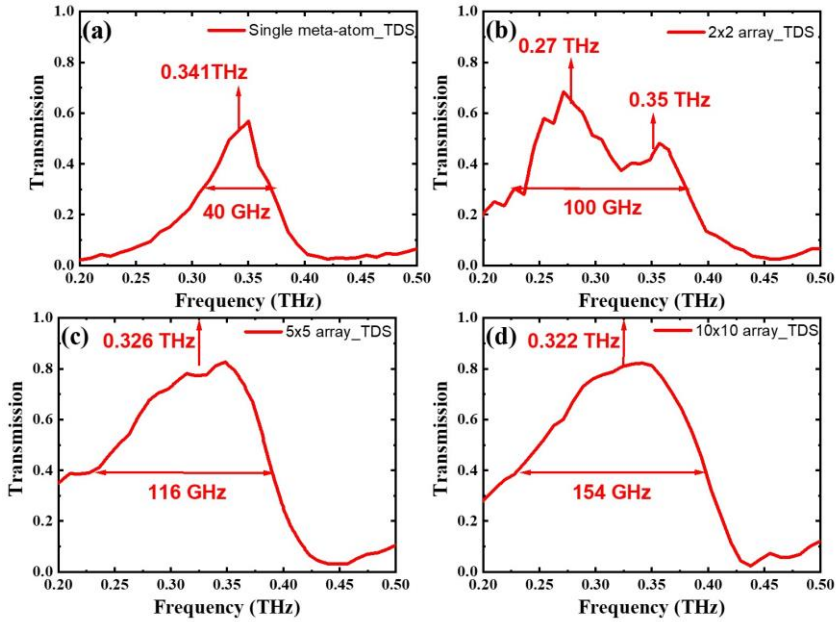


Figure 44: Measured transmission characteristics of the metamaterial samples for case of E_x polarization (a) single meta-atom, (b) 2x2 array, (c) 5x5 array and (d) 10x10 array. Parameters obtained after Gaussian fitting to experimental results are also indicated.[90]

Table 7: The resonant peak characteristics, *i.e.* spectrum position f_0 , bandwidth Δf , and q -factor, for the metamaterial samples composed of different number of meta-atoms sensing in the experiment with E_x polarization.[90]

Number of meta-atoms	Bandwidth (Δf)	Peak frequency (f_0)	q -factor ($f_0/\Delta f$)
1 (Single)	40 GHz	0.34 THz	8.5
4 (2x2 array)	100 GHz	0.35 THz	3.5
25 (5x5 array)	116 GHz	0.33 THz	2.8
100 (10x10 array)	154 GHz	0.32 THz	2.1

Silicon-based meta-surfaces

Figures. 45 show transmittance and reflectance spectra, respectively, of the fabricated meta-surface in the frequency range of 0.4-0.8 THz at normal incidence for the electric field polarized along x - and y -axes. The solid lines present the simulated spectra, while the circles show the experimental data. The THz permittivity of the silicon wafers used in our experiment was measured in the spectral range 0.1-3.5 THz in [91]. The simulated and measured transmittances see Fig. 45a are as high as 70%.and are almost frequency-independent between 0.5 THz and 0.7 THz. Since the observed variation of the transmittance in the transparency window does not exceed 30%, the anisotropy induced by intra-metaatom bridges is relatively low. Figure 45b shows that in the transparency window, calculated and measured reflectance values do not exceed 20%. The numerical simulation predicts a pronounced dip in the reflectance spectrum for both polarizations at the frequency of 0.55 THz, which, however, was not well reproduced in the experiment.

To gain qualitative understanding of the origin of the transparency window, we evaluate the contributions of individual multipoles to the scattered radiation and consider the frequency dependence of the radiation power scattered by the metaatom. Figure. 46 shows power spectra of the radiation scattered by the electric and magnetic dipoles, electric and magnetic quadrupoles, and toroidal moment, which are introduced in Eq. 5. Since toroidal and electric dipole moments produce identical radiation patterns in the far zone, we also calculated power generated by the combined source $\mathbf{TED} = \mathbf{p} + \frac{i\omega}{c^2}\mathbf{T}$. It is worth noting that interference between p and T may either be constructive or destructive. The latter corresponds to the anapole resonance, which manifests itself as a dip in the TED emission spectrum.

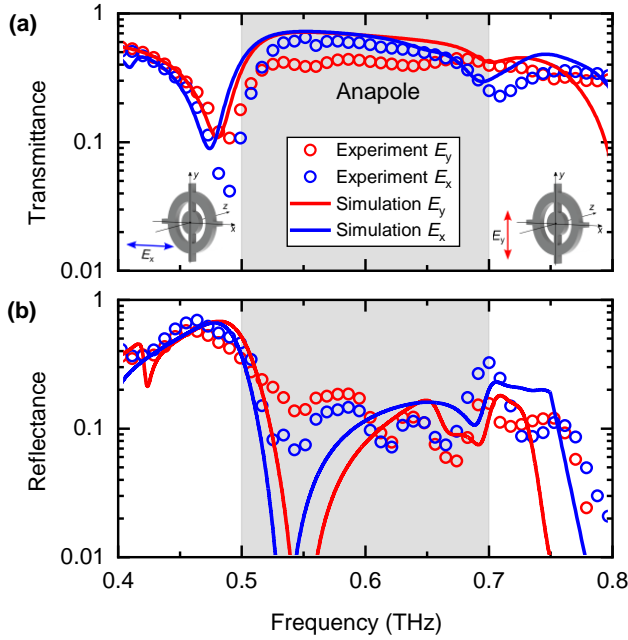


Figure 45: Simulated (solid lines) and measured (circles) transmittance (a) and reflectance (b) spectra of the meta-surface in the spectral range of 0.4 – 0.8 THz for incident wave polarized along x - and y -axis (blue red and lines, respectively) at normal incidence. Insets illustrate the orientation of the electric field vector of the incident wave with respect to the intra- and inter-metaatom bridges.[78]

One can observe from Fig. 46 that there exist two anapole resonances situated at the frequencies of 0.52 THz and 0.625 THz, where a suppression of the scattering and, correspondingly, an increase of the transmittance is expected. In addition, in the frequency range of 0.54 – 0.56 THz, the powers produced by all multipole moments but magnetic dipole are minima, *i.e.* this frequency range corresponds to the compound anapole resonance. The coexistence of two anapole resonances and a compound anapole resonance in a relatively narrow spectrum region essentially suppresses the scattering of the metaatoms that results in the transparency window spanning from 0.5 THz to 0.7 THz. Figure. 46 show that the magnetic dipole dominates in scattering in this frequency range. Our numerical simulation showed that silicon conductivity is responsible for about 30 % reduction of the transmittance within the transparency window. Although the bridges do not influence the primary multipoles or the overall response of the metamaterial, the magnetic quadrupole is significantly affected under E_x polarization. This effect becomes more pronounced at higher frequencies. The bridges, indeed, introduce

asymmetry, leading to the emergence of higher-order multipoles in the metamaterial's response. Specifically, the magnetic quadrupole represents a "trapped mode"[92] under E_x polarization. However, this trapped mode experiences leakage under E_y polarization as the magnetic field penetrates the inner bridges, becoming more concentrated compared to E_x polarization. Consequently, the magnetic quadrupole exhibits a higher intensity. It is worth noting that this mode emerges only under small perturbations [93]. At higher frequencies, a resonant manifestation of the trapped mode is anticipated.

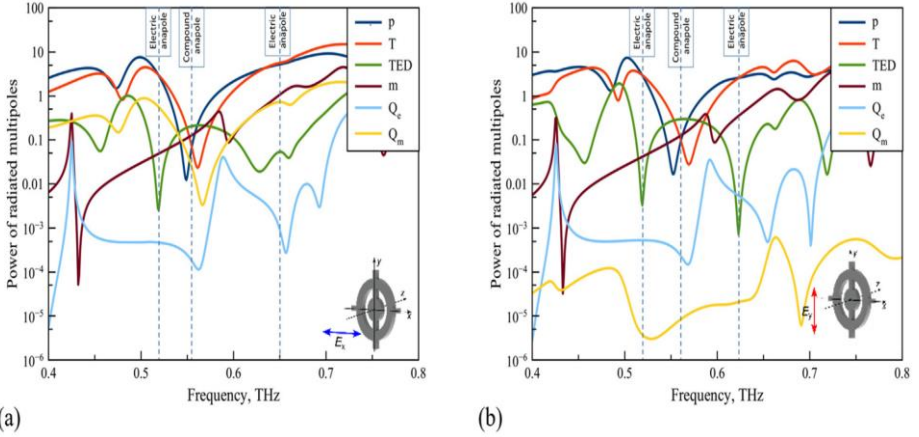


Figure 46: Radiation power spectra of electric dipole moment p (blue), toroidal dipole moment T (orange), magnetic dipole moment M (violet), electric quadrupole Q_e (cyan), magnetic quadrupole moment Q_m (yellow), and combined electric/toroidal moment $TED = \mathbf{p} + \frac{ik}{c}\mathbf{T}$ (green).

Dips in the TED spectra at 0.52 THz and 0.625THz represent the electric anapole resonances, while the compound anapole resonance is situated in the frequency range 0.54-0.56 THz where all-multipole moments but magnetic dipole are strongly suppressed.[78]

To study the effect of the anapole and compound resonances on the reflectance further, we compared the reflectance spectra of a gold mirror with and without our meta-surface. Results are shown in Fig. 47a. One can see that placing the meta-surface on top of the gold mirror leaves reflectance in the transparency window virtually unchanged for x - and y -polarized incident light, *i.e.* the presence of the meta-surface is hardly noticeable. On the contrary, outside the transparency window, the meta-surface strongly suppresses the THz wave reflected from the mirror. Figure 47b demonstrates

that the reflectance spectrum of empty aperture remained order of magnitude below than that of meta-surface in all experiments.

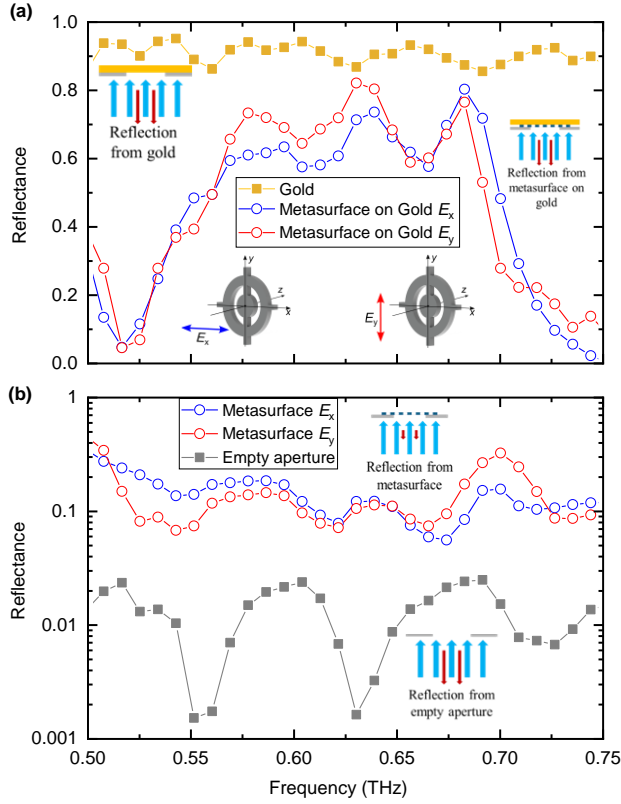


Figure 47: (a) THz reflectance spectra at normal incidence of the meta-surface combined with the gold mirror for the E_x - (blue line) and E_y - (red line) polarized light and the bare gold mirror after aperture (gold line). The results are presented in a linear scale. (b) THz reflectance spectra of a bare meta-surface at normal incidence for the E_x - (blue line) and E_y - (red line) polarized THz radiation. The black line shows the reflectance of the empty aperture used in experiments. Insets illustrate experimental arrangements.[78]

Finally, we investigated the dependence of the THz transmittance on the angle of incidence for different polarizations of the incident wave. The results are shown in Fig. 48. One can observe that within the transparency window of 0.5-0.7 THz, the transmittance may become as low as 10% when the meta-surface is rotated up to 45 degrees around both x - and y -axes for both polarizations of the incident wave. Importantly, however, the dependence of the transmittance on the polarization and rotation axis shows a pronounced frequency dependence. Specifically, the obtained weak dependence of the transmittance on the angle of incidence in the red part of the transparency

window may indicate that anapole resonance at 0.52 THz dominate the meta-surface response. On other hand, in the vicinity of the compound anapole resonance at 0.55 THz and anapole resonance at 0.625 THz we observe pronounced transmission dependences on the incident angle. This may be caused by the mutual coupling effects between inter-metaatom bridge, disk, and ring at these frequencies that require further investigation. It is worth noting that altering the angle of incidence and/or polarization of the incoming light may drastically change the electromagnetic field in the near zone, however, this hardly affects the suppression of the field in the far zone at the anapole resonance.

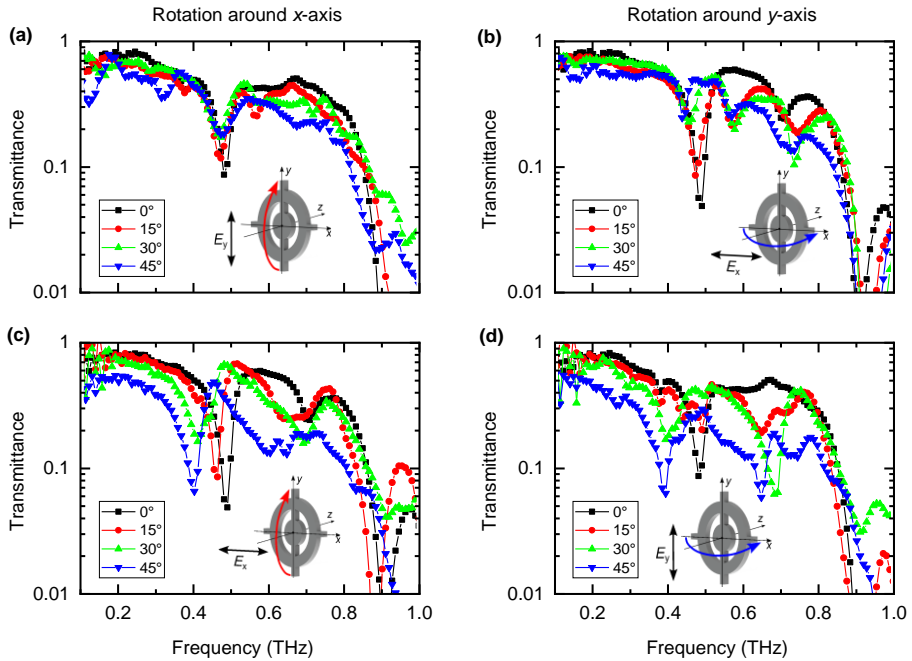


Figure 48: The transmittance spectra measured when the meta-surface was rotated around x -axis (a,c) and y -axis (b,d) for the incident wave polarized along (a,d) and perpendicular (b,c) intra-metaatom bridges.[78]

CONCLUSIONS

We have developed successfully metal- and semiconductor-based diffractive optical elements, including hybrid MPZP lenses, high-contrast grating waveplates, and free-standing meta-surfaces for THz frequency applications. The key findings and conclusions are:

- 1) Hybrid MPZP lenses made of silicon offer scalability, with improved focusing gain through a $\pi/4$ phase shift, such improvement attributes in reduction of shadowing effects at outer subzones.
- 2) The fabrication process, utilizing large-diameter laser beams, enables efficient large-scale production of the hybrid MPZP lenses, making them a promising solution for high-frequency applications.
- 3) The monolayer silicon-based high-contrast grating waveplate demonstrated efficient quarter-wave operation in the frequency range of 0.3 to 0.5 THz providing operational bandwidth of 200 GHz.
- 4) The inclination of grating walls along with the integration of an orthogonally oriented sinusoidal grating effectively suppressed the Fabry-Pérot effect and ensured efficient operation of silicon-based high-contrast grating as broadband THz waveplate.
- 5) The arrangement of meta-atoms at subwavelength distances induces strong mutual coupling, which significantly modifies resonance behavior of meta-surface composed of meta-atoms.
- 6) This coupling effect enhances the resonance bandwidth, increasing it from 40 GHz to 154 GHz, while also reducing the q -factor nearly four-fold with the change of meta-atom amount from 1x1 to 10x10.
- 7) Multipole decomposition and field analysis confirm that strong magnetic field interactions drive these changes. These findings offer valuable design strategies for tailoring metamaterial properties, enabling optimized performance in applications such as sensors, filters, and absorbers.
- 8) We develop a silicon-based meta-surface consisting of concentric disks and rings arranged in a square lattice that demonstrate the coexistence of the compound anapole and anapole resonances which enables broadband transparency. It effectively suppresses radiated scattering in the 0.5–0.7 THz range and performance remains robust across varying angles of incidence and polarizations.

SANTRAUKA

Įvadas

Optika, pagrįsta difrakciniais optiniais elementais (DOE), pasižyminti mažu storiu ir svoriu bei minimaliais sugerties nuostoliais, pradėta kurti daugiau nei prieš pusę amžiaus [1]. Skirtingai nei įprasta optika, DOE optika remiasi bangų difrakcijos ir interferencijos savybėmis, kurių dėka gali būti valdoma šviesa, pasitelkiant mažus lyginant su bangos ilgiu optinius elementus, kurie tam tikru būdu keičia fazę atskiruose erdvės segmentuose, kai banga praeina per DOE.

Pastaraisiais metais terahercų (THz) technologijos plėtrai didelę įtaką padarė THz pluošto formavimo būdai [2][3], spektroskopinis THz vaizdinimas [4] ir naujų ryšio sistemų poreikis [5]. Taigi, tikslų ir specializuotų optinių elementų dizainai naudojantys difrakciją, išlieka itin svarbus. Galimybė tūrinius elementus pakeisti plonomis struktūromis yra vis dažniau pageidaujama GHz ir THz dažnių diapazonuose.

DOE optika THz dažnių ruožui siūlo kompaktiškus ir lengvus komponentus, kurie gali būti alternatyva tradicinei optikai. Tarp plačiausiai paplitusių DOE yra difrakcinės gardelės, bangų plokštelės, daugiapakopių fazinių zoninių plokštelių (MPZP) lęšiai ir metamedžiagos. DOE ypač patrauklūs pluoštelio formavimo taikymuose THz srityje ne tik dėl savo kompaktiškumo ir mažo svorio, taipogi dėl suderinamumo su integrinių lustų technologijomis palyginti su tradiciniais šviesą atspindinčiais ir laužiančiais optikos elementais [2],[6]. Priklausomai nuo funkcijos, tokios kaip pluoštelio fokusavimas, nukreipimas ar dalinimas, DOE gali įgauti įvairias struktūrines formas, pagrįstas banginės optikos nulemtomis taisyklėmis [7]. Dėl šių ypatumų DOE yra itin susidomėjusi THz tyrimus atliekanti mokslininkų bendruomenė. Tačiau tokiems optiniams elementams, kad jie pasižymėtų reikiamomis savybėmis pasirinktame elektromagnetinių bangų (EM) ruože, reikalingi nauji kūrimo metodai ir būdai. Sparčiai tobulėjant THz mokslui ir technologijoms, didėja paklausa didelio našumo optinių komponentų, kuriuos būtų lengviau pagaminti ir sklandžiai integruoti su puslaidininkiniais lustais [8],[9],[10]. Dėl DOE efektyvumo ir universalumo THz mokslo ir technologijų bendruomenė skiria ypatingą dėmesį tokios optikos vystymui ir tobulinimui bei fotonikos integravimui ant lusto su kitais komponentais, tokiais kaip THz detektoriai ir šaltiniai.

Doktorantūros darbe pagrindinis dėmesys skiriamas DOE kūrimui ir tyrimams dažnių ruože nuo 0,1 iki 1,0 THz, kurie apima MPZP lęšius, ketvirčio ir pusės bangos plokšteles (QWP ir HWP, atitinkamai), pritaikant

didelio-kontrasto gardelės (HCG) ypatumus, dvimačių (2D) rezonatorių matricas (meta-paviršiai), panaudojant puslaidininkinį silicį, kurio santykinai didelis lūžio rodiklis, bei ploną metalinę nerūdijančio plieno plėvelę, kurios santykinai didelis elektrinis laidumas. Darbe valdant THz spinduliuotės fazės, amplitudės ir poliarizacijos būsenas siekiama sukurti DOE optiką turinčią papildomų funkcijų, tokių kaip pluošto fokusavimas, poliarizacijos valdymas, neatspindintysis paviršius bei maskavimas.

Darbo tikslas

Tikslas yra sukurti difrakcinę optiką naudojant puslaidininkinio bei metalinio laidumo elementus, kuri pasižymėtų neatspindėjimo bei padidinto pralaidumo ypatumais siekiant pluošto fokusavimo bei poliarizacijos valdymo funkcionalumo plačiame THz dažnių diapazone.

Darbo uždaviniai

1. Sukurti ir ištirti hibridinius silicio MPZP lęšius THz dažniams, siekiant sumažinti išorinių zonų dizaino sudėtingumą ir gamybos laiką, išlaikant fokusavimo parametrus.
2. Sukurti ir ištirti HCG fazines plokšteles iš silicio, veikiančias kaip QWP ir HWP, kurios veiksmingai kontroliuoja poliarizacijos būseną bei pasižymi mažais atspindžio nuostoliais plačiame dažnių ruože nuo 0,1 THz iki 1 THz.
3. Sukurti ir ištirti meta-paviršius iš metalo bei silicio meta-atomų, kuriuos sudaro koncentrinis diskas ir žiedas, išdėstant meta-atoms periodiškai kvadratinėje gardelėje kaip 1×1 , 2×2 , 5×5 , 10×10 bei begalinio skaičiaus rezonatorių masyvas, siekiant sumažinti pluoštelio sklaidą tolimajame lauke bei pasiekti padidintą meta-paviršiaus skaidrumą plačiame THz dažnių diapazone.

Darbo naujumas

1. Sukurti ir pademonstruoti hibridiniai daugiafaziai Frenelio zoninių plokštelių (H-MPZP) lęšiai, kuriuose hibridiniu būdu suderinti fazės kvantavimo lygmenys, siekiantys panašų ar net geresnį fokusavimo našumą lyginant su įprasto dizaino MPZP, turinčiomis nekintantį fazių kvantavimo lygmenų skaičių.

2. Sukurtos vienasluoksnės HCG tipo fazinės plokštelės su neatspindėjimo savybėmis, veikiančios kaip ketvirčio bangos plokštelės (QWP) dažnių ruože nuo 0,3 iki 0,5 THz, užtikrinant 200 GHz dažnių juostos plotį.
3. Pasiūlyta abiejose silicio plokštelės pusėse integruoti skirtingo tipo periodines gardeles siekiant pagerinti pralaidumo parametrus ketvirčio bangos plokštelėms (QWP) bei pusės bangos plokštelėms (HWP). Nauja struktūra apjungia ir QWP, ir HWP charakteristikas bei demonstruoja didesnį pralaidumą TM poliarizacijai siekiantį nuo 90% iki 100% plačiame dažnių diapazone nuo 0,4 iki 0,9 THz.
4. Pasiūlyta HCG tipo fazinės plokštelės plokščią paviršių papildomai struktūrizuoti sinusoide su 10 μm amplitude ir 1500 μm periodu TE poliarizacijos kryptimi, kad iki 10 % sumažinti signalo amplitudės moduliaciją dėl Fabry-Perot efekto tiek TE, tiek TM poliarizacijose dažnių diapazone nuo 0,3 iki 0,9 THz.
5. Sukurtas meta-paviršiai, sudaryti iš skirtingo skaičiaus meta-atomų rezonatorių suformuotų plonoje nerūdijančio plieno folijoje siekiant tirti meta-atomų tarpusavio sąveiką. Nustatyta, jog padidėjus rezonatorių skaičiui masyve nuo 1 iki 10×10 padidėja rezonanso smailės plotis pusės amplitudės aukštyje (FWHM) nuo 40 GHz iki 150 GHz, atitinkamai sumažėja rezonanso kokybės koeficientas nuo 8,5 iki 2,1.
6. Išmatuoti THz pralaidumo spektrai meta-paviršiams sudarytiems iš mažesnio nei bangos ilgio vieno rezonatoriaus bei 2×2 rezonatorių suformuotų plonoje nerūdijančio plieno folijoje.
7. Sukurtas meta-paviršius iš laisvai stovinčių silicio meta-atomų, sudarytų iš koncentrinų diskų ir žiedų rezonatorių, demonstruojantis anapolinę būseną, nulemiančią meta-paviršiaus didesnį optinį skaidrumą, siekiantį iki 70 % dažnių diapazone nuo 0,5 iki 0,7 THz.

Ginamieji teiginiai

1. Hibridinės daugiafazinės zoninės plokštelės, su skirtingais kvantavimo lygiais centrinėje zonoje $Q = 8$ ir išorinėse zonose $Q = 4$, kur prie fazės kvantavimo vertės papildomai pridedamas $\pi/4$ dydis, pasižymi iki 10 % didesniu fokusavimo stiprumu ir iki 50 % trumpesniu gamybos laiku, lyginant su įprastomis $Q = 8$ daugiafazinėmis zoninėmis plokštelėmis.
2. Silicio didelio kontrasto gardelės, kurių briaunos aukštis yra 200 μm , periodiškumas 100 μm , o šoninės sienelės pokrypis kiekvienoje pusėje yra 11 laipsnių, sukuria $\pi/2$ fazių skirtumą tarp statmenai orientuotų elektromagnetinės bangos tiesinių poliarizacijų dažnių diapazone nuo 0,3

iki 0,5 THz, užtikrinant juostos plotį 200 GHz, ko pakanka sukurti ketvirčio bangos fazines plokšteles, tinkančias efektyviam THz pluošto poliarizacijos valdymui.

3. Sujungiant metalo elektriniu laidumu pasižyminčius meta-atomus, kuriuos sudaro koncentriniai disko ir žiedo rezonatoriai su rezonanso smaile ties 350 GHz, į meta-paviršių išplinta rezonanso dažnių juostos plotis (nuo 40 GHz iki 154 GHz) ir sumažėja kokybės koeficientas (nuo 8,5 iki 2,1), remiantis vieno meta-atomo ir 10×10 metaatomų masyvo atvejais, dėl pakitusios gretimų meta-atomų tarpusavio sąveikos.
4. Sujungiant mažo elektrinio laidumo silicio meta-atomus, kuriuos sudaro koncentriniai disko ir žiedo rezonatoriai, į meta-paviršių pasiekiamas visiškai skaidrumas dėl perspinduliavimo kompensavimo tolimajame lauke dažnių ruože nuo 0,5 iki 0,7 THz, kai kartu egzistuoja jungtinis anapolinis ir atskirų anapolių rezonansai.

Autoriaus indėlis

Autorius suskaičiavo ir išmatavo MPZP lęšių charakteristikas, fokusavimo efektyvumą [P1]. Autorius suskaičiavo HCG fazinių plokštelių charakteristikas ir pralaidumo efektyvumą, atliko QWP plokštelių poliarizacijos charakteristikų matavimus, ir iš dalies bendradarbiaudamas su bendraautoriais prisidėjo prie matavimų su THz-TDS ir VNA sistemomis [P2]. Autorius, bendradarbiaudamas su [P3] bendraautoriais, suskaičiavo S parametrus visiems meta-paviršiams, reikšmingai prisidėjo prie daugiapolių analizės bei bandinių eksperimentinių tyrimų su THz-TDS ir VNA sistemomis. Autorius atliko skaičiavimus dalies S parametrų charakteristikų silicio-pagrindu sukurtiems meta-paviršiams [P4].

Daugumos bandinių modeliavimas, gamyba, charakterizavimas ir eksperimentiniai tyrimai buvo atlikti Fizinių mokslų ir technologijos centre (FTMC), Lietuvoje. Dalis HCG fazinių plokštelių ir meta-paviršių tyrimų [P2-P3] buvo atlikti Duisburgo-Eseno universitete Duisburge, Vokietijoje ir Lilio universitete Lilyje, Prancūzijoje.

Lazerinės abliacijos būdu bandinius pagamino dr. Simonas Indrišūnas iš FTMC Lazerinės mikrogamybos laboratorijos. Autorius kartu su dr. Daniil Pashnev, FTMC, atliko bandinių THz-TDS matavimus, su prof. Guillaume'u Ducournau iš Elektronikos, mikroelektronikos ir nanotechnologijų instituto (IEMN), Prancūzijoje, atliko VNA matavimus, bei su dr. Andreas K. Klien priežiūroje prof. Andreas Stohr iš Optoelektronikos skyriaus, Duisburgo-Eseno universitete, Vokietijoje, atliko dalį THz FDS matavimų.

Rezultatų apžvalga

THz difrakciniai lęšiai

3.1 skyriuje nagrinėjamas THz difrakcinių lęšių kūrimas ir optimizavimas, ypatingą dėmesį skiriant hibridinėms daugiafazėms zoninėms plokštelėms (H-MPZP). Šie lęšiai buvo pagaminti iš silicio plokštelės, kad sufokusuotų 585 GHz dažnio spinduliuotę. Nors daugiafazės zoninės plokštės (MPZP) su dideliu fazės kvantavimo lygiu (Q) pasiekia beveik 100% difrakcijos efektyvumą, jų gamyba sudėtinga dėl tikslių mažų matmenų išorinių zonų reikalavimo. Siekiant tai išspręsti sukūrtos H-MPZP modifikuojant MPZP su $FZ = 3$ ir $Q = 8$, kur optimalus zonų kvantavimo skaičius pasirinktas atsižvelgiant į gamybos laiką išlaikant fokusavimo efektyvumą.

Optimizavimo metu siekėme sumažinti fazių kvantavimo skaičių išorinėse H-MPZP zonose. Buvo sukurti du variantai: H-MPZP1, kur Q buvo sumažintas nuo 8 iki 4 trečioje Frenelio zonoje (FZ3), ir H-MPZP2, kur Q buvo sumažintas antroje ir trečioje Frenelio zonose (FZ2, FZ3). Modeliavimo rezultatai parodė, kad optimizavimas leido padidinti abiejų tipų hibridinių lęšių fokusavimo stiprumą iki 10 % (0,4 dB), lyginant su pradinio MPZP atveju, dėl sumažintų reikalavimų struktūrų dydžiams ir sumažintų šešėliavimo efektų.

Ekspertiškai H-MPZP2 parodė šiek tiek geresnį fokusavimo padidėjimą apie 6 %, palyginti su H-MPZP1, išlaikant maždaug 200 GHz dažnių juostos plotį. Be to, buvo 50 % sutrumpintas gamybos laikas dėl supaprastintų profilių išorinėse zonose. Dėl to efektyvesni H-MPZP lęšiai gali būti perspektyvi alternatyva MPZP pirmtakams.

HCG tipo bangų plokštės

3.2 skyriuje aptariamas didelio kontrasto gardelės (HCG) tipo fazinių plokštelių kūrimas bei optimizavimas THz dažnių ruožui. Tokios fazinės plokštelės sukurtos efektyviam poliarizacijos valdymui, įvedant dirbtinį dvigubo lūžio efektą periodinėse mažų matmenų gardelėse, kurios gali būti suformuojamos ant silicio plokštelių paviršiaus.

Vienas iš pagrindinių rezultatų buvo praktinis pademonstravimas, kad HCG gali veikti kaip ketvirčio bangos fazinės plokštelės (QWP) plačiame 0,3 – 0,5 THz dažnių diapazone, užtikrinant juostos plotį iki 200 GHz, sukuriant 90° fazių skirtumą ($\pi/2$) tarp TE ir TM poliarizacijų. Skaitmeninis FDTD modeliavimas bei eksperimentiniai THz-TDS ir VNA matavimai parodė gerą rezultatų sutapimą bei QWP tinkamumą plačiajuosčio ryšio THz sistemose.

Siekiant pagerinti našumą, išilgai TE poliarizacijos ašies, pasiūlėme gardelės plokščių paviršių modifikuoti į periodinę sinusoidinės formos gardelę. Reikšmingai sumažintas Fabry-Perot efekto poveikis fazinės plokštelės charakteristikoms naudojant papildomą 25 μm amplitudės ir 1500 μm periodo sinusinę paviršiaus moduliaciją HCG komponentui, kurio bendras storis buvo 200 μm . Atlikti tyrimai parodė, kad tokia sinusiniu dėsniu moduluota HCG tipo fazinė plokštelė pasižymėjo žymiai mažesne Fabry-Perot osciliacijos amplitudė tiek TE, tiek TM poliarizacijų spektruose, palyginti su plokščio paviršiaus HCG. Reiktų pažymėti, kad TM poliarizacijoje mažesnę Fabry-Perot osciliacijos amplitudę pavyko pasiekti panaudojant nedidelį (11 laipsnių) šoninių sienelių nuolydį didelio kontrasto gardelėje, kas leido užtikrinti tolygesnį lūžio rodiklio pasikeitimą perėjime tarp dielektriko ir oro. Tyrimų rezultatai atskleidė, pralaidumo sumažėjimą aukštesnių dažnių srityje, kas rodo būtinybę ieškoti papildomų sprendimų naujame dizaine.

Tolesnis patobulinimas buvo atliktas įdiegus dvipusę sinusoidinę gardelę, kuri padidino pralaidumą ir sumažino nuo poliarizacijos priklausomus nuostolius. Bendras pralaidumas viršijo 60 % dažnių ruože nuo 0,3 iki 0,9 THz, todėl tokios HCG-tipo fazinės plokštės pasirodė esančios veiksmingos tiek QWP, tiek pusės bangos plokštelė (HWP) taikymuose.

Gauti rezultatai rodo, kad HCG tipo fazinės plokštės su papildoma sinusine paviršiaus moduliacija pasižymi didesniu efektyvumu plačiame dažnių diapazone, todėl yra perspektyvios taikymuose kur reikalingi maži nuostoliai THz pluoštelio poliarizacijos valdymo sprendimuose.

Laisvai stovintys meta-paviršiai

Metalinio-laidumo meta-paviršiai

3.3 skyriuje aprašyti laisvai stovinčių (nėra padėklo) meta-paviršių, sudarytų iš meta-atomų pagamintų iš plonos metalinio elektrinio laidumo folijos tyrimai. Pirma, dėmesys sutelkiamas į metalinius meta-paviršius, kur skirtingas meta-atomų skaičius yra išdėstytas kvadratinėje gardelėje pasitelkiant ploną nerūdijančio plieno foliją kurios storis 50 μm , siekiant iširti meta-atomų sąveikos poveikį rezonansinėms pralaidumo charakteristikoms. Tyrimas apima pavienius meta-atomus, 2×2 , 5×5 ir 10×10 meta-atomų masyvus, kurių pralaidumo spektrinės charakteristikos analizuojamos pasitelkiant FDTD skaičiavimus bei eksperimentinius matavimus panaudojant THz-TDS ir VNA sistemas.

Tyrimų rezultatai parodė, kad meta-atomų skaičiaus masyve padidinimas žymiai padidina rezonansinės smailės juostos plotį. Vienas meta-atomas pasižymėjo siauru rezonansu ties 0,34 THz dažniu, kurio kokybės koeficientas (q faktorius) yra 8,5, o dažnių juostos plotis – 40 GHz. Tačiau sujungus metaatomus į 2×2 masyvą, jų rezonansinės smailės juostos plotis padidėjo iki 100 GHz, q koeficientas sumažėjo iki 3,5, tai rodo tarpusavio sąveiką tarp sujungtų meta-atomų meta-paviršiuje. Papildomas meta-atomų masyvo išplėtimas iki 5×5 elementų sąlygojo platesnį iki 116 GHz juostos pločio rezonansą ties 0,33 THz, kurio q koeficientas buvo tik 2,8. Meta-atomų masyvą išplėtus iki 10×10 dydžio, rezonansinis ypatumas stebimas meta-paviršiaus pralaidumo spektre dar labiau išplito, o tai rodo, kad abipusė meta-atomų sąveika tokio dydžio masyvuose vis dar yra reikšminga. Rezonansinio ypatumo išplitimas buvo priskirtas stiprioms elektrinių ir magnetinių dipolių ir kvadrupolių sąveikoms, ypač magnetinio H laukų sąveika sujungimuose (tiltuose), naudojamuose meta-atomams sujungti. Meta-paviršius, kurį sudarė 10×10 meta-atomų masyvas, demonstravo plačiausią iki 154 GHz juostos plotį ir atitinkamai mažiausią kokybę, q koeficientas buvo apie 2,1, rezonansiniam ypatumui, kurio centrinis dažnis buvo ties 0,32 THz.

Atlikta daugiapolių analizė atskleidė, kad vieno meta-atomo konfigūracijoje rezonanso atveju dominuoja elektrinis dipolinis (P) momentas. Tačiau didesnėje meta-atomų matricose magnetinio dipolinio (M) momento ir magnetinio kvadrupolinio (Q_m) momento įnašai yra didesni. Lauko pasiskirstymo analizė patvirtino, kad magnetiniai H laukai yra stipriai lokalizuoti tiltuose jungiančiuose meta-atomus, todėl matricose iš didesnio skaičiaus meta-atomų rezonansinis ypatumas išplinta ir jo kokybė sumažėja.

Silicio meta-paviršiai

Sukurti ir ištirti laisvai stovintys (nėra padėklo) meta-paviršiai pagaminti iš silicio siekiant pademonstruoti optinį skaidrumą plačiame THz diapazone. Tokius meta-paviršius sudarė masyvas koncentrinų diskų ir žiedų, pagamintų iš plonos silicio membranos, kurios nedidelis elektrinis laidumas buvo apie 10 S/m. Tyrimo rezultatai parodė, kad optinis skaidrumas plačiame THz dažnių diapazone pasiekiamas destruktvyviai kompensuojant elektrinio dipolinio momento spinduliavimą tolimojoje zonoje, kas žinoma, kaip anapolio rezonansas.

Daugiapolių analizė parodė, kad jungtinis anapolių rezonansas yra irgi svarbus siekiant užtikrinti meta-paviršiaus optinį skaidrumą plačiame dažnių ruože. Elektrinio dipolinio momento spinduliavimas gali būti slopinamas (kompensuojamas) toroidinio dipolinio momento spinduliavimu, dėl ko

tolimajame lauke efektyviai sumažėja atspindys ir gaunamas beveik didelis pralaidumas (pilnas optinis skaidrumas) dažnių diapazone 0,5–0,7 THz. Silicio pagrindo meta-paviršiaus plačiąjuostis skaidrumas priskiriamas daugelio anapolio rezonansų, įskaitant sudėtines anapolio būsenas, sąveikai. Tiksliau, buvo išskirti du anapolio rezonansai ties 0,520 THz ir ties 0,625 THz dažniais bei jungtinis anapolio rezonansas dažnių ruože 0,54–0,56 THz. Šiame diapazone visi daugiapoliai momentai, išskyrus magnetinį dipolį, buvo slopinami, veiksmingai pašalinant sklaidą ir įgalinant didelį pralaidumą.

Ekspimentiniai tyrimai parodė, kad pralaidumas išlieka didelis (iki 70 %) ir santykinai nepriklauso nuo dažnio diapazone nuo 0,5 THz iki 0,7 THz. Atitinkamai, atspindžio vertės neviršija 20 %, tai rodo sumažintą sklaidą tolimojoje zonoje. Pažymėtina, kad šiame skaidrumo lange išmatuoti meta-paviršiaus su dvejomis statmenai orientuotomis poliarizacijomis pralaidumo spektrai rodė tik nedidelius skirtumus, tas reiškia mažą anizotropijos įvedimą dėl sujungimų (tiltelių) tarp meta-atomų panaudojimo.

Galiausiai ištyrėme pralaidumo spektrų priklausomybę nuo kritimo kampo. Buvo nustatyta, kad kai meta paviršiaus pasuktas iki 45 laipsnių kampu pralaidumas tiesiškai poliarizuotam pluošteliui sumažėjo tik apie 10% skaidrumo lange, kai kituose dažniuose pralaidumas stipriai priklausė nuo tiesinės poliarizacijos krypties ir pasukimo kampo. Nustatyta silpna pralaidumo priklausomybė nuo kritimo kampo skaidrumo lange atskleidė anapolio rezonanso buvimą ties 0,52 THz dažniu. Pralaidumo spektro jautrumas posūkio kampui buvo ypač ryškus ties 0,55 THz ir 0,625 THz dažniais, kas buvo priskirta sąveikai tarp elementų (tiltų) panaudotų meta-atomams sujungti į meta-paviršių. Nepaisant šios spektrų kampinės priklausomybės, dipolinių momentų spinduliuotės slopinimas tolimojoje zonoje buvo veiksmingas.

Išvados

Darbo metu buvo sukurti ir ištirti metaliniai bei puslaidininkiniai difrakciniai optiniai elementai skirti THz dažnių diapazonui, įskaitant hibridinius MPZP lęšius, didelio kontrasto gardelės tipo fazines plokšteles bei meta-paviršius, kuriems nereikalingas padėklas. Pagrindinės darbo išvados:

- 1) Silicio hibridinių MPZP lęšių gamyba yra supaprastinama išorinėse zonose dvigubai sumažinus kvantavimo lygių skaičių ir prie fazės kvantavimo vertės pridėjus papildomai $\pi/4$ dydį, taip pat

- pasiekiant didesnę fokusavimo stiprumą dėl sumažinto šešėliavimo efekto.
- 2) Galimybė naudoti didelio skersmens lazerinį pluoštelį leidžia našiai gaminti didesnių matmenų hibridinius MPZP lęšius, todėl jie yra itin perspektyvūs aukštadažniuose taikymuose.
 - 3) Iš vientiso silicio sukurta didelio kontrasto gardelės plokštelė gali būti naudojama kaip ketvirčio bangos fazinė plokštelė plačiame 0,3–0,5 THz dažnių diapazone, užtikrinant juostos plotį iki 200 GHz
 - 4) Didelio kontrasto gardelės sienelių nuolydis kartu su statmena kryptimi orientuota mažos amplitudės sinusinio profilio gardele efektyviai slopina Fabry-Pérot efektą, užtikrinant pastovų banginės fazinės plokštelės veikimą plačiame THz dažnių ruože.
 - 5) Meta-atomų išdėstymas į meta-paviršių mažesniais atstumais už rezonansinį bangos ilgį sąlygoja stiprią jų tarpusavio sąveiką, dėl ko meta-paviršiaus rezonansinės charakteristikos skiriasi nuo pavienio meta-atomo.
 - 6) Dėl tarpusavio sąveikos efektų išplinta rezonansinės smailės plotis nuo 40 GHz iki 154 GHz bei sumažėja rezonanso kokybė beveik keturis kartus, padidinus masyve meta-atomų skaičių nuo 1×1 iki 10×10 .
 - 7) Panaudojus daugiapolių analizę tokie dideli pokyčiai buvo paaiškinti stipria magnetinių laukų sąveika. Šie rezultatai siūlo vertingas meta-paviršių kūrimo strategijas, leidžiančias optimizuoti jų charakteristikas, kurios gali būti panaudotos kuriant našius jutiklius, filtrus ir sugėriklius.
 - 8) Pavyko iš silicio sukurti meta-paviršių, sudarytą iš kvadratinėje gardelėje išdėstytų koncentrinį diskų ir žiedų masyvo, kuris demonstruoja padidintą skaidrumą plačiame dažnių ruože dėl daugelio anapolių rezonansų, įskaitant ir sudėtinių anapolių, pasireiškimo. Pralaidumo ir atspindžio charakteristikos tokio meta-paviršiaus yra stabilios plačiame elektromagnetinės bangos kritimo kampų diapazone nepriklausomai nuo tiesinės poliarizacijos krypties 0,5–0,7 THz dažnių ruože dėl efektyvaus perspinduliavimo nuostolių slopinimo.

REFERENCES

- [1] F. L. Wentworth, J. C. Wiltse, and F. Sobel, “Quasi-Optical Surface Waveguide and Other Components for the 100- to 300-Gc Region,” *IEEE Trans. Microw. Theory Tech.*, vol. 9, no. 6, pp. 512–518, Nov. 1961, doi: 10.1109/TMTT.1961.1125382.
- [2] D. Headland, Y. Monnai, D. Abbott, C. Fumeaux, and W. Withayachumnankul, “Tutorial: Terahertz beamforming, from concepts to realizations,” *APL Photonics*, vol. 3, no. 5, May 2018, doi: 10.1063/1.5011063.
- [3] Nanfang Yu *et al.*, “Plasmonics for Laser Beam Shaping,” *IEEE Trans. Nanotechnol.*, vol. 9, no. 1, pp. 11–29, Jan. 2010, doi: 10.1109/TNANO.2009.2029099.
- [4] D. M. Mittleman, “Twenty years of terahertz imaging [Invited],” *Opt. Express*, vol. 26, no. 8, p. 9417, Apr. 2018, doi: 10.1364/OE.26.009417.
- [5] T. Kleine-Ostmann and T. Nagatsuma, “A Review on Terahertz Communications Research,” *J. Infrared, Millimeter, Terahertz Waves*, vol. 32, no. 2, pp. 143–171, Feb. 2011, doi: 10.1007/s10762-010-9758-1.
- [6] A. Siemion, “The Magic of Optics—An Overview of Recent Advanced Terahertz Diffractive Optical Elements,” *Sensors*, vol. 21, no. 1, p. 100, Dec. 2020, doi: 10.3390/s21010100.
- [7] W. T. Chen and F. Capasso, “Will flat optics appear in everyday life anytime soon?,” *Appl. Phys. Lett.*, vol. 118, no. 10, Mar. 2021, doi: 10.1063/5.0039885.
- [8] J. Engelberg and U. Levy, “Achromatic flat lens performance limits,” *Optica*, vol. 8, no. 6, p. 834, Jun. 2021, doi: 10.1364/OPTICA.422843.
- [9] S. Al-Daffaie, A. J. Jumaah, V. L. Rubio, and T. Kusserow, “Design and implementation of a terahertz lens-antenna for a photonic integrated circuits based THz systems,” *Sci. Rep.*, vol. 12, no. 1, p. 1476, Jan. 2022, doi: 10.1038/s41598-022-05338-0.
- [10] L. Minkevičius, V. Tamošiūnas, K. Madeikis, B. Voisiat, I. Kašalynas, and G. Valušis, “On-chip integration of laser-ablated zone plates for detection enhancement of InGaAs bow-tie terahertz detectors,” *Electron. Lett.*, vol. 50, no. 19, pp. 1367–1369, Sep. 2014, doi: 10.1049/el.2014.1893.
- [11] A. G. Michette, “Diffractive Optics II Zone Plates,” in *Optical Systems for Soft X Rays*, Boston, MA: Springer US, 1986, pp. 165–215. doi: 10.1007/978-1-4613-2223-8_8.
- [12] M. Rachon *et al.*, “Geometrical Aberration Suppression for Large Aperture Sub-THz Lenses,” *J. Infrared, Millimeter, Terahertz Waves*, vol. 38, no. 3, pp. 347–355, Mar. 2017, doi: 10.1007/s10762-016-0342-1.
- [13] A. Siemion *et al.*, “Diffractive paper lens for terahertz optics,” *Opt.*

- Lett.*, vol. 37, no. 20, p. 4320, Oct. 2012, doi: 10.1364/OL.37.004320.
- [14] V. M. Vedernikov *et al.*, “Diffractive elements for a free electron laser,” *Optoelectron. Instrum. Data Process.*, vol. 46, no. 4, pp. 365–375, Aug. 2010, doi: 10.3103/S8756699010040102.
- [15] W. D. Furlan, V. Ferrando, J. A. Monsoriu, P. Zagrajek, E. Czerwińska, and M. Szustakowski, “3D printed diffractive terahertz lenses,” *Opt. Lett.*, vol. 41, no. 8, p. 1748, Apr. 2016, doi: 10.1364/OL.41.001748.
- [16] A. Siemion *et al.*, “Paraffin Diffractive Lens for Subterahertz Range—Simple and Cost Efficient Solution,” *IEEE Trans. Terahertz Sci. Technol.*, vol. 11, no. 4, pp. 396–401, Jul. 2021, doi: 10.1109/TTHZ.2021.3063809.
- [17] V. B. Yurchenko, M. Ciydem, M. Gradziel, J. A. Murphy, and A. Altintas, “Double-sided split-step MM-wave Fresnel lenses: design, fabrication and focal field measurements,” *J. Eur. Opt. Soc. Publ.*, vol. 9, p. 14007, Feb. 2014, doi: 10.2971/jeos.2014.14007.
- [18] T. V. Kononenko *et al.*, “Silicon kinoform cylindrical lens with low surface roughness for high-power terahertz radiation,” *Opt. Laser Technol.*, vol. 123, p. 105953, Mar. 2020, doi: 10.1016/j.optlastec.2019.105953.
- [19] S. Indrisiunas, L. Minkevicius, V. Tamosiunas, G. Valusis, G. Raciukaitis, and I. Kasalynas, “Laser-processed diffractive optics for terahertz waves,” in *2019 IEEE 8th International Conference on Advanced Optoelectronics and Lasers (CAOL)*, Sep. 2019, pp. 1–4. doi: 10.1109/CAOL46282.2019.9019480.
- [20] A. N. Agafonov *et al.*, “Silicon diffractive optical elements for high-power monochromatic terahertz radiation,” *Optoelectron. Instrum. Data Process.*, vol. 49, no. 2, pp. 189–195, Mar. 2013, doi: 10.3103/S875669901302012X.
- [21] D. K. Woo, K. Hane, and S.-K. Lee, “Fabrication of a multi-level lens using independent-exposure lithography and FAB plasma etching,” *J. Opt. A Pure Appl. Opt.*, vol. 10, no. 4, p. 044001, Apr. 2008, doi: 10.1088/1464-4258/10/4/044001.
- [22] P. Pal and K. Sato, “A comprehensive review on convex and concave corners in silicon bulk micromachining based on anisotropic wet chemical etching,” *Micro Nano Syst. Lett.*, vol. 3, no. 1, p. 6, Dec. 2015, doi: 10.1186/s40486-015-0012-4.
- [23] B. Voisiat, S. Indrišiūnas, R. Šniaukas, L. Minkevičius, I. Kašalynas, and G. Račiukaitis, “Laser processing for precise fabrication of the THz optics,” Feb. 2017, p. 100910F. doi: 10.1117/12.2253634.
- [24] G. Raciukaitis, “Ultra-Short Pulse Lasers for Microfabrication: A Review,” *IEEE J. Sel. Top. Quantum Electron.*, vol. 27, no. 6, pp. 1–12, Nov. 2021, doi: 10.1109/JSTQE.2021.3097009.
- [25] L. Minkevičius *et al.*, “Terahertz multilevel phase Fresnel lenses fabricated by laser patterning of silicon,” *Opt. Lett.*, vol. 42, no. 10, p.

- 1875, May 2017, doi: 10.1364/OL.42.001875.
- [26] S. Indrišiūnas *et al.*, “Laser-processed diffractive lenses for the frequency range of 47 THz,” *Opt. Lett.*, vol. 44, no. 5, p. 1210, Mar. 2019, doi: 10.1364/OL.44.001210.
- [27] J. A. Dobrowolski and F. Ho, “High performance step-down AR coatings for high refractive-index IR materials,” *Appl. Opt.*, vol. 21, no. 2, p. 288, Jan. 1982, doi: 10.1364/AO.21.000288.
- [28] M. Tamosiunaite *et al.*, “Focusing of Terahertz Radiation With Laser-Ablated Antireflective Structures,” *IEEE Trans. Terahertz Sci. Technol.*, vol. 8, no. 5, pp. 541–548, Sep. 2018, doi: 10.1109/TTHZ.2018.2859619.
- [29] H. Sakurai *et al.*, “Terahertz broadband anti-reflection moth-eye structures fabricated by femtosecond laser processing,” *OSA Contin.*, vol. 2, no. 9, p. 2764, Sep. 2019, doi: 10.1364/OSAC.2.002764.
- [30] S. Indrišunias *et al.*, “Laser-Ablated Silicon in the Frequency Range From 0.1 to 4.7 THz,” *IEEE Trans. Terahertz Sci. Technol.*, vol. 9, no. 6, pp. 581–586, Nov. 2019, doi: 10.1109/TTHZ.2019.2939554.
- [31] Y.-H. Liu, K.-K. Kuo, C.-W. Cheng, and A.-C. Lee, “Femtosecond laser two-beam interference applied to 4H-SiC surface hierarchical micro-nano structure fabrication,” *Opt. Laser Technol.*, vol. 151, p. 108081, Jul. 2022, doi: 10.1016/j.optlastec.2022.108081.
- [32] R. Takaku *et al.*, “Broadband, millimeter-wave anti-reflective structures on sapphire ablated with femto-second laser,” *J. Appl. Phys.*, vol. 128, no. 22, Dec. 2020, doi: 10.1063/5.0022765.
- [33] R. Takaku *et al.*, “Large diameter millimeter-wave low-pass filter made of alumina with laser ablated anti-reflection coating,” *Opt. Express*, vol. 29, no. 25, p. 41745, Dec. 2021, doi: 10.1364/OE.444848.
- [34] S. Orlov *et al.*, “Light Engineering and Silicon Diffractive Optics Assisted Nonparaxial Terahertz Imaging,” *Laser Photon. Rev.*, vol. 18, no. 5, May 2024, doi: 10.1002/lpor.202301197.
- [35] M. Chen, F. Fan, S.-T. Xu, and S.-J. Chang, “Artificial high birefringence in all-dielectric gradient grating for broadband terahertz waves,” *Sci. Rep.*, vol. 6, no. 1, p. 38562, Dec. 2016, doi: 10.1038/srep38562.
- [36] C.-S. Yang *et al.*, “The complex refractive indices of the liquid crystal mixture E7 in the terahertz frequency range,” *J. Opt. Soc. Am. B*, vol. 27, no. 9, p. 1866, Sep. 2010, doi: 10.1364/JOSAB.27.001866.
- [37] D. Grischkowsky, S. Keiding, M. van Exter, and C. Fattinger, “Far-infrared time-domain spectroscopy with terahertz beams of dielectrics and semiconductors,” *J. Opt. Soc. Am. B*, vol. 7, no. 10, p. 2006, Oct. 1990, doi: 10.1364/JOSAB.7.002006.
- [38] Y. Gong, Z. Zhang, J. Tang, L. Ma, and K. Pang, “Research progress on terahertz achromatic broadband polarization wave plates,” *Opt. Laser Technol.*, vol. 166, p. 109633, Nov. 2023, doi:

- 10.1016/j.optlastec.2023.109633.
- [39] Z. Chen, Y. Gong, H. Dong, T. Notake, and H. Minamide, "Terahertz achromatic quarter wave plate: Design, fabrication, and characterization," *Opt. Commun.*, vol. 311, pp. 1–5, Jan. 2013, doi: 10.1016/j.optcom.2013.08.039.
- [40] A. Moreno-Penarrubia, S. A. Kuznetsov, and M. Beruete, "Ultrathin Subterahertz Half-Wave Plate With High Conversion Efficiency Based on Zigzag Metasurface," *IEEE Trans. Antennas Propag.*, vol. 68, no. 11, pp. 7700–7704, Nov. 2020, doi: 10.1109/TAP.2020.2993308.
- [41] Y. Nakata, Y. Taira, T. Nakanishi, and F. Miyamaru, "Freestanding transparent terahertz half-wave plate using subwavelength cut-wire pairs," *Opt. Express*, vol. 25, no. 3, p. 2107, Feb. 2017, doi: 10.1364/OE.25.002107.
- [42] Y. Yuan, J. Cheng, X. Dong, F. Fan, X. Wang, and S. Chang, "Terahertz dual-band polarization control and wavefront shaping over freestanding dielectric binary gratings with high efficiency," *Opt. Lasers Eng.*, vol. 143, p. 106636, Aug. 2021, doi: 10.1016/j.optlaseng.2021.106636.
- [43] A. D'Arco, L. Tomarchio, S. Macis, M. Petrarca, and S. Lupi, "Achromatic terahertz quarter-wave Fresnel rhomb retarder," *Appl. Phys. Lett.*, vol. 122, no. 24, Jun. 2023, doi: 10.1063/5.0151366.
- [44] B. Päivänranta, N. Passilly, J. Pietarinen, P. Laakkonen, M. Kuittinen, and J. Tervo, "Low-cost fabrication of form-birefringent quarter-wave plates," *Opt. Express*, vol. 16, no. 21, p. 16334, Oct. 2008, doi: 10.1364/OE.16.016334.
- [45] Y. Shimotsuma, P. G. Kazansky, J. Qiu, and K. Hirao, "Self-Organized Nanogratings in Glass Irradiated by Ultrashort Light Pulses," *Phys. Rev. Lett.*, vol. 91, no. 24, p. 247405, Dec. 2003, doi: 10.1103/PhysRevLett.91.247405.
- [46] S. R. Ayyagari *et al.*, "Broadband high-contrast-grating-type waveplates for the terahertz range," *Opt. Express*, vol. 32, no. 9, p. 15870, Apr. 2024, doi: 10.1364/OE.521532.
- [47] W. Liu *et al.*, "Highly Efficient Broadband Wave Plates Using Dispersion-Engineered High-Index-Contrast Subwavelength Gratings," *Phys. Rev. Appl.*, vol. 11, no. 6, p. 064005, Jun. 2019, doi: 10.1103/PhysRevApplied.11.064005.
- [48] V. Karagodsky and C. J. Chang-Hasnain, "Physics of near-wavelength high contrast gratings," *Opt. Express*, vol. 20, no. 10, p. 10888, May 2012, doi: 10.1364/OE.20.010888.
- [49] C. J. Chang-Hasnain and W. Yang, "High-contrast gratings for integrated optoelectronics," *Adv. Opt. Photonics*, vol. 4, no. 3, p. 379, Sep. 2012, doi: 10.1364/AOP.4.000379.
- [50] J. Zi *et al.*, "Antireflection-assisted all-dielectric terahertz metamaterial polarization converter," *Appl. Phys. Lett.*, vol. 113, no.

- 10, Sep. 2018, doi: 10.1063/1.5042784.
- [51] T. Nitta *et al.*, “Broadband Pillar-Type Antireflective Subwavelength Structures for Silicon and Alumina,” *IEEE Trans. Terahertz Sci. Technol.*, vol. 7, no. 3, pp. 295–301, May 2017, doi: 10.1109/TTHZ.2017.2692045.
- [52] R. Koike, M. Matoba, S. Kawano, H. Sakurai, K. Konishi, and N. Mio, “Broadband laser-processed terahertz moth-eye antireflection structure with a controlled lattice type,” *Appl. Opt.*, vol. 63, no. 28, p. 7442, Oct. 2024, doi: 10.1364/AO.533467.
- [53] T. W. Ebbesen, H. J. Lezec, H. F. Ghaemi, T. Thio, and P. A. Wolff, “Extraordinary optical transmission through sub-wavelength hole arrays,” *Nature*, vol. 391, no. 6668, pp. 667–669, Feb. 1998, doi: 10.1038/35570.
- [54] T. J. Cui, S. Liu, and L. Zhang, “Information metamaterials and metasurfaces,” *J. Mater. Chem. C*, vol. 5, no. 15, pp. 3644–3668, 2017, doi: 10.1039/C7TC00548B.
- [55] B. Liu, K. Song, and J. Xiao, “Two-Dimensional Optical Metasurfaces: From Plasmons to Dielectrics,” *Adv. Condens. Matter Phys.*, vol. 2019, pp. 1–15, Jan. 2019, doi: 10.1155/2019/2329168.
- [56] A. H. Dorrah and F. Capasso, “Tunable structured light with flat optics,” *Science (80-.)*, vol. 376, no. 6591, Apr. 2022, doi: 10.1126/science.abi6860.
- [57] Z. Li, R. Pestourie, J.-S. Park, Y.-W. Huang, S. G. Johnson, and F. Capasso, “Inverse design enables large-scale high-performance meta-optics reshaping virtual reality,” *Nat. Commun.*, vol. 13, no. 1, p. 2409, May 2022, doi: 10.1038/s41467-022-29973-3.
- [58] Q. Wang *et al.*, “A Broadband Metasurface-Based Terahertz Flat-Lens Array,” *Adv. Opt. Mater.*, vol. 3, no. 6, pp. 779–785, Jun. 2015, doi: 10.1002/adom.201400557.
- [59] J. He *et al.*, “Generation and evolution of the terahertz vortex beam,” *Opt. Express*, vol. 21, no. 17, p. 20230, Aug. 2013, doi: 10.1364/OE.21.020230.
- [60] X.-Y. Jiang *et al.*, “An ultrathin terahertz lens with axial long focal depth based on metasurfaces,” *Opt. Express*, vol. 21, no. 24, p. 30030, Dec. 2013, doi: 10.1364/OE.21.030030.
- [61] S. B. Glybovski, S. A. Tretyakov, P. A. Belov, Y. S. Kivshar, and C. R. Simovski, “Metasurfaces: From microwaves to visible,” *Phys. Rep.*, vol. 634, pp. 1–72, May 2016, doi: 10.1016/j.physrep.2016.04.004.
- [62] A. V. Kuznetsov, A. Canós Valero, M. Tarkhov, V. Bobrovs, D. Redka, and A. S. Shalin, “Transparent hybrid anapole metasurfaces with negligible electromagnetic coupling for phase engineering,” *Nanophotonics*, vol. 10, no. 17, pp. 4385–4398, Nov. 2021, doi: 10.1515/nanoph-2021-0377.
- [63] P. Petrov, A. P. Hibbins, and J. R. Sambles, “Near-field electromagnetic coupling between helices,” *J. Phys. D: Appl. Phys.*,

- vol. 54, no. 44, p. 445108, Nov. 2021, doi: 10.1088/1361-6463/ac1d71.
- [64] F. Hesmer *et al.*, “Coupling mechanisms for split ring resonators: Theory and experiment,” *Phys. status solidi*, vol. 244, no. 4, pp. 1170–1175, Apr. 2007, doi: 10.1002/pssb.200674501.
- [65] P. Gay-Balmaz and O. J. F. Martin, “Electromagnetic resonances in individual and coupled split-ring resonators,” *J. Appl. Phys.*, vol. 92, no. 5, pp. 2929–2936, Sep. 2002, doi: 10.1063/1.1497452.
- [66] E. Tatartschuk, N. Gneiding, F. Hesmer, A. Radkovskaya, and E. Shamonina, “Mapping inter-element coupling in metamaterials: Scaling down to infrared,” *J. Appl. Phys.*, vol. 111, no. 9, May 2012, doi: 10.1063/1.4711092.
- [67] A. A. Basharin, E. Zanganeh, A. K. Ospanova, P. Kapitanova, and A. B. Evlyukhin, “Selective superinvisibility effect via compound anapole,” *Phys. Rev. B*, vol. 107, no. 15, p. 155104, Apr. 2023, doi: 10.1103/PhysRevB.107.155104.
- [68] A. Taflove and M. E. Brodwin, “Numerical Solution of Steady-State Electromagnetic Scattering Problems Using the Time-Dependent Maxwell’s Equations,” *IEEE Trans. Microw. Theory Tech.*, vol. 23, no. 8, pp. 623–630, Aug. 1975, doi: 10.1109/TMTT.1975.1128640.
- [69] Sudarta, “*FDTD Simulation Overview*,” vol. 16, no. 1. Santa Clara, CA, USA: Agilent Technologies, Inc, 2012. [Online]. Available: www.keysight.com
- [70] R. Alaei, C. Rockstuhl, and I. Fernandez-Corbaton, “An electromagnetic multipole expansion beyond the long-wavelength approximation,” *Opt. Commun.*, vol. 407, pp. 17–21, Jan. 2018, doi: 10.1016/j.optcom.2017.08.064.
- [71] T. Liu, R. Xu, P. Yu, Z. Wang, and J. Takahara, “Multipole and multimode engineering in Mie resonance-based metastructures,” *Nanophotonics*, vol. 9, no. 5, pp. 1115–1137, May 2020, doi: 10.1515/nanoph-2019-0505.
- [72] A. E. Miroshnichenko *et al.*, “Nonradiating anapole modes in dielectric nanoparticles,” *Nat. Commun.*, vol. 6, no. 1, p. 8069, Aug. 2015, doi: 10.1038/ncomms9069.
- [73] A. B. Evlyukhin, C. Reinhardt, E. Evlyukhin, and B. N. Chichkov, “Multipole analysis of light scattering by arbitrary-shaped nanoparticles on a plane surface,” *J. Opt. Soc. Am. B*, vol. 30, no. 10, p. 2589, Oct. 2013, doi: 10.1364/JOSAB.30.002589.
- [74] X.-L. Zhang, S. B. Wang, Z. Lin, H.-B. Sun, and C. T. Chan, “Optical force on toroidal nanostructures: Toroidal dipole versus renormalized electric dipole,” *Phys. Rev. A*, vol. 92, no. 4, p. 043804, Oct. 2015, doi: 10.1103/PhysRevA.92.043804.
- [75] K. V. Baryshnikova, D. A. Smirnova, B. S. Luk’yanchuk, and Y. S. Kivshar, “Optical Anapoles: Concepts and Applications,” *Adv. Opt. Mater.*, vol. 7, no. 14, Jul. 2019, doi: 10.1002/adom.201801350.

- [76] V. Savinov, N. Papasimakis, D. P. Tsai, and N. I. Zheludev, “Optical anapoles,” *Commun. Phys.*, vol. 2, no. 1, p. 69, Jun. 2019, doi: 10.1038/s42005-019-0167-z.
- [77] N. Papasimakis, V. A. Fedotov, V. Savinov, T. A. Raybould, and N. I. Zheludev, “Electromagnetic toroidal excitations in matter and free space,” *Nat. Mater.*, vol. 15, no. 3, pp. 263–271, Mar. 2016, doi: 10.1038/nmat4563.
- [78] I. A. Otoo *et al.*, “Broadband transparency in terahertz free-standing anapole metasurface,” *Appl. Phys. Lett.*, vol. 125, no. 26, Dec. 2024, doi: 10.1063/5.0246993.
- [79] V. Stankevič, A. Čermák, S. Mikalauskas, P. Kožmín, S. Indrišiūnas, and G. Račiukaitis, “Processing of ultra-hard materials with picosecond pulses: From research work to industrial applications,” *J. Laser Appl.*, vol. 30, no. 3, Aug. 2018, doi: 10.2351/1.5040633.
- [80] L. Minkevičius *et al.*, “Terahertz zone plates with integrated laser-ablated bandpass filters,” *Electron. Lett.*, vol. 49, no. 1, pp. 49–50, Jan. 2013, doi: 10.1049/el.2012.3509.
- [81] M. E. Shaheen, J. E. Gagnon, and B. J. Fryer, “Femtosecond laser ablation behavior of gold, crystalline silicon, and fused silica: a comparative study,” *Laser Phys.*, vol. 24, no. 10, p. 106102, Oct. 2014, doi: 10.1088/1054-660X/24/10/106102.
- [82] Y.-K. Hsieh *et al.*, “Direct Micromachining of Microfluidic Channels on Biodegradable Materials Using Laser Ablation,” *Polymers (Basel)*, vol. 9, no. 7, p. 242, Jun. 2017, doi: 10.3390/polym9070242.
- [83] R. Ivaškevičiūtė-Povilauskienė, L. Minkevičius, D. Jokubauskis, A. Urbanowicz, S. Indrišiūnas, and G. Valušis, “Flexible materials for terahertz optics: advantages of graphite-based structures,” *Opt. Mater. Express*, vol. 9, no. 11, p. 4438, Nov. 2019, doi: 10.1364/OME.9.004438.
- [84] F. Yu *et al.*, “Laser interference lithography as a new and efficient technique for micropatterning of biopolymer surface,” *Biomaterials*, vol. 26, no. 15, pp. 2307–2312, May 2005, doi: 10.1016/j.biomaterials.2004.07.021.
- [85] B. Voisiat, A. Bičiūnas, I. Kašalynas, and G. Račiukaitis, “Band-pass filters for THz spectral range fabricated by laser ablation,” *Appl. Phys. A*, vol. 104, no. 3, pp. 953–958, Sep. 2011, doi: 10.1007/s00339-011-6456-3.
- [86] I. Kašalynas *et al.*, “Spectroscopic Terahertz Imaging at Room Temperature Employing Microbolometer Terahertz Sensors and Its Application to the Study of Carcinoma Tissues,” *Sensors*, vol. 16, no. 4, p. 432, Mar. 2016, doi: 10.3390/s16040432.
- [87] S. R. Ayyagari, S. Indrišiūnas, and I. Kašalynas, “Hybrid Multiphase Fresnel Lenses on Silicon Wafers for Terahertz Frequencies,” *IEEE Trans. Terahertz Sci. Technol.*, vol. 13, no. 3, pp. 231–236, May 2023, doi: 10.1109/TTHZ.2023.3263638.

- [88] D. W. Prather, D. Pustai, and S. Shi, "Performance of multilevel diffractive lenses as a function of f-number," *Appl. Opt.*, vol. 40, no. 2, p. 207, Jan. 2001, doi: 10.1364/AO.40.000207.
- [89] J. Suszek *et al.*, "Evaluation of the shadow effect in terahertz kinoform gratings," *Opt. Lett.*, vol. 38, no. 9, p. 1464, May 2013, doi: 10.1364/OL.38.001464.
- [90] S. R. Ayyagari *et al.*, "Experimental observation of mutual coupling in resonator array on thin-metal-film," *J. Appl. Phys.*, vol. 137, no. 1, Jan. 2025, doi: 10.1063/5.0245081.
- [91] M. V. Cojocari, A. K. Ospanova, V. I. Chichkov, M. Navarro-Cía, A. Gorodetsky, and A. A. Basharin, "Pseudo-anapole regime in terahertz metasurfaces," *Phys. Rev. B*, vol. 104, no. 7, p. 075408, Aug. 2021, doi: 10.1103/PhysRevB.104.075408.
- [92] V. A. Fedotov, M. Rose, S. L. Prosvirnin, N. Papasimakis, and N. I. Zheludev, "Sharp Trapped-Mode Resonances in Planar Metamaterials with a Broken Structural Symmetry," *Phys. Rev. Lett.*, vol. 99, no. 14, p. 147401, Oct. 2007, doi: 10.1103/PhysRevLett.99.147401.
- [93] K. Koshelev, S. Lepeshov, M. Liu, A. Bogdanov, and Y. Kivshar, "Asymmetric Metasurfaces with High-Q Resonances Governed by Bound States in the Continuum," *Phys. Rev. Lett.*, vol. 121, no. 19, p. 193903, Nov. 2018, doi: 10.1103/PhysRevLett.121.193903.

ANNEX

To initiate the simulations, the CST software was used to, create the model by designing or importing the structure we wished to simulate using the modelling tools available in CST software. Define the appropriate boundary conditions based on simulation requirements by selecting one of perfect electric conductor (PEC) or perfect magnetic conductor (PMC) or open which extends geometry virtually to infinity allowing minimal reflection of waves, or periodic boundary to simulate periodicity in one or more directions, or conducting wall which mimics a lossy metal boundary, or unit cell for structures with two-dimensional periodicity. Then define excitation source types which suites to analysis either by using waveguide ports used for S-parameter calculations in transmission lines or in waveguides, either by using plane wave excitation simulates an incident wave for antenna or for lens, either using discrete ports for lumped element sources. Now, assign materials with proper material properties to the designed model, ensuring proper electromagnetic behavior. Further proper meshing is crucial for simulations as the calculation domain has to be subdivided into small cells, on which Maxwell's Equations are to be solved. However, achieving accurate results while managing computational requirements requires careful selection of spatial and temporal discretization steps. Spatial steps must be smaller than the shortest wavelength of the studied radiation, but excessively small steps increase computational demand without improving accuracy. For this CST has Hexahedral type mesh which is suitable for general purposes, robust even for complex geometries and another Tetrahedral type mesh provides higher conformity to boundaries and is beneficial for adaptive refinement. Now, set up the field monitors to observe specific parameters during or after the simulation like E-/H- field monitors, power flow monitor to Observe energy transmission, far-field/radar cross-section (RCS) monitors for radiation patterns, loss density monitor to analyze power dissipation or specific absorption rate and current density monitor for conductive material losses. Setup the solver depending on the problem type by chosing time domain solver for efficient high-frequency broadband simulations or frequency domain Solver that suited for sub-wavelength or resonant structures and when only a few frequency points are required. Finally use post-processing step to analyze results using CST's visualization tools such as 1D plots for S-parameters, signal responses, 2D/3D field plots for EM field distributions, far-field patterns for radiation characteristics for antennas, loss calculations for total losses and q -factor evaluation...etc. Also another advance feature in CST is that we can perform parametric studies by using parameter sweeps or

optimization technique to analyze the impact of parameter changes on the design performance.

For high-frequency models using the time domain solver, which is efficient for broadband frequency applications. It allows a single calculation run to provide the entire broadband frequency behavior. By selecting boundary conditions with open boundaries for minimal wave reflection, ideal for antenna far-field analysis and antenna arrays, and consider periodic boundaries or unit cell with defined phase shifts to simulate infinite structures. Using hexahedral mesh provides robustness and efficiency for complex high-frequency structures with the use of excitation sources like waveguide ports for transmission lines or discrete ports for lumped elements and Plane Wave Excitation is suitable for far-field or RCS analysis. On the other hand for lower frequencies the frequency domain solver is preferred for low-frequency problems or strongly resonant structures. It minimizes equation setups for limited frequency samples with tetrahedral Mesh, which conforms to material boundaries and is suitable for adaptive refinement. S-parameter calculations using ports are commonly used to assess energy transmission.

CURRICULUM VITAE

Name	Surya Revanth
Surname	Ayyagari
Date of birth	1994-06-04
Place of birth	Nellore, INDIA
Current town	Vilnius, Lithuania
E-mail	surya.revanth@ftmc.lt
ORCID ID:	0000-0002-4129-8232

Education

2021-Present	Center for Physical Sciences and Technology (FTMC) & Vilnius university, Faculty of Physics, <i>joint Ph.D. studies</i>
2017-2019	Karlsruhe Institute of Technology (KIT), Germany, <i>Master's degree in Optic and Photonics</i>

Koneru Lakshmaiah University (KLU), INDIA,
2013-2017 *Bachelor's degree in Mechanical Engineering*

Work experience

2021-now Center for Physical Sciences and Technology
(FTMC)
Junior Research Fellow

2018 May – June Tampere University (TU), Finland
2019 *Research Assistant*

2015-2016 Sri Asha Forgings Pvt.Ltd at Hyderabad, India
Engineer

NOTES

Vilnius University Press
9 Saulėtekio Ave., Building III, LT-10222 Vilnius
Email: info@leidykla.vu.lt, www.leidykla.vu.lt
bookshop.vu.lt, journals.vu.lt
Print run copies 25